Check for updates

ADVANCED FUNCTIONAL MATERIALS
www.afm-journal.de

Copper-based Materials for Photo and Electrocatalytic Process: Advancing Renewable Energy and Environmental Applications

Jéssica C. de Almeida, Yanjie Wang, Thais A. Rodrigues, Paulo H. H. Nunes, Vagner R. de Mendonça, Paulo H. E. Falsetti, Leticia V. Savazi, Tao He, Alexandra V. Bardakova, Aida V. Rudakova, Jie Tian, Alexei V. Emeline, Osmando F. Lopes, Antonio Otavio T. Patrocínio, Jia Hong Pan, Caue Ribeiro,* and Detlef W. Bahnemann**

Cu-based catalysts have emerged as critical components in photo- and electrocatalysis, offering sustainable solutions for renewable energy and environmental applications. The variable oxidation states of Cu enable diverse catalytic pathways, and its abundance, low cost, and tunable properties have positioned them at the forefront of catalytic innovation. This review provides a comprehensive overview of Cu-based catalysts applied for sustainable energy production and environmental remediation. The classification of copper-based catalysts, including metallic copper, copper oxides, copper sulfides, copper halide perovskites, copper-based metal-organic frameworks (MOFs), and covalent organic frameworks (COFs), is discussed, highlighting their structural and functional diversity. Various synthesis methods, such as wet chemical approaches, electrochemical and photochemical routes, sputtering, and thermal decomposition, are presented. The applications of copper-based catalysts in key sustainable energy and environmental remediation processes are explored, focusing on photo- and electrocatalysis. Specifically, CO_2 reduction, water splitting, oxygen reduction, nitrogen fixation, pollutant degradation, and organic synthesis are examined. The mechanisms underlying these processes are analyzed, including the factors influencing their efficiency and selectivity. These applications demonstrate their potential for tackling dual global challenges: diversifying the energy matrix and mitigating environmental issues. By bridging fundamental insights, this review underscores Cu-based catalysts as a cornerstone in advancing sustainable energy technologies.

1. Historical Introduction of Cu-Based Catalysts

The global population is projected to reach 9.8 billion people by 2050, placing increasing pressure on energy resources.[1, 2] Energy plays a critical role in sustaining human life and in developing economies.[3] From an ecological perspective, energy not only maintains the intricacy of individual humans but also supports the integrity and cohesion of social groups, with requirements proportional to their complexity and size.[4,5] According to Our World in Data, the global per capita energy consumption increased by 65% between 1965 and 2023, further emphasizing the need to produce more energy for anthropogenic activities.[6]

1.1. Energy and Environment Crises

Energy sources are primarily classified as fossil fuels, nuclear energy, and renewables.[7] Renewable energy encompasses a variety of sources, including solar, wind, biomass, geothermal, and

J. C. de Almeida, C. Ribeiro
Nanotechnology National Laboratory for Agriculture (LNNA) – Embrapa Instrumentation
São Carlos, SP 13560–970, Brazil
E-mail: caue.ribeiro@embrapa.br

The ORCID identification number(s) for the author(s) of this article can be found under https://doi.org/10.1002/adfm.202502901

© 2025 The Author(s). Advanced Functional Materials published by Wiley-VCH GmbH. This is an open access article under the terms of the Creative Commons Attribution License, which permits use, distribution and reproduction in any medium, provided the original work is properly cited.

DOI: 10.1002/adfm.202502901

Y. Wang, T. He
CAS Key Laboratory of Nanosystem and Hierarchical Fabrication
National Center for Nanoscience and Technology
Beijing 100190, China

T. A. Rodrigues, V. R. de Mendonça, P. H. E. Falsetti, L. V. Savazi
Federal University of São Carlos
Science
and Technology Center for Sustainability – UFSCar
Sorocaba, SP 18052–780, Brazil

P. H. H. Nunes, O. F. Lopes, A. O. T. Patrocínio
Laboratory of Photochemistry and Materials Science
LAFOT-CM
Federal University of Uberlândia
Uberlândia, MG 38400–902, Brazil

hydropower, all of which contribute to environmentally sustainable progress.[8–11] These sources can meet energy demands with minimal or no emissions of pollutants and greenhouse gases (GHGs), offering a cleaner environment, environmental protection, economic benefits, and increased energy security.[8, 9, 12, 13] Moreover, renewable sources are essential for powering remote locations, such as mountainous or desert regions, and contribute significantly to achieving goals outlined in international environmental protection agreements.[14, 15]

The historical trajectory of global energy production has undergone three pivotal transitions: from wood to coal, then to petroleum, and currently towards renewable energy sources. The impetus for renewable energy development intensified following petroleum-related global crises, notably the oil shocks of 1973 and 1979, and the price surge in 1990, underscoring fossil fuel dependence's vulnerabilities.[3] Despite a 126% increase in renewable energy utilization from 1965 to 2023, renewables constituted only 15% of the global energy matrix in 2023. Fossil fuels continue to dominate, accounting for over 81% of global primary energy consumption.[16] This persistent reliance accelerates the depletion of finite resources and exacerbates environmental degradation. The combustion of fossil fuels emits pollutants that are detrimental to human health and contributes substantially to greenhouse gas emissions, thereby intensifying climate change.[3, 17–20]

Currently, anthropogenic activities are responsible for climate change through the emission and accumulation GHGs in the atmosphere, such as carbon dioxide (CO_2), methane (CH_4), nitrous oxide (N_2O), hydrofluorocarbons, perfluorocarbons – fully fluorinated compounds, especially perfluoromethane (CF_4) and perfluoroethane (C_2F_6), and sulfur hexafluoride (SF_6).[21–24] These gases trap infrared radiation, disrupting Earth's radiative balance and raising global temperatures.[24] While the greenhouse effect is a natural process essential for maintaining Earth's temperature—driven by water vapor (30–70%), CO_2 (9–26%), CH_4 (4–9%), and O_3 (3–7%)—its intensification due to human activity has raised concerns since the 1960s, potentially triggering events like disruptions to the hydrological cycle.[24, 25]

CO_2, one of the primary compounds of Earth's core, crust, and atmosphere, plays a vital role in biochemical processes such as respiration and photosynthesis.[23, 26, 27] However, since the Industrial Revolution, exponential population growth and reliance on fossil fuels have disrupted the carbon cycle, leading to a significant rise in atmospheric CO_2 levels.[23, 28, 29] In 2023, CO_2 accounted for 74.9% of global GHG emissions, with per capita CO_2 emissions increasing by 298% from 1900 to 2023, outpacing population growth.[30–32] This has prompted transnational governance to mitigate emissions, starting with the 1979 Geneva climate conference, followed by protocols like the Kyoto Protocol (1997), the Doha Amendment (2012), and the Paris Agreement (2016), which aim to limit global temperature increases to 1.5–2 °C by 2100.[33–36] The Intergovernmental Panel on Climate Change estimates that achieving the 1.5 °C target requires a 45% reduction in GHG emissions by 2030 (from 2010 levels) and net-zero emissions by 2050.[37] However, current strategies fall short, and global temperatures have already exceeded the 1.5 °C threshold in 2024, highlighting the urgency for innovative solutions.[38]

Anthropogenic activities have also significantly affected global water resources, a critical component for sustaining life.[39] Emerging contaminants, a concept formally introduced by Petrović et al. in 2003, pose significant risks to aquatic environments and human health due to their unregulated presence.[40, 41] Dyes, stand out as a significant issue due to their high stability and difficulty removing them from aqueous environments. These substances contain chromophores responsible for their characteristic coloration, which gives them dyeing capabilities. For this reason, they are widely used in textiles, cosmetics, plastic, and various other industries.[42] It is estimated that more than 700 000 tons of dyes are consumed annually across multiple industries worldwide, with ≈10–15% of these dyes being lost during processing and ultimately discharged into wastewater streams.[43] These compounds reduce sunlight penetration, disrupt photosynthesis, and exhibit mutagenic and carcinogenic effects, threatening aquatic ecosystems and human health.[44, 45] Pharmaceuticals, classified as micropollutants, further exacerbate water contamination, with long-term exposure posing risks to aquatic life and humans.[46] With water demand projected to rise significantly by 2050, effective treatment solutions are urgently needed, particularly as emerging pollutants threaten irrigation water quality and monitoring remains inadequate.[47, 48]

1.2. Advances in Cu-Based Catalysts

Cu-based catalysts have emerged as versatile materials in photo- and electrocatalysis, offering sustainable solutions for renewable energy production and environmental remediation. The variable oxidation states of transition metal Cu (e.g., Cu^0, Cu^+, Cu^{2+}) enable diverse catalytic pathways, while its abundance, low cost, and tunable properties position Cu-based catalysts as key players in catalytic innovation.[49, 50]

V. R. de Mendonça
Federal Institute of Education
Science
and Technology of São Paulo – IFSP Campus Itapetininga
Itapetininga, SP 18202-000, Brazil

T. He
University of Chinese Academy of Sciences
Beijing 100049, China

A. V. Bardakova, A. V. Rudakova, A. V. Emeline, D. W. Bahnemann
Laboratory of Photoactive nanocomposite materials
Saint-Petersburg University
Saint Petersburg 199034, Russia
E-mail: bahnemann@iftc.uni-hannover.de

J. Tian, J. H. Pan
International Joint Center of Nature-Inspired Carbon Neutrality Solutions
School of Resources, Environment and Materials
Guangxi University
Nanning, Guangxi 530004, China
E-mail: jhpan@gxu.edu.cn

A. O. T. Patrocínio
Centro de Excelência em Hidrogênio e Tecnologias Energéticas Sustentáveis (CEHTES)
Federal University of Goias
Goiânia, GO, Brazil

D. W. Bahnemann
Institut Fuer Technische Chemie
Gottfried Wilhelm Leibniz Universität Hannover
Callinstrasse 3, 30167 Hannover, Germany

© 2025 The Author(s). Advanced Functional Materials published by Wiley-VCH GmbH

16163028, 0, Downloaded from https://advanced.onlinelibrary.wiley.com/doi/10.1002/adfm.202502901 by EMBRAPA - Empresa Brasileira de Pesquisa Agropecuaria, Wiley Online Library on [06/06/2025]. See the Terms and Conditions (https://onlinelibrary.wiley.com/terms-and-conditions) on Wiley Online Library for rules of use; OA articles are governed by the applicable Creative Commons License

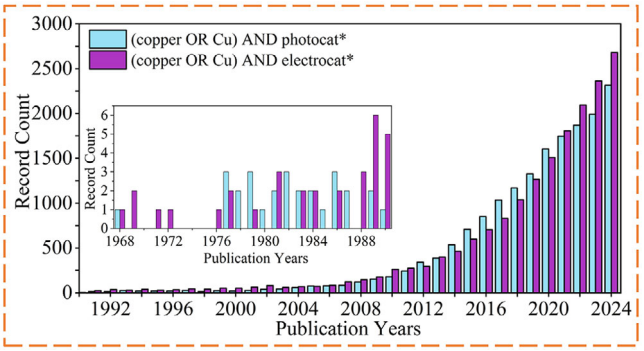

Figure 1. Trends in publications on photo- and electrocatalysis involving Cu-based catalysts, based on Web of Science data using specified keywords.

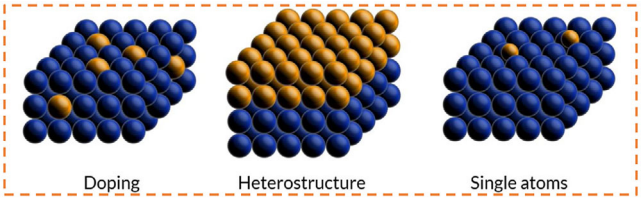

Figure 2. Schematic representation of examples of structural modifications employed in the literature to address the limitations of pristine materials.

The significance of copper in the realm of catalysis has been acknowledged for several decades. This recognition dates back to the 1960s, with the development of a Cu-based catalyst capable of producing methanol by thermal catalysis with CO_2 as the primary reactant. The process was patented by Imperial Chemical Industries, and this period marked a turning point in the industrial production of methanol, as the new catalyst demonstrated superior efficiency compared with previously employed materials composed of Cr and ZnO. This catalyst enabled methanol synthesis under milder conditions, significantly advancing industrial catalysis.[51–53]

The application of Cu-based catalysts in photo- and electrocatalysis also began in the 1960s. Specifically, in 1968, the initial studies on photo- and electrocatalysis properties were published.[54, 55] Early research demonstrated Cu's potential in photocatalysis, such as its use in combination with TiO_2 for various reactions, highlighting its role as a catalyst and co-reactant.[56] Cu was also chosen considering its previously recognized efficacy as an electrocatalytic metal in the electrochemical reduction of CO_2 to methane by Hori et al.[57–59] Subsequent studies explored Cu-loaded TiO_2 for photocatalytic applications, though challenges like low efficiency persisted and the need for further separation of gas products.[60] The field gained significant momentum in the 2010s, driven by works like Yang et al.'s 2010 study on Cu(I)/TiO_2, which investigated the photocatalytic mechanisms.[61] In this work, the pathway of photocatalytic transformation involving CO_2 and water over Cu(I)/TiO_2 was explored utilizing in situ diffuse reflectance infrared Fourier transform spectroscopy (DRIFTS) combined with isotopically labeled $^{13}CO_2$. Their observation suggested that carbonaceous species residing on the catalyst surface participated in reactions. This research has provided a reliable basis for future studies and has opened avenues for numerous additional inquiries. **Figure 1** illustrates the growing trend in publications on Cu-based photo- and electrocatalysis, reflecting their expanding role in sustainable technologies.

Cu-based catalysts are highly versatile, with applications spanning renewable energy production and environmental remediation. They are employed in processes such as water splitting for hydrogen production, nitrogen fixation for ammonia synthesis, pollutant degradation for water purification, organic synthesis for value-added chemicals, and CO_2 reduction for fuel generation. In this context, recent research has shown a trend to explore combinations of Cu and other materials to improve the selectivity of reaction products. This is partly due to the results of several studies highlighting the ability of Cu-based catalysts to produce valuable hydrocarbons and alcohols through CO_2 reduction.[62–64] However, there is a need to improve the surface structure, morphology, and composition of the catalysts to achieve optimal performance. Additionally, challenges such as stability under reaction conditions remain, particularly for copper oxides like Cu_2O, which can undergo irreversible redox disproportionation ($Cu_2O \rightarrow Cu + CuO$) under light irradiation, reducing their stability.[65, 66]

To address these limitations, strategies such as doping, constructing heterostructures, and creating single atoms have been developed.[67–71] For instance, Cu-based heterostructures with other metals or oxides enhance charge separation and stability, improving overall catalytic efficiency.[72–75] **Figure 2** illustrates examples of structural modifications that can be applied to copper-based catalysts to enhance their performance in electrochemical or photocatalytic applications.

While prior reviews have provided valuable, albeit often specialized, insights into Cu-based catalysis, focusing distinctly on areas such as plasmon-enhanced photocatalysis,[76] the application of specific nanostructures for pollutant degradation,[77, 78] the development of earth-abundant oxide photocathodes solely for photoelectrochemical water splitting,[79] electrocatalytic CO_2 conversion pathways,[80] photoinduced deracemization,[81] advancements in copper sulfide materials,[82] or sustainable synthesis strategies for nanomaterials,[83] the present work comprehensively summarizes recent advancements in Cu-based catalysts for sustainable energy production and environmental remediation, focusing on their classification, synthesis, and applications in photo- and electrocatalysis. This review offers a discussion of the diverse types of Cu-based catalysts, including not only well-established materials like copper oxides and sulfides but also emerging classes such as halide perovskites, metal–organic frameworks (MOFs), and covalent organic frameworks (COFs). Furthermore, the review provides a detailed overview of various synthesis methods, emphasizing how these methods influence the structural and functional properties of Cu-based catalysts. By linking fundamental catalyst properties with their performance in key applications like CO_2 reduction, water splitting, nitrogen fixation, pollutant degradation, and organic synthesis, this review highlights the potential of Cu-based catalysts to address energy and environmental challenges.

© 2025 The Author(s). Advanced Functional Materials published by Wiley-VCH GmbH

16163028, 0, Downloaded from https://advanced.onlinelibrary.wiley.com/doi/10.1002/adfm.202502901 by EMBRAPA - Empresa Brasileira de Pesquisa Agropecuaria, Wiley Online Library on [06/06/2025]. See the Terms and Conditions (https://onlinelibrary.wiley.com/terms-and-conditions) on Wiley Online Library for rules of use; OA articles are governed by the applicable Creative Commons License

2. Classification of Cu-Based Catalysts

Cu, a 3d transition metal, exhibits diverse oxidation states (Cu^0, Cu^{1+}, Cu^{2+}, and Cu^{3+}) and unique chemical and physical properties. This versatility enables Cu-based materials to participate in various catalytic reactions through one-electron ($1e^-$) and two-electron ($2e^-$) transfer pathways, depending on their oxidation states. Their structural and functional diversity makes Cu-based catalysts suitable for various applications in photo and electrocatalysis. Cu-based catalysts are typically classified based on their composition and properties.

2.1. Metallic Cu

Coupling metals with semiconductors is an effective strategy to achieve high performance. Precious metals such as Au, Ag, Pt, and Pd are commonly used as cocatalysts but are limited by high costs. As a cost-effective alternative, Cu^0 facilitates charge separation and transfer and is a catalytic active center.

Although free-standing Cu^0 nanomaterials can function as catalysts, they often face stability challenges. Cu^0 is more commonly used as a cocatalyst due to its excellent electronic conductivity, enabling it to act as a reactive center by enriching electrons and facilitating reactions. Cu^0 also serves as a bridge between materials, often deposited on a substrate to form a composite system where the support stabilizes Cu^0 and promotes charge dispersion. Typical substrates include metal oxides (e.g., TiO_2, ZnO, NiO), metal sulfides (e.g., MoS_2), carbon-based materials (e.g., graphene, and carbon nanotubes), carbon nitrides, zeolites, and metal-organic frameworks. The synthesis of Cu^0-based materials relies on various methods, including wet chemical approaches, electrochemical techniques, photochemical routes, and sputtering deposition. These methods allow precise control over key parameters such as particle size, morphology, and catalytic activity.

One of the most widely used methods for preparing Cu^0 nanomaterials is wet chemical synthesis, wherein Cu^{2+} is reduced to Cu^0 by using suitable reducing agents. Common Cu precursors include $CuCl_2$, $Cu(SO_4)_2$, $Cu(NO_3)_2$, $Cu(OAc)_2$ and $CuCl(PPh_3)_3$, which are reduced by agents such as $NaBH_4$, glucose, ascorbic acid and hydrazine hydrate ($N_2H_4{\cdot}H_2O$).[84–89] The size and morphology of Cu nanomaterials play a crucial role in determining their optical properties and catalytic activities. Various morphologies have been developed, such as nanotubes, nanowires, nanosheets, and porous structures. Capping agents like polyvinylpyrrolidone (PVP), poly(acrylic acid) (PAA), and octadecylamine are frequently employed to achieve precise control over size and shape. For example, Wang et al.[89] prepared Cu nanoparticles with controlled size and shape by reducing Cu^{2+} in an aqueous solution using hydrazine as the reduction agent and PAA as the capping agent. They identified an optimal pH range (9.2–10.5) for producing pure Cu nanoparticles with PAA.

Furthermore, the pH range for generating metallic Cu or copper oxide varies across systems with different capping agents, such as alkanethiols, PVP, and PAA. Their study also demonstrated that the shape and diameter of Cu nanoparticles could be enhanced by adjusting the concentration of PAA, with cuboctahedral-shaped particles obtained at moderate PAA concentrations. Additionally, using sodium citrate and citric acid as complexing agents further enables control over the morphology of Cu nanocrystals.[90, 91] For instance, Yokoyama et al.[91] reported that the size of Cu nanoparticles synthesized at pH 13 was smaller than those produced at pH 11 and 12, using citric acid as both a complexing and capping agent in an aqueous solution. Additionally, hydrophilic ionic liquids, such as 3-methyl-n-butylimidazolium tetrafluoroborate ($BMIm.BF_4$), have been employed as templates to control nanoparticle size and as stabilizing agents during Cu nanoparticle synthesis.[92]

Beyond the standalone Cu nanoparticles, most Cu is deposited and dispersed on substrates to achieve synergistically enhanced photocatalytic properties. Semiconductor-like MOFs and COFs are ideal supports due to their high porosity and extensive surface areas. For example, Xiao et al.[93] deposited Cu nanoparticles on the surface and encapsulated them within UiO-66 using an advanced double-solvent approach followed by a one-step reduction. They attributed the superior photocatalytic performance to a combination of factors, including the plasmonic effects of the Cu nanoparticles on UiO-66 and the formation of Schottky junctions facilitated by Cu quantum dots encapsulated within the UiO-66 framework.

Electrochemical synthesis is a widely used method for producing metal nanostructures, valued for its low cost, low-temperature requirements, and simplicity of operation. In this method, Cu^{2+} ions are reduced to Cu^0 by applying a negative bias. The morphology of the resulting Cu clusters and particles can be controlled by adjusting parameters such as deposition time, electrolyte concentration, and the use of capping agents. Additionally, utilizing templates in the electrochemical process provides a more precise means to control particle morphology. For instance, Cu nanoparticles have been deposited onto TiO_2 nanotube arrays using a pulsed electrochemical deposition technique, resulting in significantly enhanced hydrogen (H_2) evolution performance across all Cu/TiO_2 nanotube arrays.[94] Similarly, $Cu{-}Cu_2O$ structures were electrodeposited onto the surface of TiO_2 nanotube arrays at deposition potentials ranging from −1.0 to −1.6 V, with Cu^{2+} ions being reduced electrochemically to Cu_2O, accompanied by the simultaneous formation of Cu^0 on the top surface of the TiO_2 nanotubes.[95] A comparable configuration has also been employed in Cu/Co_3O_4 systems. Co_3O_4 nanotubes were initially synthesized on a Co foil substrate, providing a high specific surface area and an ideal platform for Cu nanoparticle loading via a pulsed galvanostatic method.[96]

Photochemical synthesis is another effective method for depositing Cu onto supports, assisted by light irradiation. In this approach, a Cu precursor is dissolved in a solvent containing dispersed semiconductor particles, allowing Cu cations to adsorb onto the surface of the semiconductor. Under illumination, photogenerated electrons generated by the semiconductor reduce Cu cations to Cu^0, which is uniformly dispersed onto the semiconductor surface. To prevent oxidation of the Cu^0, the reaction is typically carried out in an inert gas atmosphere with oxidative sacrificial agents such as methanol, ethanol, triethanolamine (TEOA), or trimethylamine (TEA). For example, Kazuma et al.[97] deposited Cu nanoparticles onto UV-irradiated TiO_2 in an aqueous solution containing ethanol and $Cu(CH_2COO)_2$, with the system deaerated by N_2 gas flow. Their synthesized ultrafine Cu nanoparticles exhibited optical properties characteristic of localized surface plasmon resonance (LSPR). Similarly, photochemical deposition was utilized to prepare Cu nanodots in

© 2025 The Author(s). Advanced Functional Materials published by Wiley-VCH GmbH

16163028, 0, Downloaded from https://advanced.onlinelibrary.wiley.com/doi/10.1002/adfm.202502901 by EMBRAPA - Empresa Brasileira de Pesquisa Agropecuaria, Wiley Online Library on [06/06/2025]. See the Terms and Conditions (https://onlinelibrary.wiley.com/terms-and-conditions) on Wiley Online Library for rules of use; OA articles are governed by the applicable Creative Commons License

the Cu/TiO_2@$Ti_3C_2T_x$ ternary photocatalytic system for efficient H_2 evolution, where ethanol served as a sacrificial agent.[98] Methanol has also been employed as a sacrificial agent in the preparation of Cu-loaded TiO_2 systems.[99]

In some cases, Cu nanoparticles are synthesized in situ during the photocatalytic reaction. For example, a Cu/carbon quantum dots (CQDs) system was prepared via in-situ photoreduction during an H_2 evolution reaction, where copper acetate was added as the precursor for Cu deposition.[100] Under light irradiation, Cu nanoparticles were generated and anchored on CQDs while the H_2 evolution reaction proceeded. Photochemical synthesis and photocatalytic activity have also been integrated into other systems. Zhang et al. developed a Cu/reduced graphene oxide (rGO) nanosheet system via a similar photochemical approach.[101] Cao et al. demonstrated a stepwise reduction process, converting Cu^{2+} to Cu_2O and eventually to Cu nanoparticles in water with TEOA or TEA as sacrificial agents. This achieved efficient H_2 evolution with the in-situ generated Cu nanoparticles.[102]

Physical preparation methods, such as sputtering deposition and molecular beam epitaxy, are direct and practical techniques for synthesizing Cu nanoparticles, utilizing high-purity Cu as the target material. The substrate and preparation conditions significantly influence the morphology and orientation of the Cu nanoparticles. Gleißner et al.[103] investigated the epitaxial growth of Cu nanoparticles on ZnO single-crystal surfaces with various orientations. Their study demonstrated that the morphology and surface facets of the Cu nanoparticles could be precisely tailored through epitaxial growth on ZnO substrates with specific crystallographic orientations, such as ZnO(0001), ZnO(000$\bar{1}$), and ZnO(10$\bar{1}$4).

Cu nanoparticles can be synthesized by calcinating Cu precursors in a reducing atmosphere, such as H_2 gas.[104] By carefully adjusting the calcination conditions, it is possible to control the oxidation states of Cu and regulate the proportion of Cu^0 within the system.[105] During calcination, Cu nanoparticles can be formed and anchored onto bulk materials using a sequential in situ exsolution (in H_2) and redispersion (in N_2) strategy, which was applied to fabricate Cu-decorated $LaFeO_3$ photocatalysts.[106]

Besides calcination, other methods such as thermal decomposition of Cu precursors,[107] pyrolysis,[108] microwave-assisted method,[109] and sonochemical techniques are also effective for preparing Cu nanomaterials. Each method offers unique advantages in controlling particle size, morphology, and catalytic properties.

In addition to standalone Cu nanoparticles and Cu deposited on substrates, Cu nanoparticles have also been utilized as interfacial bridges to facilitate charge transfer. These systems are typically prepared through multistep processes. For example, Cu_2O/Cu/AgBr/Ag photocatalyst was successfully prepared through a two-step method involving a cation adsorption-reduction mechanism to produce Cu_2O/Cu, followed by photo-assisted deposition.[110] The Cu nanoparticles, positioned between Cu_2O and AgBr, significantly enhanced charge transfer across the interface, thereby improving photocatalytic pollutant degradation performance. Similarly, Cu_2O/Cu/TiO_2 was fabricated by an impregnation-reduction method.[111] In this system, the Ohmic heterojunction formed by the Cu^0 at the interface between Cu_2O and TiO_2 nanotubes facilitated efficient charge transfer, enhancing H_2 evolution activity.

2.2. Cu-Based Oxides

Cu-based oxides, particularly Cu_2O and CuO, are among the most extensively studied catalysts. These p-type semiconductors possess direct narrow bandgaps (CuO: 1.3–1.7 eV; Cu_2O: 1.9–2.2 eV)[112, 113] that vary depending on the preparation methods and conditions. They stand out for their low cost, low toxicity, and facile synthesis, making them attractive materials for photocatalytic applications.

2.2.1. CuO

CuO adopts a monoclinic lattice structure, with its phase and morphology highly tunable through various factors such as shape-control agents, the type of Cu precursor, solvent, reaction temperature, and reaction time.[114, 115] CuO has been synthesized in multiple morphologies, including nanowires, cubes, nanosheets, and flower-like structures.[116–119]

Co-precipitation is an effective method for CuO preparation, though it typically results in large particle sizes. For example, Said et al.[120] used co-precipitation to produce CuO with tunable particle sizes and morphologies by adjusting the water-to-ethanol ratio in the reaction medium. Rod-like CuO particles with an average size of 13 nm were synthesized in pure water, while spherical particles around 7 nm were obtained in pure ethanol. Interestingly, CuO nanoparticles exhibited morphology-dependent photocatalytic performance, with those synthesized in pure water showing superior Congo red dye removal compared to those prepared in ethanol.[121] Hydrothermal and solvothermal methods are the most commonly employed approaches for CuO crystallization, offering significant advantages in controlling particle size (achieving a smaller sizer) and optimizing textural properties. For instance, 3D hierarchical cotton-candy-like CuO microspheres, ≈1–3 µm in diameter, were synthesized via a solvothermal method using ethylene glycol, followed by calcination.[122] The authors identified that a Cu^{2+}/urea ratio of 1:3, a reaction temperature of 140 °C, and ethylene glycol were critical for forming these microspheres. Aslani[123] prepared CuO nanostructures with diverse morphologies, including nanoparticles, nanorods, and nanoclusters, with sizes ranging from 40 to 100 nm, by controlling pH, temperature, and reaction time during the solvothermal process. Hong et al.[124] employed an alcohothermal route to prepare CuO nanoparticles from copper acetate precursor. The particle size was controlled to be between ≈3 and 9 nm by controlling the reaction temperature. In recent years, coupling these techniques with sonoelectrochemical methods has been proposed to increase yields in rapid approaches for CuO synthesis, further expanding the toolkit for producing these versatile oxides.[121]

Pure CuO generally exhibits poor photocatalytic efficiency due to rapid charge recombination. Various strategies have been developed to enhance its catalytic performance and address this limitation, including metal doping, heterostructure construction, and cocatalyst decoration. For instance, size-tunable CuO nanodots were successfully decorated on the surface of TiO_2 nanoparticles functionalized with PAA. This functionalization facilitated the selective precipitation of $Cu(OH)_2$ onto the TiO_2 surface.[125] Subsequently, $Cu(OH)_2$ was dehydrated and transformed into

© 2025 The Author(s). Advanced Functional Materials published by Wiley-VCH GmbH

16163028, 0, Downloaded from https://advanced.onlinelibrary.wiley.com/doi/10.1002/adfm.202502901 by EMBRAPA - Empresa Brasileira de Pesquisa Agropecuaria, Wiley Online Library on [06/06/2025]. See the Terms and Conditions (https://onlinelibrary.wiley.com/terms-and-conditions) on Wiley Online Library for rules of use; OA articles are governed by the applicable Creative Commons License

CuO nanodots. Interestingly, during photocatalytic reactions under UV irradiation with methanol as a hole scavenger, Cu^{2+} was reduced to Cu^0, which acted as an efficient cocatalyst for water splitting. Brito et al. employed a different approach to anchor CuO onto TiO_2 nanotubes via dip coating, forming a p–n junction for photocatalytic water splitting applications.[126] Similarly, a one-step hydrothermal method under pH 12 was used to disperse CuO nanoparticles on ZnO nanorods uniformly.[127] The resultant ZnO/CuO heterojunction facilitated the separation of photogenerated electron-hole pairs, significantly enhancing photocatalytic activity for methylene blue degradation.

2.2.2. Cu_2O

Cu_2O is one of the most promising candidates for photocatalytic reactions under visible light, owing to its narrow bandgap and unique properties. Its cubic lattice structure naturally facilitates the formation of nanocube morphologies. Notably, the size and exposed crystal planes of Cu_2O significantly influence its photocatalytic performance due to variations in band positions. Consequently, extensive research has been devoted to controlling the exposure of specific Cu_2O facets to optimize its catalytic activity.

Wet chemical synthesis is the most commonly employed method for producing Cu_2O. Surfactants, such as PVP, cetyltrimethylammonium bromide, and sodium dodecyl sulfate, are crucial for controlling morphology. The Huang group has conducted extensive research on Cu_2O synthesis.[128–130] Submicrometer-sized Cu_2O crystals with various morphologies, like cubic, truncated cubic, cuboctahedral, truncated octahedral, octahedral, and short hexapod structures, have been prepared (**Figure 3**a-h).[128] In this study, Cu_2O was synthesized using an aqueous solution containing $CuCl_2$, NaOH, sodium dodecyl sulfate (SDS) as a surfactant, and $NH_2OH{\cdot}HCl$ as a reductant. The morphology was primarily tuned by adjusting the volume of $NH_2OH{\cdot}HCl$ and the order of reagent addition. With slightly different amounts of $NH_2OH{\cdot}HCl$, NaOH, and H_2O, the pH of the solution became basic at 10.6, forming extended hexapods. Photocatalytic tests revealed significant activity differences between the morphologies, with octahedra and extended hexapods demonstrating excellent photocatalytic performance.

Using electrodeposition, Cu-Cu_2O core-shell structures with cubic, cuboctahedral, and octahedral morphologies were also successfully fabricated by controlling the $CuSO_4{\cdot}5H_2O$ electrolyte concentration.[131] Additionally, solvent selection played a pivotal role in shaping Cu_2O. For example, Cu_2O nanosheets were synthesized via a wet chemical approach. Initially, Cu nanocolloids were formed through the disproportionation of Cu^+, followed by the formation of Cu_2O nanosheets in ethanol, which served as both the oxidant and solvent.[132] It was demonstrated that the solvent helped limit the oxidized processes. Cu nanospheres and nanocubes were obtained with water and acetone as solvents, respectively.

Tunable Cu_2O nanoparticles were achieved using mesoporous silica supports.[133] In this study, silica-supported CuO nanoparticles were prepared using an impregnation-drying-heating process. By varying the Cu precursor concentration or the pore diameter of silica supports, Cu_2O nanoparticles with sizes ranging from 2 to 15 nm were produced through the reduction of CuO in

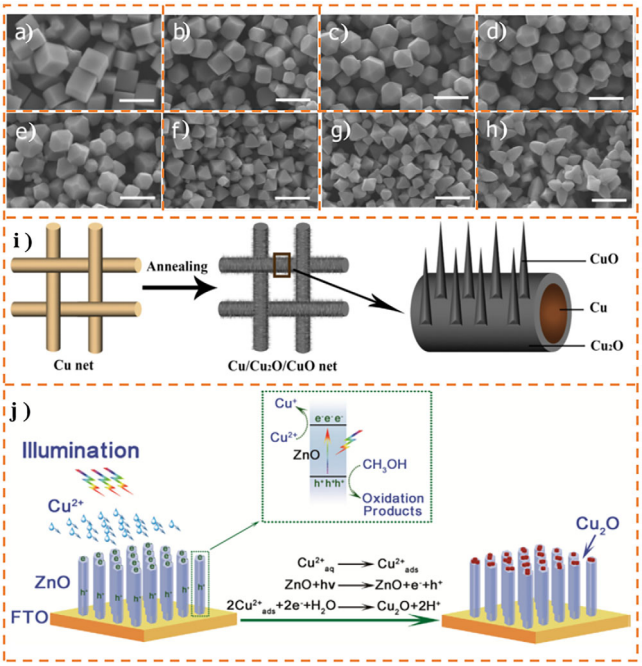

Figure 3. SEM images for Cu_2O nanocrystals with various morphologies: a) cubes, b) truncated cubes, c) cuboctahedra, d) type I truncated octahedra, e) type II truncated octahedra, f) octahedra, g) short hexapods, h) extended hexapods. Scale bar: 1 µm. i) Diagram for fabricating Cu/Cu_2O/CuO heterojunction. j) Schematic illustration of photochemical deposition of Cu_2O on ZnO nanorods. a-h) Reproduced with permission.[128] Copyright 2009, American Chemical Society. i) Reproduced with permission.[136] Copyright 2017, Elsevier. j) Reproduced with permission.[138] Copyright 2018, Elsevier.

CO. These nanoparticles exhibited high activity and stability for photocatalytic H_2 evolution in a mixture of the same proportion of water and methanol.

Uniform, high-quality Cu_2O nanoparticles were synthesized using a seed layer-assisted chemical bath deposition method.[134] This involved first depositing an ITO seed layer on glass slides via RF magnetron sputtering, followed by the growth of Cu_2O nanoparticles on the seeded ITO layer using copper chloride as the precursor.

Additionally, photodeposition is a widely used method for synthesizing Cu_2O. For instance, Zhai et al.[135] employed this technique to load Cu_2O onto TiO_2, using $CuSO_4$ as the precursor. By varying the irradiation time, they could tune the Cu_2O content. The Cu_2O and Pt co-modified TiO_2 demonstrated significantly enhanced photocatalytic activity for CO_2 reduction, yielding CH_4 and CO.

Cu-based systems with mixed oxidation states are widely utilized to establish heterojunctions that exhibit mixed narrow band gaps for broad light absorption and efficient charge separation. For example, a Cu^0/Cu_2O/CuO heterojunction was prepared by calcining a Cu net in the air (Figure 3i).[136] Additionally, CuO/Cu_2O/Cu nanoparticles were prepared using a sonochemical and thermal synthesis approach, with copper acetate as the precursor.[137] The Cu_2O/CuO heterojunction, coupled with Cu^0 cocatalysts, generates synergistic effects that enhance photogenerated charge separation and transfer, significantly

© 2025 The Author(s). Advanced Functional Materials published by Wiley-VCH GmbH

16163028, 0, Downloaded from https://advanced.onlinelibrary.wiley.com/doi/10.1002/adfm.202502901 by EMBRAPA - Empresa Brasileira de Pesquisa Agropecuaria, Wiley Online Library on [06/06/2025]. See the Terms and Conditions (https://onlinelibrary.wiley.com/terms-and-conditions) on Wiley Online Library for rules of use; OA articles are governed by the applicable Creative Commons License

improving the photocatalytic activity measured through dye degradation.

Standalone Cu_xO typically exhibits limited photocatalytic performance. However, its narrow bandgap makes it highly effective for light absorption. Consequently, Cu_xO is frequently utilized as an efficient light-absorbing component in heterojunction systems with other semiconductors. For instance, Cu_2O nanoparticles have been anchored onto g-C_3N_4 through a one-pot in situ reduction method involving the calcination of melamine and Cu precursor mixture at high temperatures.[139] In this configuration, Cu_2O serves as a sensitizer for light absorption and forms a Type II heterojunction with g-C_3N_4, significantly enhancing H_2 evolution. Similarly, tunable Cu_xO compositions have been loaded onto carbon nitride nanotubes (CNNTs) via a one-pot synthesis method, with the composition adjusted by annealing under different atmospheric conditions.[140] A Z-scheme heterojunction (Cu_2O@CuO/CNNTs) was achieved through calcination in an H_2/Ar atmosphere, whereas a Type II heterojunction (CuO/CNNTs) was formed in air.

Wide-bandgap ZnO has also been integrated with Cu_2O to create heterojunctions that improve light absorption and charge separation capabilities. For example, Cu_2O nanoparticles were photodeposited selectively at the tips of ZnO nanorods (Figure 3j).[138] During this photochemical deposition, $CuSO_4$ was employed as the Cu precursor, with water as the solvent, 5% methanol as the sacrificial agent, and lactic acid as the stabilizer to prevent precipitation. This process resulted in constructing a ZnO/Cu_2O p-n heterostructure, which demonstrated enhanced CO_2 photoreduction. In another study, Cu_2O nanoparticles were decorated onto vertically aligned ZnO nanorod arrays via electrodeposition, leading to improved photocatalytic degradation of methyl orange compared to pure ZnO or Cu_2O.[141] Wang et al.[142] synthesized a hybrid photocatalyst, CuO_x@p-ZnO, using Cu-doped zeolitic imidazolate framework-8 (ZIF-8) as the precursor. This material showed the ability to photoreduce CO_2 to CH_4 and C_2H_4. Notably, during the initial reaction stage, a self-preactivation process reduced surface Cu^{2+} to Cu^+, crucial for CO trapping and C–C coupling to generate C_2H_4.

To further enhance the performance of Cu_2O, Ag@Cu_2O core-shell nanoparticles were synthesized, where Cu_2O shells were grown on Ag nanoparticle cores via a wet chemical reduction method. By controlling the thickness of the Cu_2O shell, light absorption in the visible region was effectively tuned. It was observed that under illumination, plasmonic energy transfer from Ag to Cu_2O facilitated charge separation, resulting in improved photocatalytic performance for the degradation of methyl orange.

A significant challenge in applying Cu_2O is its susceptibility to photocorrosion, which leads to rapid deactivation. To address this issue, Cu_2O is often combined with other materials to facilitate electron extraction from Cu_2O. One practical approach involves coupling Cu_2O with rGO to improve its photocatalytic performance and photostability.[143, 144] Tran et al.[144] utilized an in situ growth method to anchor Cu_2O nanoparticles onto rGO, forming a p-n junction that exhibited enhanced photocatalytic H_2 production and improved stability. In a separate study, Mateo et al. supported Cu_2O nanoparticles on few-layer graphene through the chemical reduction of $Cu(NO_3)_2$.[145] This system achieved remarkable CO_2 methanation at 250 °C, with a CH_4 production rate of 14.93 mmol $g^{-1}(Cu_2O)$ h^{-1}. However, the Cu_2O nanoparticles were reduced to metallic Cu during the catalytic reaction. It was suggested in this work that the stability of it could be enhanced by reoxidizing it or coating the Cu_2O with a thin Au overlayer.

Additionally, noble metals such as Ag and Au deposited on the surface of Cu_2O can act as electron sinks, enabling photogenerated holes to participate in surface reactions. This promotes efficient electron-hole separation and enhances photocatalytic efficiency.[146] Coupling CuO with rGO has also been explored to improve photocatalytic activity. For instance, Gusain et al.[147] prepared rGO-CuO and rGO-Cu_2O systems using individual steps. CuO was synthesized first via a wet chemical reaction and then covalently grafted onto rGO nanosheets. rGO/Cu_2O was prepared for comparison by hydrothermal reduction of rGO/CuO. Under identical conditions, rGO-CuO exhibited superior photocatalytic activity compared to rGO-Cu_2O, attributed to the slower charge carrier recombination and efficient transfer of photogenerated electrons through the rGO framework in rGO-CuO.

2.2.3. Cu-Based Mixed-Metal Oxides

While Cu_2O and CuO show promise for catalytic applications, their band gaps restrict them to absorbing only a fraction of the solar spectrum. To overcome this limitation, Cu-based mixed-metal oxides, including ternary and quaternary oxides, have been explored as alternative Cu-based photocatalysts. These compounds consist of Cu in +1 or +2 oxidation states and other metal elements, offering enhanced flexibility for tuning optical and electronic properties.

Cu(I)-based oxides include a variety of compounds such as copper vanadates (e.g., Cu_3VO_4, $CuVO_3$), copper niobates (e.g., $CuNbO_3$, $CuNb_3O_8$, $Cu_2Nb_8O_{21}$, $CuNb_{13}O_{33}$), and copper tantalate (e.g., $Cu_2Ta_4O_{11}$, $Cu_3Ta_7O_{19}$, $Cu_5Ta_{11}O_{30}$). Another important group is copper(I) delafossites, with the general formula $CuMO_2$, where M is a metal cation in the +3 oxidation state, such as Fe, Co, Cr, Rh, Al, Sc, In, or Ga. Cu(II)-based oxides include copper(II) spinels with the general formula CuB_2O_4 that have a tetragonal unit cell where B is a trivalent metal cation (e.g., Al, Bi, Co, Cr, Fe, Ga, Mn). Additionally, copper(II) wolframites, with monoclinic or triclinic unit cells and the general formula $CuBO_2$ (B = Mn, W), are notable compounds. Other Cu(II)-based compounds include copper niobates (e.g., $Cu_3Nb_2O_8$, $CuNb_2O_6$) and copper vanadates (e.g., CuV_2O_6, $Cu_2V_2O_7$, $Cu_3V_2O_8$, $Cu_{11}V_6O_{26}$).

Cu-based quaternary oxides have been studied less but hold potential. Examples include $Ag_2Cu_2O_3$, Cu_2BiVO_6, $CuBiW_2O_8$, $CuAlGaO_4$ and Cu_2BiVO_6. Although there are indications that the insertion of a second or third cation into the frame of copper oxide frame can stabilize the compound from photocorrosion, there is still controversy on this aspect. Nevertheless, Cu-based ternary and quaternary oxides provide greater flexibility in tuning band structures and optoelectronic properties compared to Cu_2O or CuO. These mixed-metal oxides exhibit diverse structural features and bandgap values ranging from ≈1.2 to 3.1 eV, allowing coverage of the entire solar spectrum through the creation of solid solutions or composite systems.

A wide range of methods has been employed to synthesize Cu-based mixed-metal oxides, including solid-state synthesis, solution combustion synthesis, hydrothermal/solvothermal

© 2025 The Author(s). Advanced Functional Materials published by Wiley-VCH GmbH

16163028, 0, Downloaded from https://advanced.onlinelibrary.wiley.com/doi/10.1002/adfm.202502901 by EMBRAPA - Empresa Brasileira de Pesquisa Agropecuaria, Wiley Online Library on [06/06/2025]. See the Terms and Conditions (https://onlinelibrary.wiley.com/terms-and-conditions) on Wiley Online Library for rules of use; OA articles are governed by the applicable Creative Commons License

methods, sol–gel processes, co-precipitation, electrodeposition, spray pyrolysis, and chemical vapor deposition. The Maggard group has conducted extensive research on the synthesis and application of Cu(I)-based mixed-metal oxides, like $CuNbO_3$,[148, 149] Cu_3VO_4,[150] $Cu_2Ta_4O_{11}$,[151] and $Cu_5Ta_{11}O_{30}$[152] prepared by solid-state method, and $Cu_2Nb_8O_{21}$ nanoparticles synthesized through a solvothermal reaction between CuCl and Li_3NbO_4. Liu et al. prepared $CuFeO_2$ microcrystals with a cubic size of around 1.47 µm by hydrothermal method under 180 °C for 24 h. The prepared $CuFeO_2$ microcrystals showed a multi-band spectral absorption feature, which showed good photocatalytic degradation and purification activity.[153]

For Cu(II)-based compounds, Wang et al. have prepared nanoporous $CuBi_2O_4$ by electrodeposition with subsequent annealing method, with the film thickness tailored by varying the deposition time.[154] Well-crystallized $CuBi_2O_4$ nanoparticles were obtained with optimized charge transfer properties for CO_2 reduction by tuning the thickness of the $CuBi_2O_4$ film. Furthermore, $CuBi_2O_4$ film nanoporous was coated with a gradient TiO_2 layer to regulate the activity and selectivity for CO_2 reduction, with the thicker TiO_2 layer showing the highest CO_2 reduction product yield and the thinner TiO_2 layer with the highest CO selectivity.[155] Deng et al. prepared $Ag_2Cu_2O_3$ nanowires via a facile co-precipitation method. It was mentioned that Cu···Ag Lewis acid-base dual sites on the {110} surface of $Ag_2Cu_2O_3$ played a key role in the formation of the Ag···C═O···Cu intermediate for CO_2-to-CH_4 conversion. Tian et al. prepared hydroxyl-enriched $CuFe_2O_4$ via a solvothermal method, with tetrahedral Cu sites and adjacent bridging hydroxyls working as dual Lewis acid sites.[156] Solution combustion synthesis is a common method to prepare copper(II) spinels.[157] Li et al. applied a sol-gel combustion method to synthesize $CuFe_2O_4$ and coupled it with g-C_3N_4.[158] A type-II heterojunction was formed with a band gap of 1.33 eV for $CuFe_2O_4$. The ultimate g-C_3N_4/$CuFe_2O_4$ composite exhibited excellent photocatalytic performance for the degradation of propranolol.

2.3. Cu-Based Sulfides

2.3.1. Cu-Based Binary Sulfides

Copper sulfides represent a significant class of photocatalysts due to their versatility, low toxicity, and efficient light absorption properties. These materials encompass a range of phases from Cu-rich to copper-deficient structures, denoted as Cu_xS ($1 \leq x \leq 2$). Their narrow bandgaps, ranging from 1.2 to 2.0 eV, enable efficient visible light absorption and excellent plasmonic behavior. Generally, Cu_xS comprises eight distinct compositions, including covellite (CuS), yarrowite ($Cu_{1.12}S$), spionkopite ($Cu_{1.40}S$), geerite ($Cu_{1.60}S$), anilite ($Cu_{1.75}S$), digenite ($Cu_{1.80}S$), djurleite ($Cu_{1.96}S$), and chalcocite (Cu_2S). Due to the presence of Cu vacancies in the lattice ($1 < x < 2$), Cu_xS exhibits p-type semiconducting behavior. High-quality Cu_xS nanoparticles are critical for photocatalytic applications, and various synthesis techniques have been developed to achieve specific compositions and phases, including hydro/solvothermal synthesis, wet chemical synthesis, spray pyrolysis, ion exchange, co-precipitation, and chemical vapor deposition.

The bandgap values of Cu_xS decrease with increasing Cu content, ranging from 2.0 eV for CuS to 1.2 eV for Cu_2S. Therefore, tailoring the Cu_xS composition is an effective way to tune the optoelectronic properties. Generally, the composition of Cu_xS is tuned by controlling the Cu:S molar ratio in the precursor.[159–164] For example, copper sulfides Cu_xS (x = 1.8, 1.84, 1.86, 1.90, 1.92, 1.94, and 1.96) were achieved by solid-state reaction,[161] and $Cu_{1.61}S$ and $Cu_{1.81}S$ nanocrystals were synthesized by varying the Cu:S ratio during the hot injection process.[160] Further, Cuevas et al. utilized a spray pyrolysis method to prepare Cu_xS thin films, with the Cu:S ratio jointly tuned by temperature and the precursor ratio.[162]

Additionally, the Cu:S ratio in Cu_xS can also be adjusted post-synthesis while retaining the original size and shape of the nanoparticles. For example, Xie et al.[165] prepared $Cu_{1.1}S$ nanoplates using a heat-up procedure. The Cu:S ratio was then gradually increased from 1.1:1 to 2:1 through a reaction with $\{Cu(CH_3CN)_4\}PF_6$ in a methanol/toluene mixture. The overall reaction was $Cu_{1.1}S + 2\gamma Cu(I) \rightarrow Cu_{1.1+\gamma}S + \gamma Cu(II)$. This approach allowed the preparation of Cu_xS with various compositions while maintaining the nanocrystals' morphology. Similarly, Jiang et al.[164] prepared Cu_9S_8 via a solvothermal method and further obtained Cu_7S_4 and CuS by adjusting the redox atmosphere, using KBH_4 and $SnCl_4$, respectively, to post-treat Cu_9S_8.

Furthermore, other methods have also been employed to fine-tune the Cu:S ratio in copper sulfide nanocrystals. For instance, Cu_xS nanocrystals with monodispersed sizes were synthesized by sulfurizing Cu(II)-alkyl-amine complexes using dodecanethiol-solvated sulfur.[163] The chemical composition of the Cu_xS nanocrystals was effectively tuned by varying the alkylamine species used in the reaction. Interestingly, solvents also play a crucial role in modulating the Cu:S ratio. Wang et al.[166] prepared copper sulfides (CuS, Cu_7S_4, Cu_9S_5) via a solvothermal method, with stoichiometry controlled by adjusting the volume of ethylene diamine. The solvent volume, along with reaction temperature and time, significantly influenced the formation of various morphologies, such as the hexagonal snowflake-like Cu_7S_4.

The size and morphologies, such as nanosheets, nanoparticles, nanowires, spheres, nanoplates, etc., can be precisely controlled by adjusting reaction conditions. The hot injection method is widely recognized for producing well-dispersed, small crystals with uniform and well-defined morphologies.[167–169] Cu_2S nanodots (3-6 nm) and nanodisks were prepared via a one-pot hot injection method.[167] The aspect ratio (up to 2.0), thickness, and diameter of the nanodisks were tuned by varying reaction parameters such as temperature, duration, surfactant concentrations (tri-n-octylphosphine oxide), and precursor concentrations (cuprous acetate (CuOAc) and dodecanethiol). Furthermore, Cu_2S/CuS hetero-nanocrystals have also been prepared through a one-step hot injection approach, leveraging in-situ self-heterogenization.[170] Specifically, Cu_2S nanocrystals grew in situ on the (101) and (102) facets of CuS nanocrystals. This precise facet alignment facilitated efficient charge separation and transfer, enhancing the hetero-nanocrystals' photocatalytic performance.

Kamazani et al.[171] prepared Cu_2S, Cu_2S/CuS, and CuS using co-precipitation and hydrothermal methods, exploring factors such as temperature, surfactant, solvent, concentration, Cu precursor, and sulfide source. These parameters significantly

© 2025 The Author(s). Advanced Functional Materials published by Wiley-VCH GmbH

16163028, 0, Downloaded from https://advanced.onlinelibrary.wiley.com/doi/10.1002/adfm.202502901 by EMBRAPA - Empresa Brasileira de Pesquisa Agropecuaria, Wiley Online Library on [06/06/2025]. See the Terms and Conditions (https://onlinelibrary.wiley.com/terms-and-conditions) on Wiley Online Library for rules of use; OA articles are governed by the applicable Creative Commons License

influenced the morphology and particle size, resulting in diverse nanostructures, including nanospheres, nanoflowers, nanorods, and nanosheets. Moreover, microwaves have been frequently used to assist and accelerate the nucleation and growth of copper sulfides during the hydro/solvothermal process. For example, Kim et al.[172] successfully obtained CuS nanoplatelets with a diameter of 13.2 nm using this approach in air.

1D copper sulfide nanowires can be obtained using various strategies, such as hydrothermal synthesis of Cu_2S nanowires on the Cu substrate by reacting sulfur powder with Cu foil,[173] Cu_2S nanowires with diameters of 2–6 nm obtained from polymerized Cu-thiolate by solventless thermolysis method,[174] CuS nanowire grown on a Cu mesh through a liquid-solid reaction,[175] Cu_xS nanowires by sulfuring the Cu nanowires at various temperatures,[176] {100}-oriented CuS nanowire from electrodeposition,[177] and CuS nanowires with 40–80 nm in diameter prepared from Cu-dithiooxamide by hydrothermal method.

Additional unique morphologies have been achieved through tailored synthesis methods. For instance, CuS nanoflowers were prepared via a polyol route, where ethylene glycol acted as a capping agent for the formation of nanoflowers.[178] Similarly, rose-like CuS microflowers were produced via a solvothermal process in N,N-dimethylformamide (DMF), with the solvent's low viscosity playing a critical role in morphology formation.[179] Adding PVP to the reaction medium led to the formation of CuS microspheres and multiplates.

Chemical bath deposition has been used to fabricate Cu_xS thin films with varying phases, such as Cu_2S, $Cu_{1.75}S$, $Cu_{1.12}S$, and CuS, alongside morphologies including nanoplates, nanosheets, nanospheres, and nanoflowers. The concentration of L-cysteine was a key parameter in controlling the morphology.[180] Stam et al. demonstrated that in situ converted Sn(IV)-thiolate complexes from additive $SnBr_4$ could serve as a shape-directing agent to control the size, shape, and crystal structure of Cu_xS polyhedral nanocrystals.[181] By varying the $SnBr_4$ concentration, hexagonal bifrustums, bipyramids, and nanoplatelets with diverse aspect ratios were achieved.

2.3.2. Cu-Based Multinary Sulfides

The structure, bandgap, and performance of binary copper sulfides depend heavily on their stoichiometry, morphology, and size. Introducing additional elements into the Cu-S framework to form Cu-based multinary sulfides with a wide variety of stoichiometries offers enhanced flexibility for tuning electronic and optical properties. This enables better performance tailored to specific applications. It was reported that incorporating foreign atoms into Cu-based systems is often valence-specific, and it is incompatible with divalent cations.[182] Instead, it is common to incorporate trivalent and tetravalent cations into the structure to form a compound. Examples of such incorporation include metals from the p-block (e.g., Al, Ga, In, Ge, Sn, Sb, Bi) and d-block (e.g., Fe, Co, Ni, Zn). Consequently, a wide variety of Cu-based ternary and quaternary sulfides have been identified, with applications spanning photocatalysis and other advanced fields.

In photocatalysis, ternary nanocrystals such as I-III-VI_2 (e.g., $CuInS_2$, $CuGaS_2$), I-IV-VI_2 (e.g., Cu_2SnS_3, Cu_3GeS_3), I-V-VI (copper antimony sulphide, like $CuSbS_2$, Cu_3SbS_4, Cu_3SbS_3, $Cu_{12}Sb_4S_{13}$; copper bismuth sulphide like Cu_3BiS_3, $CuBi_3S_5$, $Cu_4Bi_4S_9$) and I-IV-VI (copper tin sulphides like Cu_2SnS_3, Cu_3SnS_4, Cu_4SnS_4, $Cu_4Sn_7S_{16}$) have been widely studied. Additionally, quaternary systems such as I-II-III-VI (e.g., CuZnInS, CuZnGaS), I-II-IV-VI (e.g., Cu_2ZnSnS_4, Cu_2ZnGeS_4), and I-III-IV-VI (e.g., $CuInSnS_4$, Cu_3GaSnS_5) expand the range of Cu-based multinary sulfides.

Since the composition and size of Cu-based sulfides are closely tied to their optoelectronic properties, considerable efforts have been dedicated to the controllable synthesis of these multinary sulfides. The synthetic methods significantly impact their morphology, size, crystal phase, and composition. Factors such as precursor, capping agents, reaction temperature, and reaction duration play critical roles in achieving precise control of the Cu-based multinary sulfides. Similar to binary Cu sulfides, synthesis methods such as hot injection, solvothermal/hydrothermal, electrodeposition, and spray pyrolysis have been extensively utilized for their synthesis.

Ternary Cu-III-VI_2 nanocrystals, such as $CuInS_2$, $CuGaS_2$, and $CuSbS_2$, are particularly popular semiconductors due to their narrow band gaps. For example, $CuInS_2$ typically adopts a chalcopyrite structure at room temperature, whereas wurtzite and zinc blende phases become stable at higher temperatures. Pan et al.[183] synthesized nearly monodisperse Cu-In-S nanocrystals with tunable Cu/In ratios, crystalline structures, and particle sizes ranging from 2 to 30 nm via the hot-injection method. The zinc blende and wurtzite structure were achieved by using a capping agent of oleic acid and dodecanethiol, respectively. The commonly used chalcopyrite-type $CuInS_2$ with diverse morphologies have been prepared using various approaches, such as nanoparticles by microwave heating process using sodium sulfide as a sulfur source in ethylene glycol,[184] monodisperse spherical hierarchical architectures by one-pot solvothermal route,[185] thin films by electrodeposition followed by sulfurization processes,[186] and 2D–3D hierarchical structure by soft-template-assisted hydrothermal synthesis.[187] Interestingly, cation exchange offers a powerful strategy to gradually transform binary Cu_2S into ternary $CuInS_2$ and subsequently into quaternary CuInZnS. Akkerman et al.[188] demonstrated a three-step cation exchange process for this transformation. Cu_2S nanocrystals were first synthesized, followed by the incorporation of In3+ to replace Cu+ by a cation exchange process to form $CuInS_2$. Then, a second cations exchange was carried out to introduce Zn^{2+} to replace Cu^+ and In^{3+}, yielding CuInZnS nanocrystals.

The synthesis of stoichiometric Cu-based quaternary sulfides presents significant challenges due to the tendency for secondary phases, such as binary and ternary compounds, to form concurrently. Among these, Cu_2ZnSnS_4 (CZTS) stands out as one of the most extensively studied quaternary semiconductors, owing to its high absorption coefficient ($\approx 10^4$ cm^{-1}), direct bandgap (≈1.4–1.5 eV), and composition of non-toxic, cost-effective, and earth-abundant elements. CZTS has been synthesized using various methods, including hot injection, hydrothermal/solvothermal, sol–gel, and microwave techniques, resulting in nanoparticles with diverse sizes and morphologies.

CZTS exhibits various crystal phases, primarily the tetragonal kesterite-type and stannite-type structures, both derived from a tetragonal zinc blende parent structure, as well as the

© 2025 The Author(s). Advanced Functional Materials published by Wiley-VCH GmbH

16163028, 0, Downloaded from https://advanced.onlinelibrary.wiley.com/doi/10.1002/adfm.202502901 by EMBRAPA - Empresa Brasileira de Pesquisa Agropecuaria, Wiley Online Library on [06/06/2025]. See the Terms and Conditions (https://onlinelibrary.wiley.com/terms-and-conditions) on Wiley Online Library for rules of use; OA articles are governed by the applicable Creative Commons License

hexagonal wurtzite-type structure. The kesterite and stannite phases are thermodynamically more stable and are, therefore, the most widely studied. Achieving a single-phase CZTS requires meticulous control over reaction conditions, as factors like solvents and ligands significantly influence the resulting crystal phase. For instance, long-chain alkanethiols such as dodecanethiol have been shown to promote the formation of wurtzite CZTS by acting as both a sulfur source and a surfactant. CZTS nanoparticles with a hexagonal wurtzite structure have been synthesized using dodecanethiol and oleylamine as sulfur sources and organic ligands.[189]

The more commonly studied kesterite-type CZTS has been prepared using various methods. In 2009, Riha et al. synthesized nearly monodisperse kesterite CZTS nanocrystals (12.8 ± 1.8 nm) by injecting sulfur and metal precursor solutions in oleylamine into hot trioctylphosphine oxide at 300 °C.[190] With a different hot-injection order, kesterite CZTS, Cu_2CoSnS_4, and Cu_2NiSnS_4 nanocrystals with an average diameter of 18.0 ± 5.0 nm were obtained by injecting the sulfur-oleyamine solutions into the hot metal precursors solutions in oleyamine at 280 °C. These nanocrystals demonstrated excellent potential for photocatalytic H_2 evolution.[191] Kesterite Cu_2MgSnS_4 nanoparticles (14.7 ± 3.8 nm) were synthesized using a similar hot-injection method at 230 °C, where the sulfur precursor was injected into hot metal precursors dissolved in oleylamine.[192] Via a different method, Ansari et al. achieved uniform kesterite CZTS nanoparticles (≈7 nm) using a hydrothermal method with oleic acid as a surfactant.[193] In a different work, CZTS nanoparticles (20–30 nm) were solvothermally prepared in ethylene glycol, demonstrating a highly controllable size and morphology.[194]

2.4. Cu-Based Halide Perovskites

Metal halide perovskites have emerged as a highly promising optoelectronic semiconductor. Various Cu-based halide perovskites have been explored for advanced photocatalysis. Their attractive properties—such as high absorption coefficients, long carrier diffusion lengths, tunable bandgaps, and low-cost solution processability—have driven intense research interest over the past decade. Compared with traditional oxide photocatalysts, the synthesis of Cu-based halide perovskites is relatively facile as the preparation condition is mild and can mostly be conducted with a high yield at room temperature with no calcination process. During the past decade, rapid progress has been made in developing synthesis methods, which include solid mechanical synthesis, thermal injection, solution method, anti-solvent method, and solvent evaporation method.

2.4.1. Solid Mechanical Synthesis

The solid mechanical synthesis strategy involves mixing precursors and mechanically grinding them, which might be the most rapid, simplest, and scalable method without largely using solvents. The synthesis can proceed on laboratory and industrial scales by well-mixing precursors with a stoichiometric ratio using mortar or ball milling. For example, Grandhi et al. grounded CsI and CuI with a molar ratio of 3:2 and 1:2 for 5–10 min to synthesize composition-tunable $Cs_3Cu_2I_5$ and $CsCu_2I_3$, respectively (**Figure 4a**). This method can be scaled up proportionally to obtain scales of several hundred grams and exhibits sufficient environmental stability.[195]

To achieve more uniform mixing and automatical synthesis, Xie et al. synthesized gray-white $Cs_3Cu_2Cl_5$ powder with good thermal and photostability by ball milling CsCl and CuCl at a speed of 1000 rpm for 30 min (Figure 4b).[196] Updated from traditional ball milling methods, Zheng et al. reported a mechanical-assisted sintering technique for the preparation of high-quality perovskite.[197] Similarly, Ren et al. mixed precursor materials and ball-milled them overnight at 100 °C to prepare $Cs_3Cu_2X_5$, $CsCu_2X_3$ (X = Cl, I), $Cs_5Cu_3Cl_{8-x}I_x$, and $Cs_3Cu_2Cl_{5-x}I_x$ powders, further improving the crystallinity and phase purity of the materials (Figure 4c).[198]

Although solid-state mechanical synthesis can be used to prepare halide perovskites, the resulting products are often bulk materials with non-uniform dimensions. Furthermore, variations in preparation conditions—such as raw material quality and mechanical processing parameters—can lead to significant fluctuations in the performance of the synthesized halide perovskites.

2.4.2. Hot Injection Method

The hot injection method provides a more controlled route to achieve uniform sizes and morphologies for preparing perovskite nanoparticles and quantum dots (QDs). The controllable size and morphology and high crystallinity can be attained by tuning the synthesis conditions, such as temperature, reaction time, and precursors. Moreover, long-chain organic ligands (aliphatic carboxylic acids and amines) are frequently used to alter reaction kinetics, affect nucleation rates, and passivate surface defects of nanocrystals (**Figure 5a**).[199] According to a recent study from Le et al., different chain-length ligands can be used to control the size and shape of $Cs_3Cu_2Br_5$ nanocrystals during thermal injection. The short ligand (C_6) induces irregularly shaped dispersed nanoparticles, the longer ligands (C_9 and C_{18}) can form smaller nanocubes and nanospheres, and the combination of C_6/C_9 and C_9/C_{18} ligands can form rectangular nanosheets and nanospheres (Figure 5b).[200]

Meanwhile, the injection temperature also has a significant impact on the size and morphology of perovskite nanocrystals. Cheng et al. found that, with the same proportion of precursor added, the product can be controlled to be zero-dimensional (0D) $Cs_3Cu_2I_5$ or one-dimensional (1D) $CsCu_2I_3$ by adjusting the temperature to 100 or 70 °C, respectively (Figure 5c).[201] Moreover, the type of precursor also affects the crystal structure of Cu-based halide perovskites. Gao et al. enhanced the thermal injection method by introducing InI_3 to the precursor solution. While the In^{3+} ions did not incorporate into the $Cs_3Cu_2I_5$ crystal lattice, their presence led to a gradual decrease in the size of the $Cs_3Cu_2I_5$ nanocrystals. This modification prevented excessive crystal growth, which can lead to the loss of colloidal stability in the solvent (Figure 5d).[202]

2.4.3. Solution Precipitation Method

Metal halide perovskites are prone to nucleation and growth upon the precursors are dissolved in the solution. Their

© 2025 The Author(s). Advanced Functional Materials published by Wiley-VCH GmbH

16163028, 0, Downloaded from https://advanced.onlinelibrary.wiley.com/doi/10.1002/adfm.202502901 by EMBRAPA - Empresa Brasileira de Pesquisa Agropecuaria, Wiley Online Library on [06/06/2025]. See the Terms and Conditions (https://onlinelibrary.wiley.com/terms-and-conditions) on Wiley Online Library for rules of use; OA articles are governed by the applicable Creative Commons License

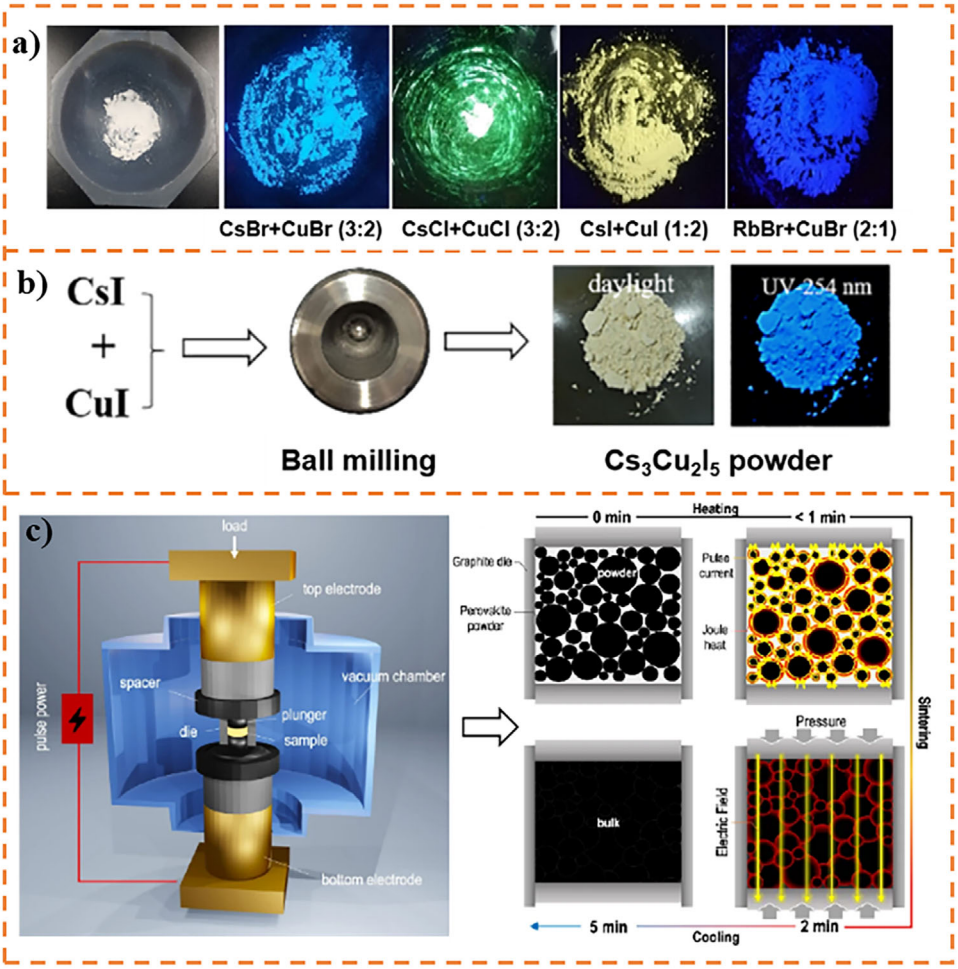

Figure 4. a) Images of powder samples produced by grinding Cs (or Rb) halide and Cu halide at different molar ratios. b) Schematic illustration of the synthetic process of $Cs_3Cu_2I_5$ perovskite powder by using a planetary ball mill. c) The mechanism of synthesizing perovskite using Prototype FAST. a) Reproduced with permission.[195] Copyright 2020, American Chemical Society. b,c) Reprint under the terms of the Creative Common Attribution 4.0 International License.[196, 198]

temperature-dependent solubility is leveraged to achieve supersaturation, thereby inducing solute precipitation through meticulous temperature control. For compounds exhibiting low solubility at room temperature, direct crystallization serves as a straightforward and efficient method for perovskite preparation. Notably, certain metal halide perovskites display inverse solubility behavior, where solubility decreases with increasing temperature. This characteristic has been effectively utilized to grow high-quality perovskite single crystals by cooling saturated solutions, facilitating controlled crystallization processes.

Aamir et al. dissolved $CuCl_2$ in HBr and added an equimolar amount of CsBr, stirred for 1 h, and stored at room temperature for 1 day to synthesize $CsCuBr_3$. For substances with a high coefficient of positive dissolution temperature, the solute can be dissolved at high temperatures.[203] Then, the solution temperature gradually decreases during its growth process, allowing the crystal to continue to grow and attach to the crystal nucleus, forming large and high-quality $CsCuBr_3$ crystals. Yao et al. synthesized high-quality $Cs_3Cu_2I_5$ with an absolute photoluminescence quantum yield PLQY of 97.76% using this cooling crystallization method (**Figure 6a**).[204] Indeed, the hydrothermal method is similar in principle to the cooling crystallization method. Its critical condition creates a high-temperature and high-pressure environment inside the reaction vessel by heating, completely dissolving all the reactants, and then cooling down and crystallizing as the temperature decreases to produce the target product. $CsCu_2I_3$, $CsCuCl_3$, and $CsCuCl_xBr_{3-x}$ have been synthesized via a hydrothermal process (Figure 6b).[205–207]

Although the halide perovskite grown by solution method has accurate composition control, high crystal quality, and good reproducibility, it requires a long growth cycle, high purity of raw materials, high corrosiveness, and environmental impact.

2.4.4. Anti-Solvent Method

The anti-solvent method is particularly effective for the low-temperature synthesis of metal halide perovskites. It allows for the gradual crystallization of perovskite materials in solution by introducing a miscible solvent that reduces their solubility.

© 2025 The Author(s). Advanced Functional Materials published by Wiley-VCH GmbH

16163028, 0, Downloaded from https://advanced.onlinelibrary.wiley.com/doi/10.1002/adfm.202502901 by EMBRAPA - Empresa Brasileira de Pesquisa Agropecuaria, Wiley Online Library on [06/06/2025]. See the Terms and Conditions (https://onlinelibrary.wiley.com/terms-and-conditions) on Wiley Online Library for rules of use; OA articles are governed by the applicable Creative Commons License

16163028, 0, Downloaded from https://advanced.onlinelibrary.wiley.com/doi/10.1002/adfm.202502901 by EMBRAPA - Empresa Brasileira de Pesquisa Agropecuaria, Wiley Online Library on [06/06/2025]. See the Terms and Conditions (https://onlinelibrary.wiley.com/terms-and-conditions) on Wiley Online Library for rules of use; OA articles are governed by the applicable Creative Commons License

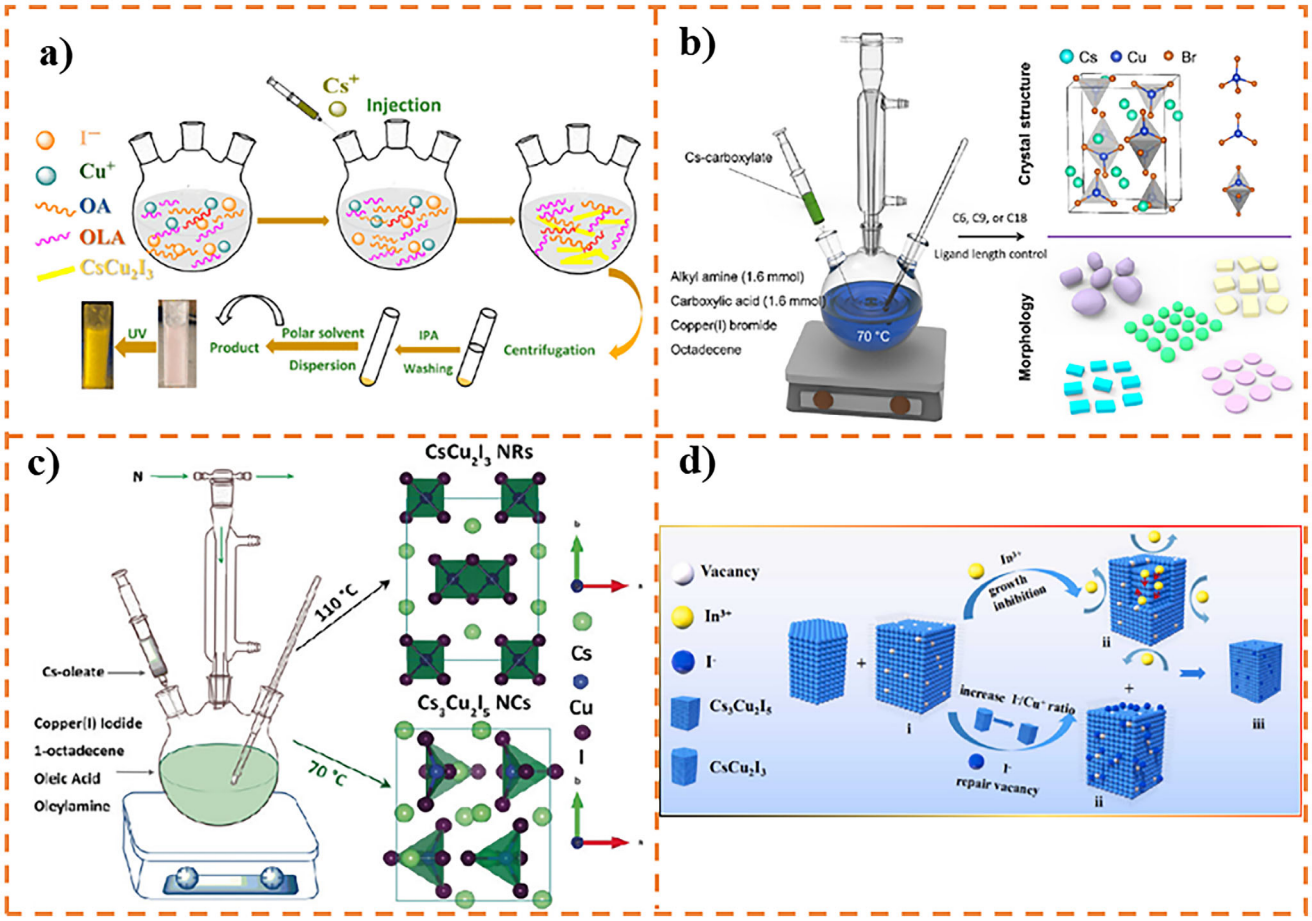

Figure 5. a) Schematic illustration of the synthetic process for cesium copper iodide with different OLA-I stoichiometric ratios through hot-injection technique. b) Hot-injection synthesis of $Cs_2Cu_3Br_5$ nanocrystals using different chain-length ligands. c) Colloidal synthesis of cesium copper halide nanocrystals under different temperatures. d) Schematic diagram of growth mechanism for the InI_3-assisted synthesis of $Cs_3Cu_2I_5$ NCs. a) Reprint under the terms of the Creative Common Attribution 4.0 International License.[199] b) Reproduced with permission.[200] Copyright 2021, American Chemical Society. c) Reproduced with permission.[201] Copyright 2019, John Wiley and Sons. d) Reproduced with permission.[202] Copyright 2022, Elsevier.

Anti-solvent methods are generally classified into two main categories: the gradual crystallization steam-assisted method and the rapid anti-solvent crystallization method. Jun et al. used an anti-solvent steam-assisted crystallization method to prepare $Cs_3Cu_2I_5$ by adjusting and controlling the molar ratio of CsI and CuI.[208] First, CsI and CuI were dissolved in dimethyl sulfoxide (DMSO) and DMF under stirring at 60 °C. Then, methanol (MeOH) was dropped into the solution until the precipitate was no longer dissolved. The saturated solution was filtered and placed in a sealed beaker filled with MeOH. After growing at 60 °C for 48 h, high-quality millimeter-sized crystals were obtained. The anti-solvent vapor-assisted method achieves crystal growth by controlling the solvent, dissolving the solute in a good solvent with high solubility, and diffusing the poorly soluble and volatile poor solvent into the good solvent through heating and other methods, thereby reducing the solubility of the solute in the mixed solution and gradually causing the solute to precipitate and crystallize. On the basis of the anti-solvent steam-assisted crystallization method, a rapid anti-solvent crystallization method has been developed. By rapidly injecting the precursor solution into the anti-solvent, crystals can be quickly obtained in a short period. Cs_2CuBr_4 QDs are mainly obtained through this synthesis method. For example, Dong used an improved anti-solvent method to sonicate stoichiometric amounts of CsBr and $CuBr_2$ in 20 mL DMSO, and then rapidly added the obtained precursor solution to 500 ml IPA under vigorous stirring. Then, centrifuge the solution at 3000 rpm for 3 min to remove large particles, and centrifuge at 10 000 rpm for 5 min to obtain the final product with the desired particle size.[209]

The solvent evaporation method is another widely-used technique that relies on controlling solvent properties to achieve crystal growth. This method involves dissolving the precursor solution in an organic or acidic solvent at a concentration close to saturation, and then slowly evaporating the solvent from the porous container cover at a controllable speed, so that the concentration of the solution is always in a metastable supersaturated state, providing continuous driving force for crystal growth. $Cs_2Cu\ (Cl_xBr_{1-x})_4$ was prepared by Huang et al. using the solvent evaporation method. First, CuX_2 and CsX (X = Cl, Br) were mixed in a molar ratio to obtain a series of halide aqueous solutions. Then, the solvent was slowly evaporated at 40 °C to obtain crystals of different colors and sizes within about 10 days.[210]

© 2025 The Author(s). Advanced Functional Materials published by Wiley-VCH GmbH

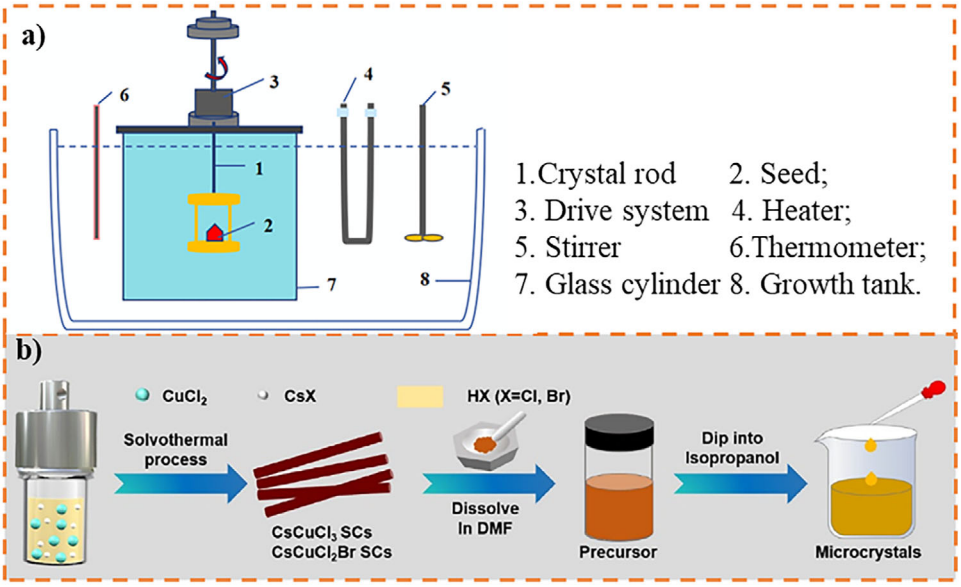

Figure 6. a) Schematic diagram of a device for $Cs_3Cu_2I_5$ crystal grown by solution method. b) Schematic diagram of the synthesis route of $CsCuCl_3$ and $CsCuCl_2Br$ MCs. a) Reproduced with permission.[204] Copyright 2022, John Wiley and Sons. b) Reproduced with permission.[205] Copyright 2022, American Chemical Society.

It should be noted that the solvent evaporation method is suitable for solutes with high solubility but low or even negative temperature coefficients. Compared to the cooling crystallization method for preparing single crystal samples, the constant temperature solvent evaporation method is more convenient in controlling growth conditions, but it requires maintaining high-temperature stability.

2.5. MOFs and COFs

MOFs and COFs are classes of highly porous materials forming two- or three-dimensional structures.[211–213] MOFs are formed by coordination bonding between metal nodes and organic linkers,[214] while COFs are formed by covalent bonding between organic linkers.[215] The structures and properties of these frameworks can be fine-tuned using different metal nodes and/or organic linkers.[216, 217] Pore size and physicochemical properties can be controlled by varying linker chain length,[218] introducing functional groups,[219] and using different symmetry combinations.[220]

MOFs and COFs electronic structures are formed by molecular and atomic orbitals, entirely dissimilar to the conventional semiconductor photoactive materials. Thus, a typical mechanism of MOFs and COFs photoexcitation can be described as a photostimulated charge transfer mechanism[221] (see **Figure 7**) rather than the photogeneration of free charge carriers. It results in the relatively short lifetime of the excited states and limited access to the photoinduced active sites for the reagent molecules.

To enhance MOFs and COFs sensitivity toward visible light and to create purposefully active sites, various modification strategies have been proposed. For example, the introduction of visible light sensitizers or the incorporation of visible light photocatalyst nanoparticles (nanoclusters) into the MOF structure (see **Figure 8**)[222] or the creation of a single atom or single site catalyst by incorporation of metal atoms or clusters into COF structure (**Figure 9**).[223–225]

Another widely used strategy to enhance the overall photoactivity of both MOFs and COFs is the formation of composites and heterostructures with conventional semiconductors such as metal oxides and g-C_3N_4 to increase charge separation between components. All mentioned strategies are applied for Cu-based MOFs and Cu-containing COFs.[227–229]

In terms of coordination chemistry, copper ions in the bivalent state can be tetra- or hexacoordinated and able to form MOF structures with different linkers. A comprehensive review of the

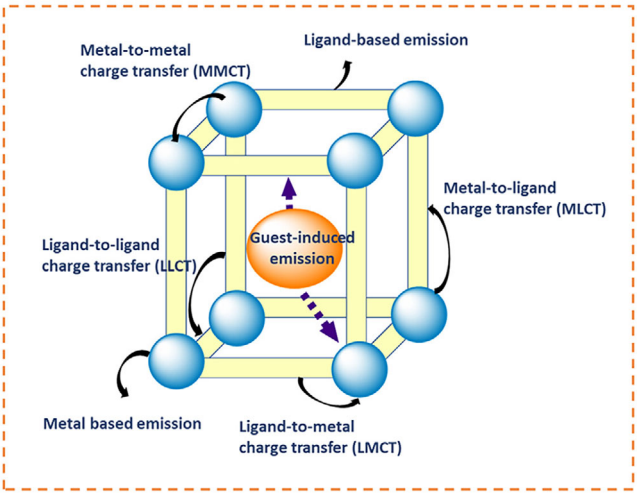

Figure 7. Schematic illustration of some possible photoinduced reaction pathways in MOFs. Reproduced under the terms of the Creative Common Attribution 4.0 International License.[221]

© 2025 The Author(s). Advanced Functional Materials published by Wiley-VCH GmbH

16163028, 0, Downloaded from https://advanced.onlinelibrary.wiley.com/doi/10.1002/adfm.202502901 by EMBRAPA - Empresa Brasileira de Pesquisa Agropecuaria, Wiley Online Library on [06/06/2025]. See the Terms and Conditions (https://onlinelibrary.wiley.com/terms-and-conditions) on Wiley Online Library for rules of use; OA articles are governed by the applicable Creative Commons License

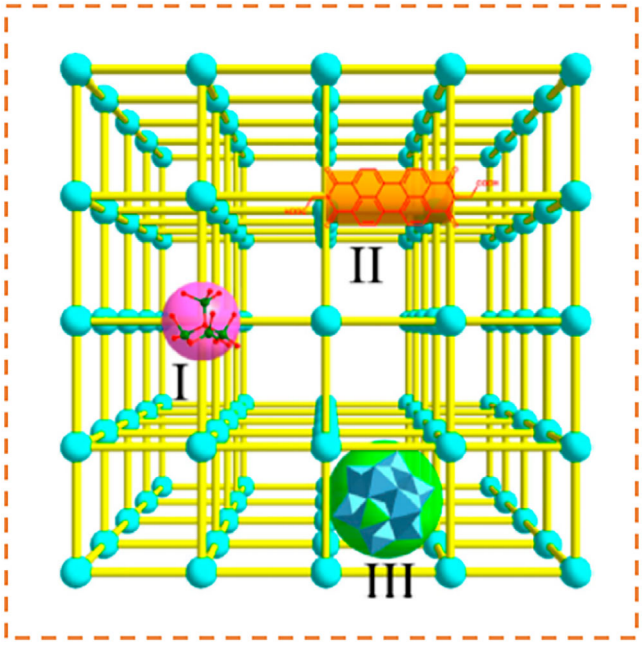

Figure 8. Scenarios of MOFs application as photoactive materials: I) MOFs photoexcitation, II) photosensitizer incorporation, III) host matrix for the visible light photocatalyst nanoparticles. Reproduced with permission.[226] Copyright 2016, American Chemical Society.

design of different types of Cu-based MOFs and their design is given elsewhere.[230] If the metal centers are unsaturated, copper acts as a good catalyst for various catalytic reactions. HKUST-1 is one of the most studied materials from the MOFs class based on Cu. In particular, HKUST-1 is a promising material for catalytic applications because the assembly of building blocks produces secondary building units of petals-type containing open metal sites acting as Lewis acid sites. Remarkably, HKUST-1 is deeply blue-colored (**Figure 10**), and therefore, one can expect to observe its catalytic activity under visible light irradiation. However, to the best of our knowledge, there have been no reports about HKUST-1 activity in solar fuel production yet.

At the same time, publications are demonstrating photochemical activity in CO_2 reduction for other Cu-MOFs. Deng et al. reported that $Cu_3(BTC)_2$ could be conformally and uniformly deposited on Cu_2O photocathode to form $Cu_2O/Cu_3(BTC)_2$ heterostructure to enhance the efficiency and stability of Cu_2O for photocatalytic reduction of CO_2 to CO.[231] The photocatalytic CO production rate at $Cu_2O/Cu_3(BTC)_2$ electrode (16 µmol h^{-1} at −1.97 V) was four times higher than that on bare Cu_2O photocathode in organic solvent when using TBAPF6 (tetrabutylammonium hexafluorophosphate) as supporting electrolyte. In addition, the $Cu_2O/Cu_3(BTC)_2$ photocathode showed better stability than bare Cu_2O under visible light irradiation, preventing rapid photocorrosion of the Cu_2O surface.

Albo and coworkers reported copper-based MOFs supported on gas diffusion electrodes to accelerate the electrocatalytic conversion of CO_2 to alcohols.[232] Four different synthesized MOFs were formed: 1) HKUST- 1 MOF, $[Cu_3(m6\text{-}C_9H_3O_6)_2]_n$; 2) CuAdeAce MOF, $[Cu_3(m_3\text{-}C_5H_4N_5)_2]_n$; 3) CuDTA mesoporous metal-organic aerogel, $[Cu(m\text{-}C_2H_2N_2S_2)]_n$; 4) CuZnDTA MOF, $[Cu0_{.6}Zn_{0.4}(m\text{-}C_2H_2N_2S_2)]_n$. These electrodes are characterized by relatively large surface area, high availability of Cu catalytic centers, and favorable electrocatalytic activity for CO_2 reduction with efficient production of methanol and ethanol in the liquid phase. The electrocatalytic reduction activity was carried out in an electrochemical filter press cell under ambient conditions. Faraday efficiencies of the electrodes for CO_2 conversion were 15.9% for HKUST-1, 1.2% for CuAdeAce, and 9.9% for CuZnDTA at a current density of 10 mA cm^{-2}. HKUST-1 and CuZnDTA–based electrodes exhibited stable electrocatalytic performance for 17 and 12 h, respectively. This work provides insights into the design of efficient electrocatalysts for CO_2 reduction, including "paddle wheel" motifs that exhibit square-planar coordination geometries around Cu(II) centers and create open metal sites for strong interaction with guest species through a porous framework.

Wang et al. reported a realization of the Z-scheme mechanism in the heterostructure consisting of Cu-based MOF photosensitizer (PCN-224(Cu), which was prepared from CuTCPP and $ZrCl_4$) and TiO_2 nanoparticles (x% PCN-224(Cu)/TiO_2, where x is the weight percentage of TiO_2) for the photocatalytic CO_2 photoreduction to CO.[233] The excited electrons can be transferred from the conduction band of TiO_2 to the interface between PCN-224(Cu) and TiO_2 to recombine with the photogenerated holes in the HOMO of PCN-224(Cu), preventing the recombination of electrons and holes generated in PCN-224(Cu) and TiO_2, respectively. As a result, the photocatalytic CO_2 conversion rate of 15% PCN-224(Cu)/TiO_2 (37.21 µmol $h^{-1}g^{-1}$) in aqueous solution without additional cocatalyst and sacrificial agent was 10 times and 45.4 times higher than that of bare PCN-224(Cu) and TiO_2, respectively.

X. Han et al. synthesized a copper-based MOF (CUST-804) using a bulky tetraphenylethylene-tetrazole linker and demonstrated its photocatalytic activity for CO_2 reduction. CUST-804 exhibits CO production activity up to 2.71 mmol g^{-1} h^{-1} with a selectivity of 82.8%.[234] Theoretical calculations demonstrated that only the 5-coordinated Cu site is active for CO_2 reduction, in which the *COOH intermediate is stabilized and CO is readily desorbed.

More details about the application of Cu-based MOFs for CO_2 reduction can be found elsewhere.[227, 228, 230] Cu also behaves as an active single-site catalyst being incorporated in different COF structures.[225, 235] W. Su and coauthors recently reported a novel Cu-based covalent organic framework (CuN_2O_2-COF) with Cu-N_2O_2 single sites.[235] In this study, CuN_2O_2-COF exhibited superior CH_4 production efficiency in CO_2 reduction, with the Faradaic efficiency of CH_4 formation as high as 85.4%. Theoretical calculations indicated that compared with the Cu-N_4 or Cu-O_4 sites in a typical single-site catalyst, the new Cu-N_2O_2 configuration in CuN_2O_2-COF increased the d-band center of the Cu sites and enhanced the adsorption of key intermediates (*COOH and *CHO) required for CO_2 reduction to CH_4.

M. Dong et al. reported the preparation of a metal-cluster-based covalent organic framework (CuABD).[236] The reported yield of 1.3 mmol g^{-1} h^{-1} for formic acid (HCOOH) under simulated solar irradiation demonstrates a synergetic effect of Cu cluster and COF combination due to an efficient charge transfer between diamine monomer and cyclic trinuclear copper (I) units, and the electron delocalization of the π-conjugated framework.

© 2025 The Author(s). Advanced Functional Materials published by Wiley-VCH GmbH

16163028, 0, Downloaded from https://advanced.onlinelibrary.wiley.com/doi/10.1002/adfm.202502901 by EMBRAPA - Empresa Brasileira de Pesquisa Agropecuaria, Wiley Online Library on [06/06/2025]. See the Terms and Conditions (https://onlinelibrary.wiley.com/terms-and-conditions) on Wiley Online Library for rules of use; OA articles are governed by the applicable Creative Commons License

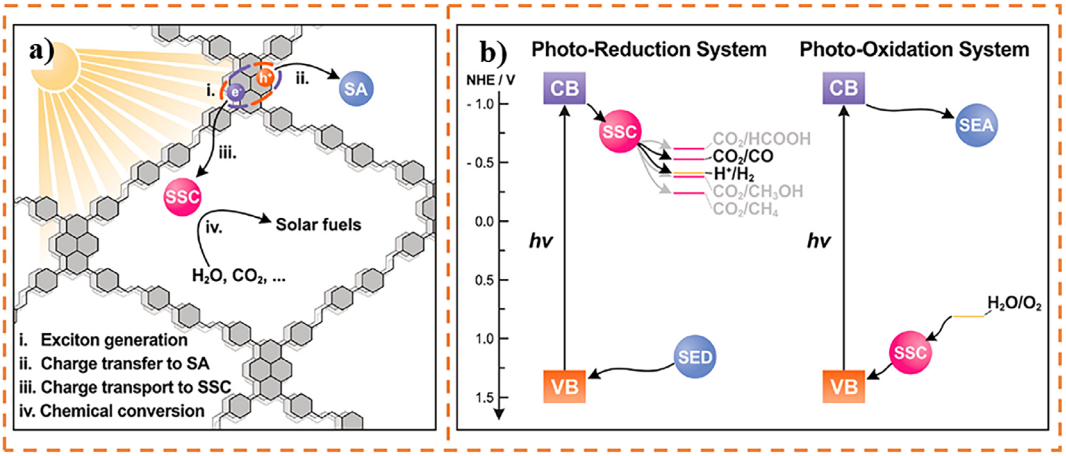

Figure 9. *a)* Schematic illustration of the main processes for solar-to-fuel conversion with COFs as single-site photocatalysts. b) energetic requirements for the COFs applied to photocatalytic solar-to-fuel conversion and the equilibrium potentials vs NHE (pH *7*) of the reduction and oxidation half-reactions. SSC, single-site catalyst; SA, sacrificial agent; SEA, sacrificial electron acceptor; SED, sacrificial electron donor; CB, conduction band; VB, valence band. Reprint under the terms of the Creative Common Attribution 4.0 International License.[223]

Q. Zhao et al. reported a synthesis of a tandem electrocatalyst consisting of Cu nanoclusters dispersed among the isolated Cu single atoms in the COF network for CO_2 to CH_4 conversion.[237] They proposed that CO_2 is first reduced to CO over the atomically isolated Cu single-atom sites, followed by diffusion onto the neighboring Cu nanoclusters for further reduction into CH_4.

Thus, summing up, we can conclude that the development of Cu-based MOFs and Cu-incorporated COFs for CO_2 reduction is currently in progress, and the major trends of the progress are the creation of composite and heterostructured materials for MOFs and the design of Cu single catalytic sites incorporated in COF structures.

2.6. Cu as a Modifier of Other Structures

Besides Cu-based structures, there is a range of remarkable materials where Cu is a modifier of a given catalyst, i.e., as a dopant or single-atom. In both cases, Cu is frequently the active catalyst site, which highlights its importance.

Figure 10. Photography of Cu-based MOF HKUST-1.

2.6.1. Cu-Doped Semiconductor

Doping has emerged as a pivotal technique in catalysis to address the limitations of pristine catalysts, such as wide band gaps, rapid recombination of photogenerated electron-hole pairs, and slow surface reaction kinetics. Doping involves incorporating foreign elements into the host semiconductor without altering its fundamental structure. Typically, dopant metals introduce impurity levels, which modify the electronic and optical properties of the host material by reducing the band gap and enhancing visible light absorption. Moreover, dopants can serve as electron traps to promote charge separation and create new active sites for catalytic reactions.

Among the various metal dopants, including Pt, Ni, Co, Zn, Mn, Cu, and Fe, Cu has gained prominence as an effective dopant for catalytic applications. Cu doping in semiconductors, such as TiO_2, ZnO, and MOFs, introduces defect states that enhance light absorption and charge separation, significantly improving catalytic efficiency. There are various ways to dope Cu into the host materials. Cu doping is typically achieved through one-step or in situ methods, often integrated with the synthesis of the host material. The synthesis technique significantly influences the doping process and the resulting material properties.

The sol–gel method is a widely used low-temperature technique for nanoparticle synthesis and is frequently employed to prepare Cu-doped materials. For example, Cu-doped TiO_2 is commonly synthesized via the sol–gel process, where precursors for TiO_2 and Cu are dissolved simultaneously in a solvent, followed by calcination at optimal temperatures. Several studies have adopted this approach to synthesize Cu-doped TiO_2.[238–240] It has been observed that the choice of Cu precursor influences the crystalline phase of the resulting TiO_2 when preparing a Cu-doped TiO_2 system.[241] By using copper chloride, brookite was obtained in high concentrations.

© 2025 The Author(s). Advanced Functional Materials published by Wiley-VCH GmbH

16163028, 0, Downloaded from https://advanced.onlinelibrary.wiley.com/doi/10.1002/adfm.202502901 by EMBRAPA - Empresa Brasileira de Pesquisa Agropecuaria, Wiley Online Library on [06/06/2025]. See the Terms and Conditions (https://onlinelibrary.wiley.com/terms-and-conditions) on Wiley Online Library for rules of use; OA articles are governed by the applicable Creative Commons License

In contrast, copper sulfate with a 10 wt% concentration predominantly forms anatase as the primary phase. Another work by Tseng et al. further highlighted the effect of Cu precursors on the characteristics and photoactivity of Cu-doped TiO_2.[242] The work demonstrated that Cu-doped TiO_2 synthesized using copper chloride exhibited better Cu dispersion and superior activity in CO_2 photoreduction than that prepared with copper acetate. The microwave-assisted sol–gel method has been utilized to produce Cu-doped TiO_2 co-doped with nitrogen (N).[243] This method offers advantages such as fast heating rates, consistent heating, and shorter processing times, which reduce the required calcination period. The resulting nanosized spherical anatase TiO_2 exhibited enhanced photocatalytic performance for dye degradation. In addition to TiO_2, the sol–gel method has been successfully applied to synthesize other Cu-doped systems, including Cu-doped ZnO,[244–246] Cu-doped ZnS,[247, 248] and other metal oxides.[249, 250]

The hydrothermal or solvothermal methods are also a general way to prepare Cu-doped materials. These techniques involve chemical reactions conducted at elevated temperatures and pressures in a sealed steel autoclave containing a specific solvent. For instance, Cu^{2+} was successfully incorporated into NH_2–MIL-125 using an in situ solvothermal approach. This doping enhanced the electron density at the Cu active site due to the reconstructed directional charge transfer within the Ti-O-Cu framework, ultimately improving NH_3 production efficiency.[251] Similarly, Cu^{2+} was doped into the core of the porphyrin ring in PCN-224, forming metalloporphyrin–MOFs via a simple hydrothermal process.[252] The doped Cu^{2+} effectively trapped photogenerated electrons and suppressed electron-hole recombination, leading to enhanced photocatalytic performance. Li et al. reported the hydrothermal synthesis of Cu^{2+}-doped $SrTiO_{3-\delta}$ nanosheets, followed by an in situ reduction of partial Cu^{2+} to Cu^0 under an H_2 atmosphere.[253] This process resulted in dual-functional Cu (Cu^0/Cu^{2+})-modified $SrTiO_{3-\delta}$ nanosheets, exhibiting remarkable photothermal catalytic performance for CO_2 reduction and H_2 evolution.

In addition to the methods mentioned above, various other techniques have been employed to uniformly dope Cu into the host materials, including the precipitation method,[254] solid-state reaction method, impregnation, spin coating, flame spray pyrolysis, and ammonia-evaporation-induced synthetic method.[255]

Cu dopants can substitute specific atoms in a host material, known as substitutional doping, or occupy interstitial positions, depending on the system under investigation. For instance, in halide perovskite systems, Feng et al. successfully doped Cu into $Cs_3Bi_2Br_9$ hexagonal nanoplates using a one-step mechanochemical synthesis approach. XRD, DFT calculations, and Raman spectra confirmed that the Cu dopant occupied the Cs sites rather than substituting Bi or residing in interstitial lattice positions.[256] In contrast, in $CsPbI_3$[257] and $CsPbBr_3$[258] systems, Cu was reported to replace Pb atoms. However, doping behavior can vary significantly. For example, when Tailor et al.[259] attempted to substitute Ag with Cu in double perovskite $Cs_2AgBiCl_6$, they found that Cu incorporated interstitially instead of replacing Ag.

Additionally, while doping often does not alter the crystal structure of the host material, it can sometimes induce phase transitions in perovskites. Such phase changes can degrade material quality but, in some cases, lead to efficient composite structures for photocatalysis. For instance, Li et al.[260] developed a Cu-doped dual-phase $CsPbBr_3$-Cs_4PbBr_6 nanocomposite via an in-situ transformation strategy. Initially, $CsPbBr_3$ was synthesized using a hot-injection method. Subsequently, cupric acetylacetonate, as a Cu source, was introduced into a 1-octadecene (1-ODE) solution containing tri-n-octylphosphine oxide at 300 °C. The incorporation of Cu led to the formation of Cs_4PbBr_6, creating a Cu-doped dual-phase $CsPbBr_3$-Cs_4PbBr_6 system. This composite exhibited a 4.2-fold enhancement in photocatalytic CO_2 reduction efficiency compared to pristine $CsPbBr_3$ nanoparticles.

While uniform doping of Cu into the host material through the aforementioned methods has its advantages, it can sometimes lead to material instability or an increased rate of charge recombination. To mitigate these challenges, many studies have shifted their focus towards introducing Cu as a surface-active site rather than as a bulk dopant. In such cases, a postsynthetic cation-exchange reaction is often employed. This approach involves a two-step process: the host material is first synthesized, followed by a separate step to deposit Cu onto its surface. A common technique for this purpose is chemical bath deposition. For example, Wang et al. deposited Cu onto the surface of BiOCl nanosheets, creating an active site that enriched photogenerated electrons and facilitated the reaction pathway by reducing the activation barrier for CO_2 activation.[261]

Similarly, Arai et al. doped Cu onto the surface of ZnS via a cation-exchange process driven by the difference in ionization tendencies between copper and zinc ions.[262] The surface Cu-doped ZnS exhibited significantly enhanced photocatalytic H_2 evolution performance compared to bulk Cu-doped ZnS.

2.6.2. Cu Single-Atom

Single-atom catalysts (SACs), characterized by individual and isolated metal atoms stabilized on suitable supports, have emerged as a transformative innovation in catalysis. These catalysts offer unparalleled metal atom efficiency and unique catalytic mechanisms compared to conventional catalysts. Specifically, SACs maximize the number of active sites accessible to reactants and intermediates, exhibiting high catalytic activity and selectivity due to their unsaturated coordination environments and distinctive electronic structures. Moreover, their well-defined single-atom active sites provide an ideal platform for further investigating reaction mechanisms. Single-atom catalysts with Cu as the active center represent a cutting-edge advancement in photocatalysis. Compared to traditional Cu-based catalysts, Cu SACs possess highly uniform active sites and well-defined geometric configurations, enabling precise spatial interactions with substrates and superior catalytic performance.

The synthesis of Cu SACs requires precise control to achieve high atom density, robust stability, and the desired electronic structure. Stabilization of Cu single atoms on supports can occur through various mechanisms, such as interaction with surface atoms, substitution of surface atoms, or coordination with organic bridging ligands, depending on the nature of the support. The choice of support material plays a crucial role in stabilizing Cu single atoms and significantly influences the loading method. Various techniques are employed to load Cu SACs onto supports,

© 2025 The Author(s). Advanced Functional Materials published by Wiley-VCH GmbH

16163028, 0, Downloaded from https://advanced.onlinelibrary.wiley.com/doi/10.1002/adfm.202502901 by EMBRAPA - Empresa Brasileira de Pesquisa Agropecuaria, Wiley Online Library on [06/06/2025]. See the Terms and Conditions (https://onlinelibrary.wiley.com/terms-and-conditions) on Wiley Online Library for rules of use; OA articles are governed by the applicable Creative Commons License

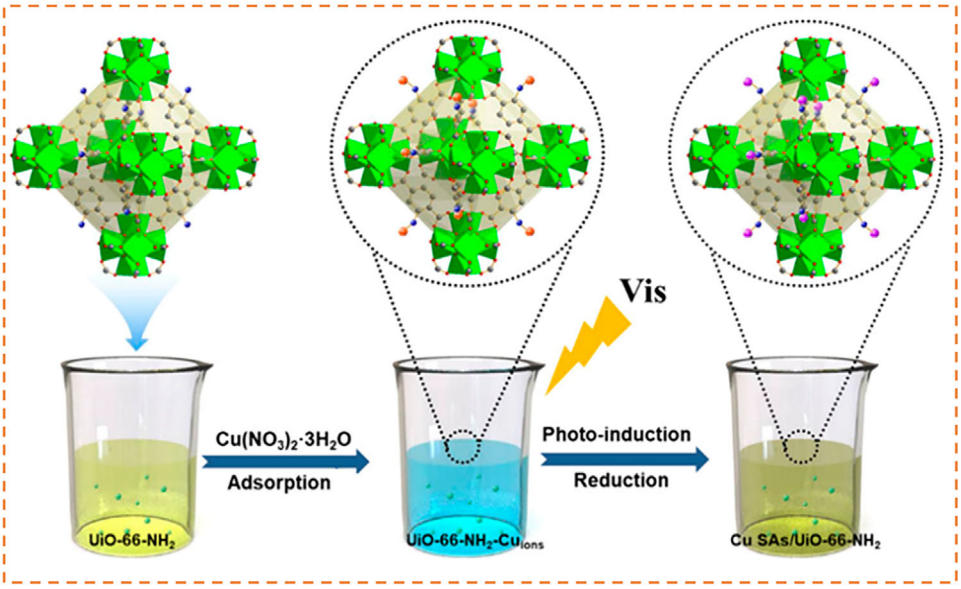

Figure 11. Synthesis process of the Cu SAs/UiO-66-NH_2 photocatalyst. Reproduced with permission.[267] Copyright 2020, American Chemical Society.

ensuring proper stabilization and maximizing their catalytic potential.

Impregnation is a widely used method for loading Cu single atoms onto semiconductors. Semiconductor surfaces typically feature abundant O^{2-}/OH or S^{-}/SH groups and vacancies, which act as anchoring sites for Cu atoms. Cu atoms can directly bond to surface O^{2-}/OH or S^{-}/SH ligands through impregnation or occupy surface cation vacancies, enabling effective stabilization. For example, Li et al. immobilized Cu SACs on the surface of TiO_2 using an impregnation-calcination method, where the single-atom Cu was coordinated with oxygen atoms.[263] The Cu SACs provided additional electron-rich sites, facilitating the co-photoactivation of N_2 and CO_2 and achieving remarkable performance in urea photosynthesis.

In contrast, Lee et al.[264] employed a wrap-bake-peel method to precisely control the Cu atom's location within the Ti vacancies. This process involved coating silica spheres with a sol-gel layer of TiO_2, adsorbing the Cu precursor, applying a silica overlayer, baking at high temperatures, and finally etching away the silica overlayer. The resultant Cu/TiO_2 with Cu atoms occupying Ti vacancies demonstrated a reversible and cooperative photoactivation process.

Recently, Huang et al.[265] developed Cu-ZnS photocatalysts containing dispersed Cu SAs synthesized via impregnation followed by calcination. In this system, Cu SAs were coordinated with sulfur atoms, forming Cu-S-Zn units. These units stabilized the *COHCO intermediate and facilitated its coupling with *CO to generate *COCOHCO, ultimately enhancing CH_3CH_2COOH production. Additionally, impregnation has been utilized to construct Cu/UiO-66 catalysts with Cu atoms anchored at defect sites.[266] In this study, UiO-66 was synthesized with one missing linker per Zr_6 cluster. The Cu atoms were subsequently anchored to the oxygen atoms of —OH/—OH_2 groups, terminating defect sites through impregnation, demonstrating a highly effective approach to stabilizing single-atom Cu within a robust framework.

The photoinduced method is another widely utilized approach for loading Cu SAs onto semiconductor surfaces. For instance, Wang et al. developed UiO-66-NH_2-supported Cu SACs using this method.[267] In their work, Cu species in solution were first adsorbed onto the -NH_2 groups within UiO-66-NH_2, followed by anchoring under visible light irradiation, as illustrated in **Figure 11**. This method effectively anchored Cu SACs, leveraging light-driven processes to achieve strong binding on the MOF support.

Intercalation is a cost-effective strategy to anchor Cu single atoms onto photocatalysts with layered structures. Xiao et al.[268] intercalated Cu single atoms into and between C_3N_4 planes by introducing chlorophyll sodium copper into a supramolecular precursor, followed by controlled pyrolysis. The Cu atoms were shown to coordinate with compositional N atoms (Cu-N_x), forming charge transfer channels that facilitated the separation and transport of charge carriers, significantly enhancing photocatalytic performance.

Pyrolysis is considered one of the most efficient methods for preparing Cu SACs. Duan et al.[269] employed a one-step pyrolysis process to directly anchor single-atom Cu onto CN while generating N vacancies as dual active centers. Specifically, thiourea and copper chloride were used as precursors, followed by high-temperature pyrolysis at 550 °C. In addition to carbon-based materials, MOFs are extensively used as precursors in the pyrolysis method for SACs due to their high porosity and tunable internal structures. For example, MIL-125 was utilized as a precursor, with partial Ti atoms replaced by Cu during the hydrothermal synthesis.[270] Subsequent high-temperature pyrolysis resulted in mesoporous TiO_2 with Cu SAs anchored on its surface, demonstrating excellent catalytic performance.

In another interesting study, Da Silva et al.[271] synthesized a crystalline carbon nitride, poly(heptazine imide) (PHI), through the thermal treatment of melamine and NaCl, yielding Na-PHI. For the sample preparation, an aqueous suspension of Na-PHI and the metal chloride precursor (CuCl) were mixed. After the

© 2025 The Author(s). Advanced Functional Materials published by Wiley-VCH GmbH

16163028, 0, Downloaded from https://advanced.onlinelibrary.wiley.com/doi/10.1002/adfm.202502901 by EMBRAPA - Empresa Brasileira de Pesquisa Agropecuaria, Wiley Online Library on [06/06/2025]. See the Terms and Conditions (https://onlinelibrary.wiley.com/terms-and-conditions) on Wiley Online Library for rules of use; OA articles are governed by the applicable Creative Commons License

metal coordination, the material was washed. The XRD patterns indicated that the cation exchange reactions do not considerably change the structure of carbon nitride.

Cu-N-C Single-Atom: The dynamic structure of N-doped C-supported metal SACs (M-N-C), particularly Cu-N-C single-atomic catalysts, is a significant feature in electrochemical processes, setting them apart from other catalysts.[272] Cu-N-C single-atomic catalysts have remarkably performed in various electrochemical reactions, especially in CO_2 reduction. The process of reconstruction of these catalysts during electrochemical reactions is a critical aspect that affects their performance and stability. However, there is still a gap in understanding how to assess this dynamic stability during operational conditions.[272–274]

For instance, Bai et al. have studied the dynamic stability of Cu–N_4–C SAC during CO_2RR using computation methods and experimental applications.[273] They have reached a few conclusions: 1) as the electrode potential becomes negative, the adsorption of hydrogen at the nitrogen sites intensifies; 2) hydrogen adsorption serves as a crucial factor for the mobilization of copper single atoms from the catalyst surface during electrolysis, probably diminishing the kinetic barrier to Cu mobilization; 3) following the detachment of a subset of copper atoms, transient small clusters are formed with adjacent copper atoms, which facilitate the electroreduction of CO_2 to ethanol; 4) upon reaction completion or positive potential adjustment, the oxidation of Cu is significantly accelerated by hydroxyl radicals, followed by redeposition, ultimately restoring the Cu clusters to their initial atomically dispersed state, thus completing the copper catalyst reconstruction cycle.

This reconstruction's reversible nature is particularly noteworthy. This dynamic behavior highlights the importance of evaluating catalyst stability under realistic reaction conditions.

3. Applications of Cu-Based Catalysts

Energy and environmental issues have long been among humanity's most pressing challenges. Due to their excellent light absorption and catalytic properties, Cu-based catalysts have demonstrated remarkable potential across various applications to address these challenges. This section highlights the latest research progress on Cu-based catalyst applications, such as CO_2 reduction, water splitting, N_2 fixation, and oxidation reactions, including the degradation of organic pollutants and organic synthesis.

3.1. CO_2 Reduction

Several approaches are already available to mitigate the amount of CO_2 in the atmosphere, such as carbon capture and storage (CCS), electrochemical and thermochemical conversion, photoelectrochemical processes, photocatalytic reduction, and biological fixation.[275, 276] Although CCS is a well-studied approach with recognized effectiveness, its challenges include the risk of leakage in geological deposits and the costs associated with compression and transportation.[277] Similarly, biological fixation of CO_2 by microalgae, while promising, faces limitations related to enzyme production and regeneration.[278]

On the other hand, the catalytic conversion of CO_2 into CH_4 and CO, using transition metals as catalysts, is seen as a promising and effective option in terms of technological applicability. The technique of CO_2 reduction employs a catalyst to convert CO_2 and water into solar fuels and chemicals such as CH_4, CO, methanol (CH_3OH), formic acid (HCOOH), and formaldehyde. It is desirable to foster these reactions to C_{2+} products (e.g., oxalic acid, ethanol, etc.), where the CO_2 abatement would be more efficient and, consequently, the potential for effective carbon sequestration. The transformation of CO_2 into fuels and chemicals offers an additional energy-storage strategy that can strategically contribute to expanding the energy matrix.[23, 279–281] In conclusion, CO_2 catalytic reduction can solve two global problems: energy generation and decreasing CO_2 concentration in the atmosphere.

Catalysis involving cascade CO_2 reduction reactions has also begun to emerge. In this process, the product generated from one catalytic step serves as the reactant for the subsequent step. This approach integrates multiple catalytic steps within a single reactor or system, enabling the sequential conversion of intermediates This entire sequence occurs in either a spatially defined arrangement within a catalytic material or a temporally controlled manner within a reaction system, ultimately leading to the conversion of CO_2 into more complex and valuable chemical products.[282–285] This strategy draws inspiration from natural enzymatic cascades, where enzymes, either as individual units or as multienzyme complexes, facilitate multistep transformations with remarkable efficiency and selectivity. In enzymatic systems for methanol synthesis, CO_2 is reduced to formate, then formaldehyde, and finally methanol, each step catalyzed by specific enzymes.[278]

Carbon monoxide (CO) is a crucial intermediate in many CO2RR cascade reactions, particularly for multicarbon product formation. The initial step often involves selective CO_2 reduction to CO on catalysts like Ag, Au, or modified copper. Subsequent steps involve CO adsorption and activation on a second catalytic site, often copper, for C-C coupling to form C_{2+} products. In-situ spectroscopic techniques and theorical calculations are crucial for elucidating reaction mechanisms and identifying transient intermediates.[284, 286]

Theaker et al. demonstrated a two-step electrochemical cascade system using heterogeneous catalysts to convert CO_2 to ethanol.[283] In this system, CO_2 was first reduced to CO using an Ag-nanocoral catalyst, and then CO was reduced to ethanol using an oxide-derived Cu catalyst. The authors found that excluding CO_2 from the second-stage electrolyzer was critical for maintaining appreciable ethanol selectivity. Despite the limited conversion of the intermediate CO between cascade steps, the system produced ethanol with a faradaic efficiency of 11.0% at an average applied potential of −0.52 V vs RHE, demonstrating the potential of cascade systems for electrochemical reduction of CO_2 to liquid fuels.

Lian et al. developed a ternary composite material (CTU/CdS-P25) for high-efficiency photocatalytic CO_2 reduction. The composite was synthesized by inserting TiO_2 particles into CdS grains to form CdS-P25 and then integrating this composite with a mixed-ligand-based MOF, CuTCPPcUiO-66 (CTU). The resulting CTU/CdS-P25 composite showed broadened light absorption and enhanced delivery of photo-induced carriers, leading to a CO production rate of 2.38 μmol h^{-1}, which is significantly higher than that of UiO/CdS-P25 and CdS-P25. The authors proposed a cascade electron transfer mode within the heterojunction

© 2025 The Author(s). Advanced Functional Materials published by Wiley-VCH GmbH

16163028, 0, Downloaded from https://advanced.onlinelibrary.wiley.com/doi/10.1002/adfm.202502901 by EMBRAPA - Empresa Brasileira de Pesquisa Agropecuaria, Wiley Online Library on [06/06/2025]. See the Terms and Conditions (https://onlinelibrary.wiley.com/terms-and-conditions) on Wiley Online Library for rules of use; OA articles are governed by the applicable Creative Commons License

structure, which suppresses the recombination of carriers and enhances photocatalytic behavior.

Thus, despite significant progress, challenges remain in achieving high selectivity, Faraday efficiency, and stability for desired products while suppressing HER. Long-term catalyst stability under industrial conditions needs improvement.

3.1.1. CO_2 Photoreduction

CO_2 stands as an exceptionally stable covalent molecule (C═O), $\Delta H \approx 800$ kJ mol^{-1}) with a linear configuration and net dipole moment of zero, presenting minimal opportunities for electron transfers and chemical transformations.[287] Among the candidates for converting CO_2, heterogeneous photocatalysis in CO_2 photoreduction emerges as a promising alternative, as highlighted in the literature, as it allows CO_2 to deviate from its linear form, creating dipole moments and inducing chemical reactivity.[287, 288]

The initial research on heterogeneous photocatalysis dates back to Markham.[289] However, with the studies conducted by Fujishima and Honda,[290] this process gained greater prominence, solidifying itself as a continuously evolving area of interest. Due to its unique characteristics, heterogeneous photocatalysis has found applications in various sectors, such as environmental remediation of dyes,[291, 292] pharmaceuticals,[293, 294] and pesticides.[295, 296] Subsequently, it was realized that the mechanism of photocatalysis could be employed in the photoreduction of CO_2, also known as artificial photosynthesis.[297]

The first reported work on the photocatalytic reduction of CO_2 into other products was conducted by Inoue et al.[298] This study utilized various semiconductors, including WO_3, TiO_2, ZnO, CdS, GaP, and SiC, with CO_2 photoreduction tests performed in water. TiO_2, ZnO, CdS, GaP, and SiC generated formic acid, formaldehyde, and methyl alcohol. The authors observed that as the negativity of the material's conduction band increased, more methyl alcohol was produced.

In CO_2 photoreduction, the adsorption of CO_2 molecules plays a crucial role in determining the selectivity of the formed products. Both adsorption and activation processes are critical for product generation and suppressing competitive reactions. Typically, there are three initial pathways of CO_2 product formation, as depicted in **Figure 12a**. Despite the linear structure of gaseous CO_2 and its lack of a dipole moment, each oxygen atom within it possesses a lone pair of electrons, capable of donation to surface Lewis acid centers, illustrated in bend – I. Moreover, the carbon atom gains electrons from Lewis base centers, such as oxide ions, leading to the formation of a carbonate-like species, as depicted in bend – II. Lastly, the CO_2 molecule can function as both an electron donor and acceptor simultaneously, forming mixed coordination products, illustrated in bend – III. This initial adsorption process tends to alter the linear geometry of CO_2, causing the molecule to lose its linear symmetry, subsequently reducing the reaction barrier.[299] The redox potentials of different byproducts were compiled in **Table 1**.[300]

CO_2 photoreduction reaction involves various steps, as depicted in Figure 12b. Initially, electrons are excited upon absorbing photons with energy equal to or greater than the material's band gap, transitioning from the valence band (VB) to the conduction band (CB), forming a hole in the VB and an electron in the CB (1). In the subsequent step, electron-hole pairs overcome the Coulombic force, facilitating their separation and transfer to the surface reaction sites. The recombination of electron-hole pairs consistently occurs during the charge transfer process within or on the catalyst's surface, significantly constraining catalytic activity (2).[301] The final and pivotal step encompasses reactants (CO_2 and H_2O) adsorbed on the surface undergoing a redox reaction with electrons and holes, forming various carbon-based

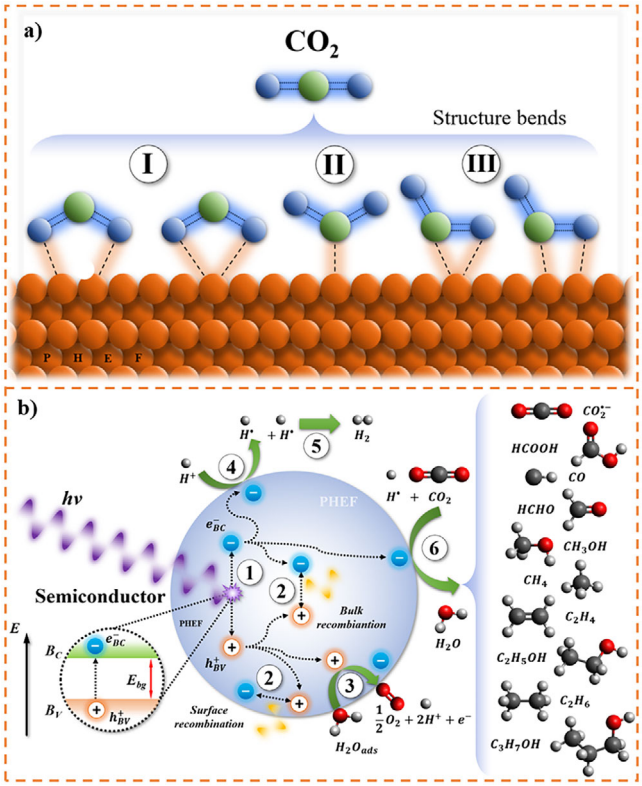

Figure 12. Mechanism of CO_2 adsorption onto the semiconductor surface (a) and photoreduction process (b). These schemes were composed of a compilation of information from references.[303–306]

Table 1. CO_2 photoreduction into diverse products and the associated redox potentials (vs NHE at pH 7).[300, 309]

Product	Reaction	E^0 (V vs NHE)
Carbon monoxide	$CO_2 + 2H^+ + 2e^- \rightarrow CO + H_2O$	−0.53
Formic acid	$CO_2 + 2H^+ + 2e^- \rightarrow HCOOH$	−0.61
Formaldehyde	$CO_2 + 4H^+ + 4e^- \rightarrow HCHO + H_2O$	−0.48
Methanol	$CO_2 + 6H^+ + 6e^- \rightarrow CH_3OH + H_2O$	−0.38
Methane	$CO_2 + 8H^+ + 8e^- \rightarrow CH_4 + 2H_2O$	−0.24
Acetaldehyde	$2CO_2 + 10H^+ + 10e^- \rightarrow CH_3CHO + 3H_2O$	−0.36
Ethylene	$2CO_2 + 12H^+ + 12e^- \rightarrow C_2H_4 + 4H_2O$	−0.34
Ethanol	$2CO_2 + 12H^+ + 12e^- \rightarrow C_2H_5OH + 3H_2O$	−0.33
Ethane	$2CO_2 + 14H^+ + 14e^- \rightarrow C_2H_6 + 4H_2O$	−0.27
Oxygen	$H_2O \rightarrow 1/2O_2 + 2H^+ + 2e^-$	+ 0.81
Hydrogen	$2H^+ + 2e^- \rightarrow H_2$	−0.42

© 2025 The Author(s). Advanced Functional Materials published by Wiley-VCH GmbH

16163028, 0, Downloaded from https://advanced.onlinelibrary.wiley.com/doi/10.1002/adfm.202502901 by EMBRAPA - Empresa Brasileira de Pesquisa Agropecuaria, Wiley Online Library on [06/06/2025]. See the Terms and Conditions (https://onlinelibrary.wiley.com/terms-and-conditions) on Wiley Online Library for rules of use; OA articles are governed by the applicable Creative Commons License

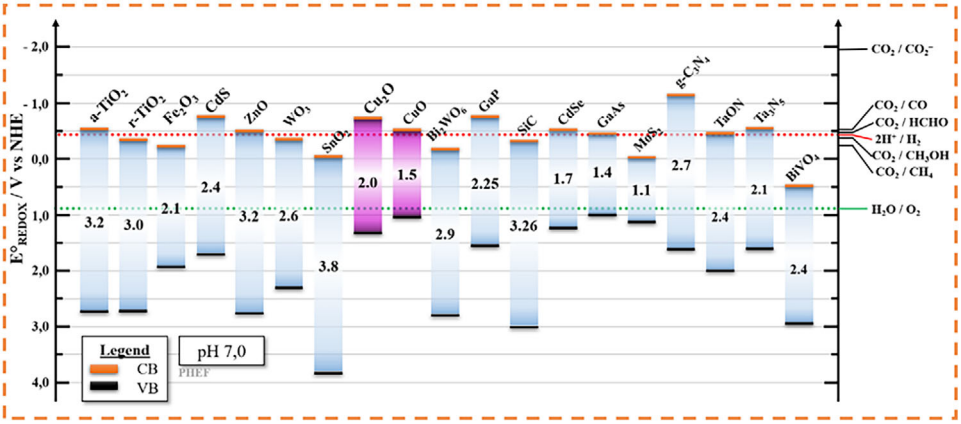

Figure 13. Energy bands of various semiconductors, their reduction potentials, and specific reactions for the process. Observation: a-TiO_2 refers to the anatase phase, while r-TiO_2 denotes the rutile phase. This diagram was composed of a compilation of information from references.[321–324]

products (3, 4, and 6). The reaction with water produces H_2, rendering water splitting a competitive process during photocatalytic CO_2 reduction (3, 4, and 5).[302]-

While photocatalytic CO_2 reduction stands as a promising alternative to mitigate atmospheric CO_2 levels, some challenges limit its application. For instance, water splitting emerges as a competitive reaction in photocatalytic CO_2 reduction.[302] Typically, materials utilized in these processes exhibit a high band gap energy in the UV spectrum, rapid charge-combination, low affinity/adsorption for reactants, and photocorrosion.[49, 307, 308] Therefore, seeking the synthesis of materials to overcome these challenges is essential for enhancing their photocatalytic performance.

Numerous materials have been investigated for their potential in CO_2 photoreduction. TiO_2 has been studied due to its stability and bandgap properties,[310] while g-C_3N_4,[311] Fe_2O_3,[312] and CdS[313] are notable for their absorption of visible light. ZnO, characterized by its high surface area and the presence of surface defects and oxygen vacancies, serves as an active site for CO_2 activation[291, 314] WO_3, owing to its intermediate band gap, significant oxidizing power of the valence band holes, and robust stability in both acidic and oxidative conditions, has also garnered attention[315] MoS_2 stands out due to its unique layered structure.[316, 317] In contrast, Nb_2O_5, with its acidic surface, enhances selectivity.[318] Cu_2O is favored for its low cost and earth abundance,[319, 320] while CuO is recognized for its ability to reduce CO_2 to CH_4.[72, 115] The bandgaps of some of the listed materials are summarized in **Figure 13**.

In this context, Cu-based catalysts have received particular attention due to their ability to convert CO_2 into hydrocarbon and alcohol products. Heterostructures with copper oxides have emerged as promising materials for CO_2 photoreduction due to their ability to address the limitations of individual components. Interestingly, Shreya Singh and collaborators modulated the electronic and structural properties of the MoS_2 and Cu_2O heterostructure components. They studied the effect of work function and morphology of the material for CO_2 photoreduction application.[73] Two types of MoS_2 were used: p-MoS_2 with a higher work function and n-MoS_2 with a lower work function and structural defects. Similarly, two types of Cu_2O with slightly different work functions were employed based on their morphology (cubic or cuboctahedron). The study confirmed the n-type conductivity of n-MoS_2 and identified defects, sulfur deficiencies, and oxygen incorporation within its structure. Notably, the choice of MoS_2 and Cu_2O was strategic as each excelled in either CO_2 reduction (Cu_2O) or water oxidation (MoS_2), but not both. An efficient photocatalyst needs both functionalities. Experiments confirmed the low CO_2 reduction activity of the individual components. However, all MoS_2-Cu_2O heterostructures exhibited a 2–5 times increase in CH_3OH yield compared to the isolated catalysts. P-MoS_2-based heterostructures displayed superior activity due to their Z-scheme charge transfer mechanism. In this scheme, photogenerated electrons accumulated on the component with a stronger reduction ability (Cu_2O), while holes accumulated on the component with a stronger oxidation ability (MoS_2). This contrasted with the type-II mode in n-MoS_2-based structures, where the charge distribution was reversed. The Z-scheme effectively suppresses electron-hole recombination and provides stronger redox abilities, leading to higher photoactivity. This finding highlighted the significance of work function in governing charge transfer across the heterostructure interface. Tailoring the work function through different synthesis methods could further enhance photoactivity.

Furthermore, p-MoS_2-Cu_2O-c (with cubic Cu_2O morphology) demonstrated significantly improved activity compared to p-MoS_2-Cu_2O-co (cuboctahedron Cu_2O). This was attributed to the stronger binding energy between {100} facets of Cu_2O-c and {002} facets of MoS_2, as revealed by density functional theory (DFT) calculations. Additionally, differences in electron and hole effective masses obtained through DFT calculations explained lower electron-hole recombination in p-MoS_2-Cu_2O-c, confirmed by electrochemical impedance spectroscopy (EIS) measurements.[73] Their results emphasized the crucial role of work function and morphology in optimizing binding and charge transport within heterostructures.

Hao and coworkers synthesized Z-scheme heterojunctions between Cu_2O and WO_3 through post-hydrothermal treatment of the aqueous solution containing metal precursors.[325] The molar ratio of Cu was varied concerning WO_3, ranging from 5 to 25%. In terms of structure, the hexagonal phase of WO_3 was

© 2025 The Author(s). Advanced Functional Materials published by Wiley-VCH GmbH

16163028, 0, Downloaded from https://advanced.onlinelibrary.wiley.com/doi/10.1002/adfm.202502901 by EMBRAPA - Empresa Brasileira de Pesquisa Agropecuaria, Wiley Online Library on [06/06/2025]. See the Terms and Conditions (https://onlinelibrary.wiley.com/terms-and-conditions) on Wiley Online Library for rules of use; OA articles are governed by the applicable Creative Commons License

identified, and in the samples containing copper, the (111) and (200) planes related to Cu_2O were observed. High-resolution transmission electron microscopy (HRTEM) images unveiled the embedding of Cu particles onto the surface of the WO_3 semiconductor within the nanocomposite, doped with Cu_2O in WO_3, aligning with the diffraction pattern of the nanocomposite. CO_2 photoreduction tests were conducted in a gas-solid heterogeneous reaction mode with H_2O gas, and the resulting gaseous products, including O_2, H_2, CH_4, and CO, were quantified. The results showed that the material did not produce significant values for the sample without Cu (pure WO_3). However, even at the lowest proportion of 5% Cu, a substantial amount of CH_4 and CO was observed, while the amounts of O_2 and H_2 were negligible. Thus, the new material preferred CO_2 reduction over the water-splitting reaction, a positive aspect given the challenges associated with this process. As noted by the authors, doping WO_3 with Cu_2O increased CO_2 adsorption and prevented charge recombination through the migration of photogenerated electrons. The materials maintained a constant production rate over six cycles, surpassing isolated oxides.[325]

Nogueira et al.[326] synthesized Nb_2O_5/CuO heterostructures through the solvothermal method, incorporating commercial Nb_2O_5 power in the CuO synthesis and modifying the molar ratio of CuO and Nb_2O_5 between 2.5 and 10%. CO_2 photoreduction tests were conducted in water. Concerning morphology, the orthorhombic phase of Nb_2O_5 was identified. Due to the low amount of CuO, only two main peals were discerned, namely (−111) and (111). As discussed by the authors, a Z-scheme heterostructure was formed between the oxides, extending the lifetime of photo-generated charges. However, more importantly, the selectivity of the byproducts and the heterojunction formation increased the production of H_3CCOOH in samples with lower CuO content. This underscored the significance of CO formation in generating longer hydrocarbons, indicating that CH_3 and CO should be formed on the same surface. Regarding sample reuse, at the 10% proportion, there was a decrease from the first to the second cycle, yet the amount of CH_4 formed remained constant in subsequent cycles.

Another interesting work by Lei Li et al. described an innovative approach for constructing CuO/Cu_2O S-scheme heterostructures.[327] The central characteristic of this design was the interfacial Cu (II)-O-Cu(I) bridges, which were formed through an in-situ topotactic transformation strategy. The authors described that these interfacial bridges played a crucial role in promoting both the separation of photogenerated carriers and the activation of CO_2 molecules. The Cu (II)-O-Cu(I) bridges acted as efficient channels for transferring electrons from CuO to Cu_2O, leading to improved charge separation. Additionally, these bridges modified the electronic structure of the Cu(I) sites, making them further favorable for CO_2 adsorption and activation. As a result of these combined effects, the CuO/Cu_2O heterostructures exhibited an enhanced CO_2 conversion rate of 22 μmol g^{-1} h^{-1} with a CO selectivity of 94%. This performance surpassed pristine CuO nanosheets, Cu_2O nanosheets, and Cu_2O nanocubes by a wide margin. This work emphasized the potential of interfacial engineering for creating advanced photocatalysts with superior performance. The findings demonstrated the effectiveness of the in-situ topotactic transformation strategy for constructing well-defined interfaces with optimized electronic structures and their critical role in boosting CO_2 photoreduction activity.[327]

Wei Wang and collaborators further demonstrated the feasibility of modulating Cu oxidation states to enhance photocatalytic CO_2 reduction.[142] Their work introduced a novel CuO_X@p-ZnO hybrid catalyst derived from Cu-doped ZIF-8. In this configuration, Cu primarily existed in its oxidized form (CuO). Polycrystalline ZnO (p-ZnO) was a semiconductor sensitizer, absorbing light to generate electrons. These electrons were then transferred to Cu oxide, which acted as the active center for CO_2 reduction. Employing microwave-assisted thermal synthesis, the researchers obtained a dodecahedral-shaped material. HRTEM revealed lattice fringes corresponding to ZnO (100) and (101) planes, as well as CuO (002) planes, confirming the formation of an interface between the two components. Remarkably, this photocatalyst facilitated the generation of CH_4 and C_2H_4 products, exhibiting a selectivity of 32.9% for C_2H_4, a significant advancement over pristine p-ZnO lacking Cu. Additionally, cycling measurements demonstrated minimal activity loss (less than 10%) over four cycles, indicating good material stability.[142]

In the study by Fang et al., the authors investigated the contribution of TiO_2 crystal facets on the photocatalytic reduction of CO_2 using CuOx/TiO_2 heterostructures.[328] The CuOx/TiO_2 photocatalyst was synthesized using TiO_2 nanocrystals predominantly exposing different facets ({001}, {100}, and {101}) as supports. The interaction of CuOx with TiO_2 was found to be strongest in CuOx/ TiO_2 -{001} catalysts. The research demonstrated that under light irradiation, supported CuO species on TiO_2-{001} were photoreduced to stable Cu_2O species, which benefited the photocatalytic CO_2 reduction to CH_4. In contrast, supported CuOx species on TiO_2-{100} and TiO_2-{101} were photoreduced to Cu^0 species, which were less favorable for photocatalytic CO_2 reduction to CH_4. Characterization methods were utilized to investigate the catalysts' physical and chemical properties and helped to understand the interactions between CuOx and TiO_2 and their impact on photocatalytic performance. Photocatalytic activity measurements revealed that CuOx/TiO_2 catalysts exhibited enhanced performance compared to bare TiO_2 nanocrystals, with facet-dependent variations in activity. The study also employed in situ DRIFTS to investigate the photocatalytic reaction mechanism, demonstrating that CO_2 reduction to CH_4 occurred via bicarbonate and carboxyl intermediates on all CuOx/TiO_2 catalysts. Additionally, CO_2 and formate intermediates contributed to the reaction mechanism on CuOx/ TiO_2 -{100} and CuOx/ TiO_2 -{101} catalysts.[328]

In another work, Liu and colleagues studied more complex materials by introducing a novel photocatalyst design, Cu-Pt/TiO_2-CuO, prepared through a two-step process.[329] The synthesis involved the initial preparation of Cu_2O/TiO_2, followed by treatment with a chloroplatinic acid solution. Light illumination during this treatment led to the partial redissolution of Cu_2O nanoparticles on TiO_2 and their subsequent redeposition alongside elemental Pt. Simultaneously, the Cu_2O was oxidized into nanosized CuO clusters. This process resulted in a final surface decorated with bimetallic Cu-Pt clusters, with elemental Cu situated on the exterior, encapsulating the Cu-Pt complex. The studied Cu-Pt/TiO_2-CuO heterojunction demonstrated significantly higher CO_2 reduction activity, producing CO as the main

© 2025 The Author(s). Advanced Functional Materials published by Wiley-VCH GmbH

16163028, 0, Downloaded from https://advanced.onlinelibrary.wiley.com/doi/10.1002/adfm.202502901 by EMBRAPA - Empresa Brasileira de Pesquisa Agropecuaria, Wiley Online Library on [06/06/2025]. See the Terms and Conditions (https://onlinelibrary.wiley.com/terms-and-conditions) on Wiley Online Library for rules of use; OA articles are governed by the applicable Creative Commons License

product at a rate ten times greater than Cu_2O/TiO_2 or Pt/TiO_2. Furthermore, the CuO surface modification enabled this material to respond to CO_2 photoreduction under visible light irradiation. This finding highlighted the potential of Cu-Pt/TiO_2-CuO as a visible-light-driven photocatalyst for CO_2 reduction.[329]

This intriguing design utilized Cu in both its metallic and oxide forms. While copper oxide is a well-established photocatalyst in the literature, metallic Cu can also be employed as a cocatalyst, leveraging its efficient charge transfer capabilities. Additionally, metallic Cu can function as a plasmonic catalyst, exploiting the generation of charges through the LSPR phenomenon.

In addition to using copper oxides in forming heterostructures, metallic Cu can be employed in this type of modification. Thus, utilizing Cu as a cocatalyst in heterostructures is a common strategy for boosting its photocatalytic activity in CO_2 reduction reactions.[142, 330]

In this context, TiO_2 stands out as one of the most employed materials in photocatalytic processes due to its widely used structure in forming heterostructures.[292, 310] As a result, it is common to come across heterostructures involving TiO_2 and Cu-based catalysts. For example, Jinyan and collaborators developed mesoporous TiO_2 with Cu particles anchored and applied it as a photocatalyst for CO_2 conversion to CO and CH_4 under artificial sunlight irradiation.[331] The TiO_2-Cu nano aggregates with varying concentrations of Cu (0 to 7.5%) were obtained through solvothermal route. One of the advantages of this approach is the fine control of the parameters and resulting morphology. Then, SEM images showed TiO_2 and TiO_2-Cu (5%) materials presented similar morphology to aggregated spherical nanoparticles. The elemental mapping of TiO_2-Cu (5%) by EDX showed uniform Ti, O, and Cu distribution. HRTEM measurements identified the lattice fringes corresponding to both TiO_2 (101) and Cu (111) planes, verifying the formation of a heterostructured catalyst. The study reported that incorporating 5% Cu enhanced CH_4 production by 220% during CO_2 photoreduction, which was attributed to a more efficient charge separation and transfer process.[331]

A study led by Torres and colleagues explored the material interaction in TiO_2/Cu heterostructure as a catalyst for CO_2 photocatalysis.[75] This study aimed to address the challenge of the poor stability of Cu-based semiconductors in aqueous environments, which is attributed to parallel oxidation reactions. The synthesis process of the TiO_2/Cu heterostructures involved the immobilization of Cu nanoparticles on TiO_2 surfaces by reducing copper nitrate with sodium borohydride. The proportion of Cu during the synthesis varied from 1 to 30%. Experimental results from CO_2 photoreduction reactions revealed that TiO_2/Cu catalysts demonstrated considerable stability, indicating the beneficial impact of an adequately formed heterojunction on catalyst activity. Experimental results from CO_2 photoreduction reactions highlighted the role of the heterojunction formed between TiO_2 and Cu in enhancing photocatalytic activity. The study pointed out that Cu presence increases the catalytic efficiency and influences the selectivity towards different products, with a particular interest in forming C_{2+} compounds with higher commercial value. The work of Torres et al. demonstrated the importance of optimizing the Cu^0-TiO_2 interface to improve both the efficiency and stability of photocatalysts for CO_2 reduction, offering insights into developing more sustainable and efficient methods for converting CO_2 into valuable carbon-based fuels and chemicals.[75]

Huibin Ge et al. described the synthesis and application of TiO_2 nanotubes with confined, highly dispersed Cu clusters for the photocatalytic reduction of CO_2 and water to light olefins.[332] The authors employed the atomic layer deposition (ALD) technique to achieve their goal. UV-vis diffuse reflectance spectra showed that Cu (100)/TiO_2-RO exhibited enhanced visible light absorption compared to pure TiO_2 nanotubes and Cu (100)/TiO_2. This improved light absorption was attributed to the presence of Cu species. The sample bandgap was calculated, revealing a decrease in the bandgap with the introduction of Cu oxide, indicating a modification of the TiO_2 and a redistribution of its electrical charge. The photocatalytic activity and selectivity of the catalysts were evaluated, and Cu (100)/TiO_2-RO exhibited enhanced efficiency, with the activity and selectivity being highly dependent on temperature. At 150 °C, the catalyst achieved a maximum selectivity of 60.4% for light olefins, primarily ethylene, with a generation rate of 1.52 μmol g^{-1} h^{-1}. However, a further rise in temperature or light intensity resulted in a significant enhancement in methane selectivity. The superior selectivity of this catalyst towards light olefins arose from the optimized heterostructure. This structure was characterized by well-dispersed Cu clusters enriched with Cu(I) species on the surface. Additionally, the authors mention that proper control of the CO_2 and active hydrogen ratio at moderate temperatures and low light intensity facilitated the achievement of high olefin selectivity.[332]

Another emerging approach in CO_2 photocatalysis research is the utilization of plasmonic catalysts. These catalysts comprise metal nanoparticles that exhibit LSPR upon irradiation with appropriate light. This phenomenon leads to generating charge carriers, driving the photocatalytic reaction.[333] Among various metals, Cu exhibits exceptional electrical conductivity, affordability, and a strong LSPR effect. However, rapid charge carrier recombination on the Cu surface significantly hinders its photocatalytic activity. To address this limitation, researchers have strategically introduced other elements into the structure to enhance charge separation. Haiwei Lai et al. investigated this phenomenon using Cu@Co particles and proposed a photocatalytic CO_2 reduction mechanism based on charge transfer from Cu to Co atoms.[334] Although the materials were not semiconductors, this charge transfer mechanism aligned with the principles of heterostructure formation. In this report, the Cu@Co bimetallic catalyst was synthesized by hydrothermal reaction under mild conditions (200 °C, 15h) using different Cu and Co molar ratios. The research also compared the performance of other bimetallic materials like CuNi, CuPb, CuPt, CuAu, and CuRu for CO_2 reduction. Characterization techniques, including HRTEM images and EDS, confirmed the formation of an interface region between Cu (111) and Co (101) planes and provided elemental distribution mapping. Among the tested catalysts, Cu@Co, with a molar ratio of 8.5:1.5, exhibited the highest efficiency. It attained CO yields of 920.28 μmol g^{-1} h^{-1} of CO and a selectivity of 98% during a 12 h test. Notably, isolated Cu nanoparticles synthesized under the same conditions produced less than 500 μmol g^{-1} h^{-1} of CO, demonstrating an expressive drop in its activity within the third hour of the experiment.[333]

He et al. investigated Cu/ZnO heterojunctions as photocatalysts for CO_2 hydrogenation, demonstrating improved

© 2025 The Author(s). Advanced Functional Materials published by Wiley-VCH GmbH

16163028, 0, Downloaded from https://advanced.onlinelibrary.wiley.com/doi/10.1002/adfm.202502901 by EMBRAPA - Empresa Brasileira de Pesquisa Agropecuaria, Wiley Online Library on [06/06/2025]. See the Terms and Conditions (https://onlinelibrary.wiley.com/terms-and-conditions) on Wiley Online Library for rules of use; OA articles are governed by the applicable Creative Commons License

16163028, 0, Downloaded from https://advanced.onlinelibrary.wiley.com/doi/10.1002/adfm.202502901 by EMBRAPA - Empresa Brasileira de Pesquisa Agropecuaria, Wiley Online Library on [06/06/2025]. See the Terms and Conditions (https://onlinelibrary.wiley.com/terms-and-conditions) on Wiley Online Library for rules of use; OA articles are governed by the applicable Creative Commons License

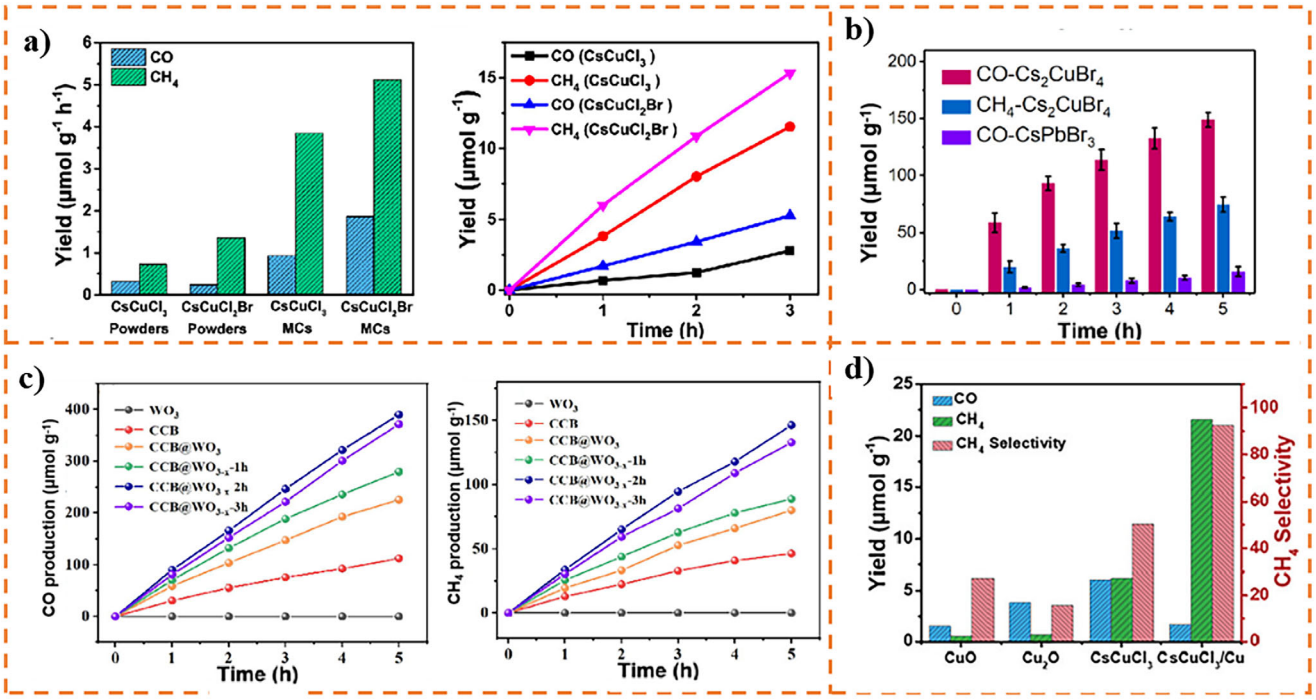

Figure 14. a) Comparison of photocatalytic product yields per hour of synthesized samples; The CO and CH_4 yields of $CsCuCl_3$ and $CsCuCl_2Br$ MCs. b) Time-yield CO and/or CH_4 plots over Cs_2CuBr_4 and $CsPbBr_3$ PQDs. c) Yield of CO and CH_4 over the prepared samples. d) Comparison of the photocatalytic product yield and CH_4 selectivity of catalysts after 3 h of photoreaction under simulated sunlight of 100 mW cm^{-2}. a) Reproduced with permission.[205] Copyright 2022, American Chemical Society. b) Reproduced with permission.[209] Copyright 2022, American Chemical Society. c) Reproduced with permission.[197] Copyright 2024, Elsevier. d) Reproduced with permission.[336] Copyright 2023, John Wiley and Sons.

performance and control over product selectivity by adjusting the Cu/Zn molar ratio.[335] The photocatalyst was prepared using a straightforward precipitation technique followed by calcination in an argon environment containing 5% hydrogen. This catalyst exhibited significantly enhanced CO_2 hydrogenation at 300 °C under light irradiation, achieving a 10.4-fold performance increase compared to the dark reaction. This enhancement was attributed to the synergistic effect of hot electrons generated within the Cu nanoparticles through surface plasmon resonance and photogenerated electrons from ZnO under light excitation. These combined effects facilitate H_2 dissociation and CO_2 activation. The study further revealed that the Cu/Zn molar ratio influenced the selectivity of CO_2 reduction products. By adjusting this ratio, the researchers achieved control over CO and CH_4 production rates. Notably, a 1:1 Cu/Zn ratio yielded only CO at a rate of 300 μmol g^{-1} h^{-1}. Conversely, the sample with a 1:2 ratio solely produced CH_4 at a rate of 51.93 μmol g^{-1} h^{-1}. An intermediate ratio of 1:3 resulted in the formation of both CO and CH_4, with respective rates of 66 μmol g^{-1} h^{-1} and 13 μmol g^{-1} h^{-1}.[335]

Although studies on photocatalytic CO_2 reduction over Cu-based halide perovskites are still in their immature stage, it has already shown their great potential, attributed to the low toxicity of Cu-based halide perovskites compared to Pb-based perovskites. **Figure 14** shows a few product yields for CO_2 photoreduction using Cu-based catalysts.

1D hexagonal $CsCuCl_3$ microcrystals were reported by Kuang et al. Br doping reduces their bandgap and charge transfer kinetics. Compared with bare $CsCuCl_3$, the electron consumption rate of $CsCuCl_2Br$ increased by 1.4 times, and the CH_4 yield (15 μmol g^{-1}) and CO (5.61 μmol g^{-1}) increased by 1.3 times and 2.0 times after 3 h, respectively.[205] Later, 0D Cs_2CuBr_4 QDs were synthesized using an anti-solvent strategy by Dong et al. and employed for solar photocatalytic CO_2 reduction, yielding close to 75 μmol g^{-1} of CH_4 and 149 μmol g^{-1} of CO after 5 h. Their photocatalytic performance surpassed $CsPbBr_3$ QDs prepared under identical conditions, attributed to the microelectronic polarization effect inherent in the Cs_2CuBr_4 QDs.[209]

To promote charge dispersion and improve photoactivity, a coupled Cs_2CuBr_4@WO_3-x catalyst was synthesized by Zhang et al. using an anti-solvent method. The materials exhibited excellent CO_2 photoreduction performance, with an electron consumption rate of up to 390 μmol g^{-1} h^{-1}, three times superior to bare Cs_2CuBr_4. The enhanced performance stemmed from precisely tuning the WO_{3-x} Fermi level through controlled oxygen vacancy concentration. This optimization facilitated efficient charge separation and directed electron transfer within the Cs_2CuBr_4@WO_{3-x} heterojunction.[197] Loading metal ions is also an efficient method for adjusting the bandgap width of perovskite and improving CO_2 reduction performance. The $CsCuCl_3$/Cu heterojunction, developed by Zhao et al. using acid etching solution reaction to in situ load Cu nanocrystals on the surface of $CsCuCl_3$, exhibited an electron consumption rate of about 59 μmol g^{-1} h^{-1}, nearly three times that of single $CsCuCl_3$. It also achieved a remarkable CH_4 selectivity of 92.7%, significantly higher than $CsCuCl_3$ and most lead-free halide perovskites. This enhancement was primarily attributed to the Cu nanocrystals,

© 2025 The Author(s). Advanced Functional Materials published by Wiley-VCH GmbH

which effectively extract photoelectrons, improve charge separation efficiency, and improve CO_2 adsorption and activation.[336]

3.1.2. CO_2 (Photo)Electroreduction

Over the past years, numerous review articles have extensively covered the application of Cu-based catalysts for the electrochemical reduction of CO_2 (CO_2RR), reflecting the dynamic progress and widespread interest in this field. These reviews have provided comprehensive insights into Cu-based systems' underlying mechanisms,[337] material designs,[338] and performance optimizations.[63, 339] However, given the rapid pace of research, it is crucial to highlight the latest developments to provide an updated perspective. This section will focus on key articles published within the last four years to summarize the most impactful contributions and advancements in the design and application of Cu-based catalysts for CO_2RR. It covers electroreduction and photoelectroreduction since the basic aspects of both processes are the same, and they cannot be addressed separately.

Cu-based catalysts have been the focal point of research for CO_2RR due to their unparalleled ability to produce a variety of valuable hydrocarbons and alcohols via multi-electron transfer pathways.[63] Despite their versatility, significant challenges, including high overpotentials, poor selectivity, and catalyst deactivation, have limited their practical application.[340] Recent advancements have sought to optimize Cu catalysts' structural and electronic properties to overcome these barriers, yielding notable improvements in performance metrics such as current density, faradaic efficiency (FE), and long-term stability.[63, 341] Cu-based catalysts for CO_2RR can be broadly categorized into four major classes: monometallic Cu, oxide-derived Cu (OD-Cu), bimetallic Cu alloys, and Cu-based single-atom catalysts. Each class features distinct material properties to address specific challenges in CO_2RR.

One prominent strategy involves nanostructuring Cu metallic to expose specific facets and control particle size, directly influencing the catalytic performance. Studies have demonstrated that Cu(100) surfaces favor forming C_{2+} products, such as ethylene, due to enhanced C-C coupling, while Cu(111) surfaces are more selective for methane generation. Zhang et al.[342] described the production of various Cu(100)-rich films, deposited in GDL substrates, obtained by a designed deposition-etch-bombardment process, allowing for the obtention and control of the Cu(100) facet through the adjustment of the kinetic energy of the bombarding Cu atoms. Three different Cu° films were obtained by adjusting the bombarding power and adding molecular O_2 during bombardment. It was obtained from high electrochemically active surface area electrodes, where the bombardment power directly correlated the exposure of the Cu(100) facet, with the HRS-Cu sample obtaining higher contents of Cu(100). At the same time, LRS-Cu formed mainly with the presence of the Cu(111) facet. Electrochemical assays performed better for the HRS-Cu sample, which could generate C_{2+} products and CO from CO_2 reduction at different applied potentials. It achieved a maximum FE of 86.6% for C_{2+} products, including 58.6% for ethylene. Additionally, scaling up the electrode to a 25 cm^2 MEA system allows the current to reach 12 A, achieving a single-pass yield of 13.2% for C_{2+} products.

Oxide-derived Cu (OD-Cu) has emerged as an auspicious material, retaining unique defect sites and grain boundaries that stabilize intermediates during CO_2RR. The presence of Cu(I) species, either as surface oxides or at Cu(0)/Cu(I) interfaces, has been shown to facilitate the formation of C_{2+} products. In this sense, Jiao et al.[343] reported new insights into the effect of the coordination number (CN) of Cu catalysts on the selectivity of the obtained products of CO_2 reduction. The authors synthesized a series of Cu catalysts by reducing CuO precursors via pulsed electrolysis, cyclic voltammetry, and potentiostatic electrolysis, respectively named Pul-Cu, Cyc-Cu, and Pot-Cu. Through the quantitative fitting of the FT-EXAFS curves, it was shown that the CN obtained for the samples was dependent on the reduction process applied, changing from 12 to 6, respectively. The CO_2 reduction assays show an interesting correlation between the CN of the Cu samples and the obtained reduction product, with the high CN samples generating primarily C_{2+} products, mainly ethylene and ethanol, with the Pot-Cu sample obtaining a FE of 82.5% for C_{2+} products, with a current density of 514.3 $mA.cm^{-2}$, while also achieving no FE for CH_4, at −1.27 V. On the contrary, the low CN sample showed a higher predominance of CH_4 production, with a FE_{CH4} = 56.7%, achieving a current density of 234.4 $mA.cm^{-2}$ at −1.87 V, while also being able to generate C_{2+} products, only with a considerably lower FE of 16.7% (**Figure 15**). X-ray absorption and Raman spectroscopy were employed in situ to investigate *CO adsorption on Cu catalysts with different coordination numbers. The studies revealed distinct adsorption behaviors, influencing the CO_2RR pathway. Liu et al. designed and synthesized oxygen-rich ultrathin CuO nanoplate arrays.[344] These structures were produced through a scalable anodic corrosion method and self-evolve into Cu/Cu_2O heterogeneous interfaces during electrocatalysis. The optimized catalyst demonstrated a high ethylene Faradaic efficiency (84.5%) and a total C_{2+} product Faradaic efficiency exceeding 80%, along with exceptional stability for ≈55 h in a flow cell. Mechanistic analyses revealed that the Cu/Cu_2O interfaces enhance the adsorption of key intermediates, such as *OCCOH, reducing energy barriers for C—C coupling and preserving structural integrity over extended reactions. The neutral KCl electrolyte played a critical role by generating a high local pH and suppressing hydrogen evolution, further improving selectivity and durability. Moreover, the catalyst achieved an ethylene energy efficiency of 27.6% at a current density of 200 mA cm^{-2} in a membrane electrode assembly electrolyzer. These results highlight the potential of Cu-based nanostructured catalysts and mild electrolytic conditions to enable efficient and scalable CO_2 reduction for industrial applications. However, maintaining structural stability during prolonged electrolysis (1000 h) remains challenging, as these defects can degrade under the reaction conditions.

Oxide-derived Cu-based catalysts have emerged as a promising approach to enhance chloride adsorption and enable efficient electrocatalytic CO_2RR under neutral pH conditions, offering multiple advantages. Neutral electrolytes help minimize energy and carbon losses associated with carbonate formation. Still, these systems often suffer from limited multicarbon selectivity and low reaction rates due to the sluggish kinetics of the CO–CO coupling step. Yang et al.[345] published an article demonstrating effective CO_2 reduction utilizing a neutral KCl electrolyte while taking advantage of specific chloride adsorption in order to mediate local CO intermediate coverage for an augmented CO

© 2025 The Author(s). Advanced Functional Materials published by Wiley-VCH GmbH

16163028, 0, Downloaded from https://advanced.onlinelibrary.wiley.com/doi/10.1002/adfm.202502901 by EMBRAPA - Empresa Brasileira de Pesquisa Agropecuaria, Wiley Online Library on [06/06/2025]. See the Terms and Conditions (https://onlinelibrary.wiley.com/terms-and-conditions) on Wiley Online Library for rules of use; OA articles are governed by the applicable Creative Commons License

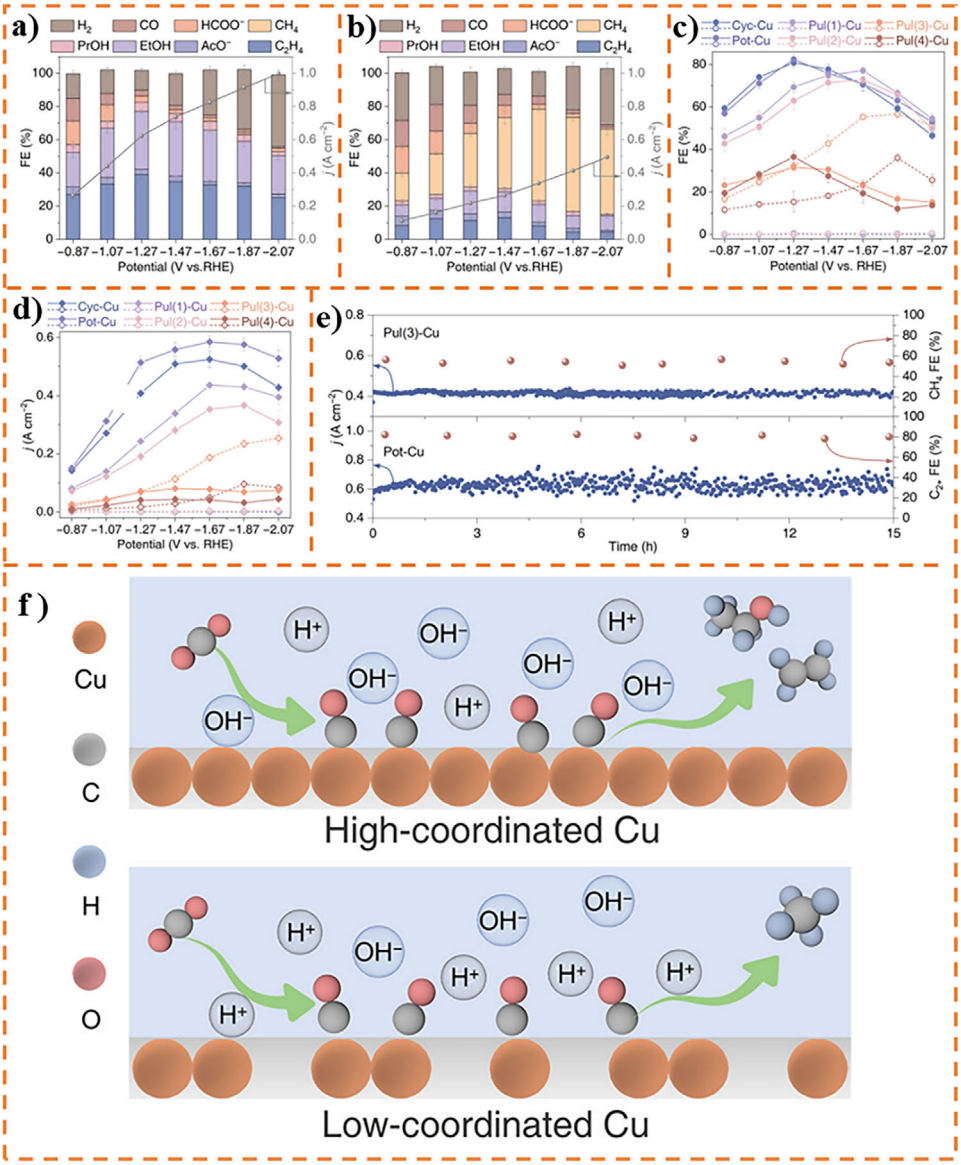

Figure 15. Electrochemical CO_2RR over different Cu electrodes. a,b) Product distribution over Pot-Cu (a) and Pul(3)-Cu (b) at different potentials. c) Plot of FE_{C2+} (solid line) and FE_{CH4} (dash line) vs potential. d) Plot of j_{C2+} (solid line) and j_{CH4} (dash line) vs potential. e) Plot of j vs time over Pul(3)-Cu at −1.87 V vs RHE (top) and Pot-Cu at −1.27 V vs RHE (bottom). f) Schematic representation of the different CO_2 reduction mechanisms of high CN and low CN Cu samples. Reproduced with permission.[343] Copyright 2024, American Chemical Society.

dimerization kinetics. The authors obtained a dual-phase Cu catalyst through the reduction of $CuCl_2.2H_2O$ in ethylene glycol at room temperature, with the addition of tannic acid, in order to promote the chelation of Cu^{2+} ions, halting the complete transition of Cu^{2+} to Cu^0 during the reduction process, resulting in the formation of a Cu-Cu(I) dual phase catalyst. By using this approach, the Cu(I), mainly present in the catalyst as a copper oxide matrix, can facilitate Cl^- adsorption, significantly improving the application of the KCl electrolyte, which was confirmed through ion chromatography to be significantly adsorbed on the amorphous copper oxide present in the catalyst. The improved Cl^- adsorption originated a more energetically favorable CO-CO coupling, significantly augmenting the production of C_{2+} products in a neutral electrolyte, with the most optimal sample achieving a FE_{C2+} of 81% in 3 M KCl, with a superior current density of 400 mA cm^{-2}, significantly higher than the crystalline and amorphous Cu samples, respectively showing an F.E. of 41.4% and 7.5% and current densities values of around 2.2 times lower for the crystalline counterpart, and an insignificant value for the amorphous sample, which yielded mainly CH_4 as the reduction product. Furthermore, it was stable for 45 h at commercially relevant current densities (300 mA cm^{-2}), showcasing its potential for industrial CO_2 electrolysis applications.

Several studies suggest that the enhanced activity of oxide-derived catalysts in CO_2 reduction is closely associated with forming oxygen vacancies during the reaction .[346–348] These oxygen

© 2025 The Author(s). Advanced Functional Materials published by Wiley-VCH GmbH

16163028, 0, Downloaded from https://advanced.onlinelibrary.wiley.com/doi/10.1002/adfm.202502901 by EMBRAPA - Empresa Brasileira de Pesquisa Agropecuaria, Wiley Online Library on [06/06/2025]. See the Terms and Conditions (https://onlinelibrary.wiley.com/terms-and-conditions) on Wiley Online Library for rules of use; OA articles are governed by the applicable Creative Commons License

vacancies would play a critical role in modifying the electronic structure of the catalyst, improving its ability to adsorb and activate key intermediates, such as *CO and *OCCOH. The presence of these defects facilitates electron transfer and lowers the energy barriers for crucial reaction steps, such as C–C coupling, ultimately leading to improved selectivity and efficiency in the production of multicarbon products. Chen R. et al.[349] reported a new strategy of inducing Cu vacancy defects through a fast electrochemical reconstruction process, resulting in an efficient reduction of CO_2 into C_{2+} products with high selectivity (**Figure 16**). Through the reconstruction of $Cu(OH)_2$ nanowires, by in situ electroreduction, the authors were able to obtain Cu nanowires with high concentrations of triple-copper-vacancies, noted as $V_{tri\text{-}Cu}$-rich-Cu. Similarly, through the electroreduction of CuO nanowires, the $V_{tri\text{-}Cu}$-poor-Cu sample was obtained. HAADF-STEM analysis and positron annihilation lifetime were used to confirm and identify the induced defects that resulted from the electrochemical approach, clearly depicting, in the case of the $V_{tri\text{-}Cu}$-rich-Cu catalyst, high quantities of vacancies of three adjacent Cu atoms, while in the case of $V_{tri\text{-}Cu}$-poor-Cu, the vacancy concentration observed was significantly lower. As a result, the $V_{tri\text{-}Cu}$-rich-Cu catalyst obtained a 1000 mA cm^{-2} current density at −0.82 V, almost two times higher than what was observed for the $V_{tri\text{-}Cu}$-poor-Cu. Additionally, the vacancy-rich material also showed a partial current density of 754 mA cm^{-2} for C_{2+} products at −0.85 V with a FE_{C2+} = 80%, while the values observed for the $V_{tri\text{-}Cu}$-poor-Cu sample at the same applied potential were of 274 mA cm^{-2} and a FE_{C2+} = 30%. DFT calculations and ATR-SEIRAS were used to evaluate further the effects of the Cu vacancies in the observed improvement over the $V_{tri\text{-}Cu}$-rich-Cu catalyst. It was found that the presence of the vacancies significantly increased the CO_2 adsorption capabilities of the material, improving the reduction process. The defects were also responsible for contributing to a more excellent stabilization of the adsorbed CO and accelerated *CO dimerization, resulting in superior catalytic capabilities for the $V_{tri\text{-}Cu}$-rich-Cu catalyst.

Single-atom catalysts (SACs) have emerged as highly promising materials for catalyzing electrochemical CO_2 reduction (ECR) owing to their exceptional atomic utilization efficiency. A breakthrough inSAC technology has been the development of CuN_2O_2 active sites supported by carbon dots (Cu-CDs). These catalysts were synthesized through a novel low-temperature partial-carbonization method, preserving a unique coordination environment of Cu with nitrogen and oxygen. The Cu-CDs exhibit extraordinary selectivity, with more than 99% of CO_2RR products being CH_4 over a wide potential range (−1.14 to −1.64 V versus RHE) and a FE of 78% at −1.44 V with a current density of 40 mA cm^{-2}. The catalysts also demonstrate a turnover frequency of 2370 h^{-1} and remarkable stability, retaining 96% of the initial FE after 6 h of continuous operation. DFT calculations attribute these results to suppressed hydrogen evolution reaction (HER) and optimized energy barriers for CH_4 production intermediates.[350] Despite the high selectivity achieved, this work exhibits a low current density and stability, key parameters for a practical application.

Another practical approach to improving the performance of Cu-based catalysts is the formation of single-metal Cu-based alloys, which present tailored electronic structures and modified surface adsorption properties, which facilitate optimized CO_2 activation and stabilization of key reaction intermediates, thereby enhancing selectivity and efficiency for the formation of multicarbon products in electrochemical CO_2 reduction. Kim et al.,[351] reported novel discoveries related to the application of cobalt ions as a trace-level dopant in a Cu-Benzene-1,4-dicarboxylic acid MOF system, which showed promising results towards more efficient CO_2 reduction into C_{2+} compounds, applied with a neutral electrolyte. The prepared Cu-MOFs were doped with concentrations of Co ions from 0.2 to 5.0%. Through XPS and UPS analysis, it was shown that the presence of Co atoms directly affected the *d*-band center of the Co-doped materials, with a gradual shift to the Fermi level, increasing in correlation with Co concentration. This shift in the d-band directly correlates with the binding strength of CO intermediates, making it so that the samples doped with contents of Co of 1% and more had their partial current densities for CO_2RR considerably diminished due to a stronger binding affinity to CO. On the other hand, the 0.2% doped sample showed highly enhanced current densities for CO_2 reduction since the low atomic contents of Co dopants were not sufficient enough to affect the *d*-band center of the catalyst. Additionally, the authors showed, through DFT calculations, that active Cu sites near CO-poisoned Co sites can further hasten the conversion of CO_2 to CO, enhancing the coverage of adsorbed intermediates that are required for the formation of C_{2+} products. The electrode with 0.2% doped was able to achieve a high yield of C_2H_4 of 15.6% at −1.07 V vs RHE, with a current density of 282 mA cm^{-2}.

Zheng et al. also synthesized a single-atom Pb-alloyed Cu catalyst using the sol-gel approach with remarkable performance for CO_2 reduction to formate ($HCOO^-$). A PbCu catalyst achieved near-exclusive conversion of CO_2 to $HCOO^-$ with Faradaic efficiencies exceeding 96% and high partial current densities of ≈1000 mA cm^{-2} at −1.0 V vs RHE (**Figure 17**). The catalyst also maintained a Faradaic efficiency above 90% across a broad potential range (−0.7 V to −1.0 V vs RHE). The PbCu catalyst exhibited exceptional stability, with continuous operation at a partial current density of −500 mA cm^{-2} maintaining an average Faradaic efficiency of 90% over 20 hours in a flow reactor. Additionally, in a system designed for the direct production of pure formic acid using a solid electrolyte, the catalyst sustained operation for 180 h at −3.45 V, producing a total of approximately 8 liters of a 0.1 M HCOOH solution while maintaining selectivity above 85%. The enhanced activity and selectivity of PbCu arise from the suppression of competitive reaction pathways, such as the HER and C–C coupling. In situ spectroscopic studies revealed that the Pb atoms modify the electronic structure of adjacent Cu sites, favoring the adsorption and stabilization of HCOO* intermediates over COOH*. This selective pathway minimizes side reactions, allowing the production of high-purity formic acid solutions. Furthermore, theoretical calculations support these experimental findings, highlighting the reduced energy barriers for the HCOO* pathway on PbCu compared to pure Cu.[352]

Bimetallic catalysts have gained significant attention for the electrochemical reduction of CO_2 due to their unique ability to combine the properties of two metals, often resulting in synergistic effects that enhance catalytic performance. Jiang et al.[353] reported the application of tin and copper oxide nanotubes that achieved a highly selective CO_2 electroreduction to formate by the modulation of the oxidation state of the catalyst. The catalysts

© 2025 The Author(s). Advanced Functional Materials published by Wiley-VCH GmbH

16163028, 0, Downloaded from https://advanced.onlinelibrary.wiley.com/doi/10.1002/adfm.202502901 by EMBRAPA - Empresa Brasileira de Pesquisa Agropecuaria, Wiley Online Library on [06/06/2025]. See the Terms and Conditions (https://onlinelibrary.wiley.com/terms-and-conditions) on Wiley Online Library for rules of use; OA articles are governed by the applicable Creative Commons License

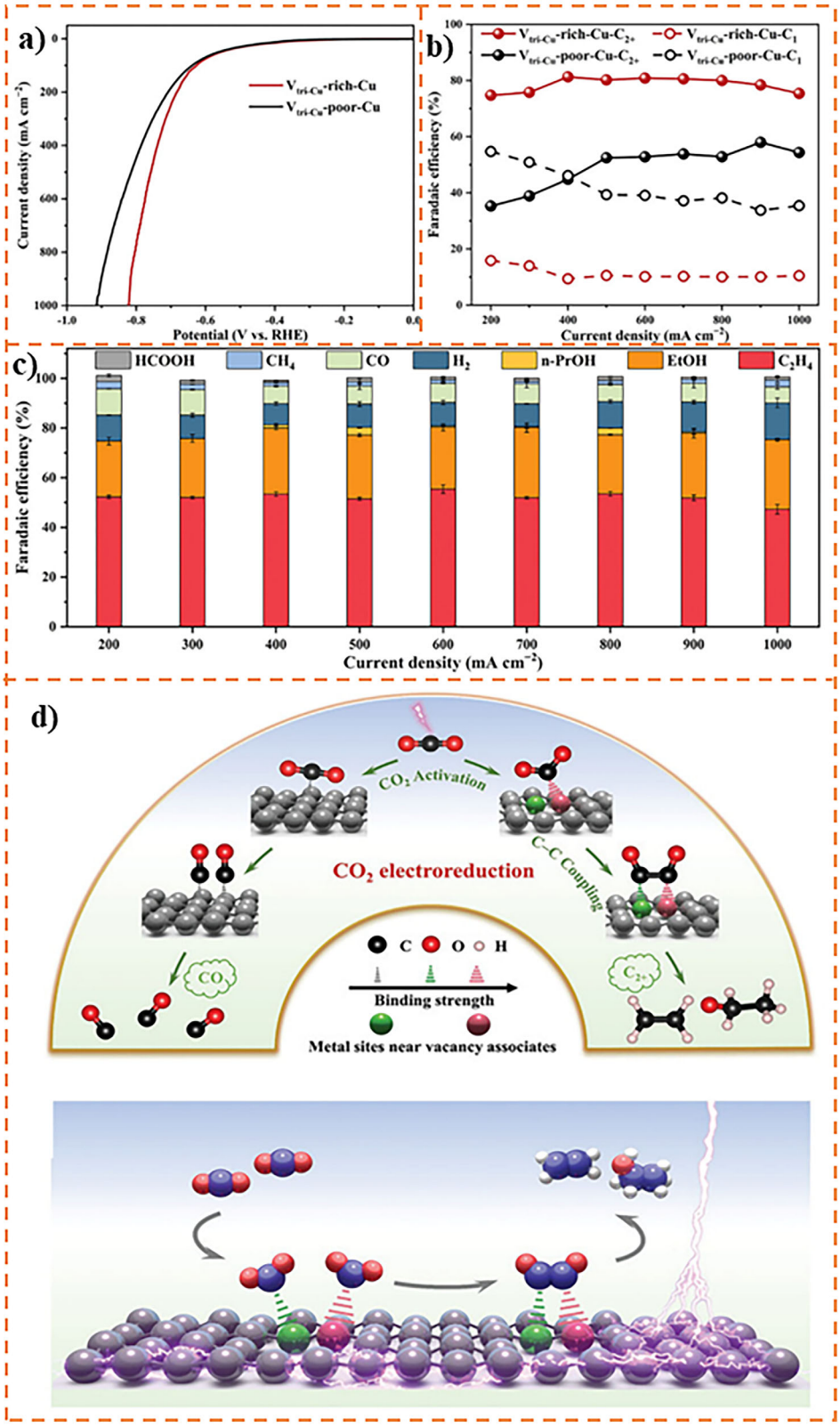

Figure 16. CO_2 electrochemical reduction performance in flow cells. a) Linear sweep voltammetry curves and b) Faradaic efficiencies for C_{2+} and C_1 products of the $V_{tri\text{-}Cu}$-rich-Cu and the $V_{tri\text{-}Cu}$-poor-Cu. c) Product distributions using the $V_{tri\text{-}Cu}$-rich-Cu catalysts at various current densities. Mechanistic illustration of the main catalytic pathway observed on the vacancy-rich Cu catalyst, resulting in higher C_{2+} product obtention (Right path) and the usual pathway of vacancy-poor Cu catalyst, with a prevalence of C_1 products (Left path). Reproduced with permission.[349] Copyright 2020, John Wiley and Sons.

© 2025 The Author(s). Advanced Functional Materials published by Wiley-VCH GmbH

16163028, 0, Downloaded from https://advanced.onlinelibrary.wiley.com/doi/10.1002/adfm.202502901 by EMBRAPA - Empresa Brasileira de Pesquisa Agropecuaria, Wiley Online Library on [06/06/2025]. See the Terms and Conditions (https://onlinelibrary.wiley.com/terms-and-conditions) on Wiley Online Library for rules of use; OA articles are governed by the applicable Creative Commons License

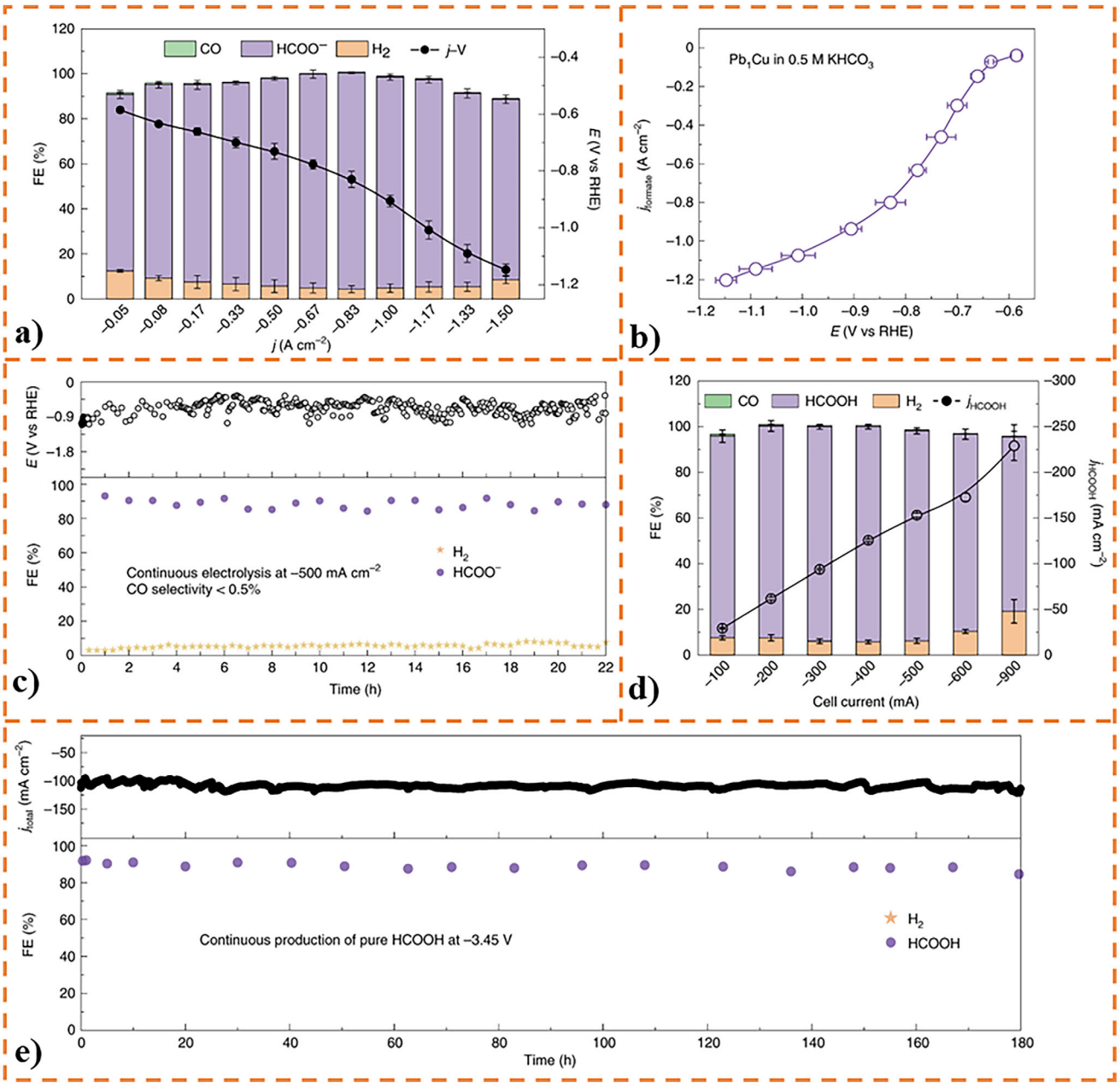

Figure 17. a) FEs of all CO_2RR products at different current densities and the corresponding j–V curve of Pb_1Cu SAAs. b) Variation in the formate partial current density against applied potential over Pb_1Cu SAAs. c) Stability test at $-500\,mA\,cm^{-2}$ current density in a flow cell for over 20 h, indicating an average formate FE of about 90%, estimated by NMR analysis. d,e) Direct production of pure liquid fuel over Pb_1Cu SAAs using a CO_2 reduction device with a solid electrolyte. Reproduced with permission.[352] Copyright 2021, Springer Nature.

were obtained through electrospinning and thermal oxidation of the Sn, Cu, and PVP precursors, with varying ratios of Sn and Cu, that when annealed at 400 °C resulted in a composite nanotube structure of a SnCu-Carbon nanotubes, denoted as SnCu-CNS. FE-SEM and HR-TEM techniques confirmed that the obtained materials possessed a 1D hollow nanotube structure, which could allow for more exposed active sites that can greatly accelerate electron transfers in order to improve the formate selectivity in CO_2 reduction. The obtained XPS spectra confirmed the additional oxidation states contained in the catalyst, with the SnCu-CNS possessing split Sn peaks, related to the presence of Sn^{d+} with higher binding energies than that of Sn^{4+}, and also a greater ratio of Cu^{2+}/Cu^{+}. Compared to the individual tin or copper oxides, the obtained SnCu-CNS showed greater selectivity toward the production of formate from the CO_2 reduction process, with the highest $FE_{formate}$ obtained among the tested catalysts of 95.1% at −0.9 V, with diminished CO and H_2 production. Comparatively, the obtained Sn and Cu oxides obtained $FE_{formate}$ values of 70.8% and 54.4% at the same applied potential. In an electrochemical flow cell, SnCu-CNS can further deliver partial current densities

© 2025 The Author(s). Advanced Functional Materials published by Wiley-VCH GmbH

16163028, 0, Downloaded from https://advanced.onlinelibrary.wiley.com/doi/10.1002/adfm.202502901 by EMBRAPA - Empresa Brasileira de Pesquisa Agropecuaria, Wiley Online Library on [06/06/2025]. See the Terms and Conditions (https://onlinelibrary.wiley.com/terms-and-conditions) on Wiley Online Library for rules of use; OA articles are governed by the applicable Creative Commons License

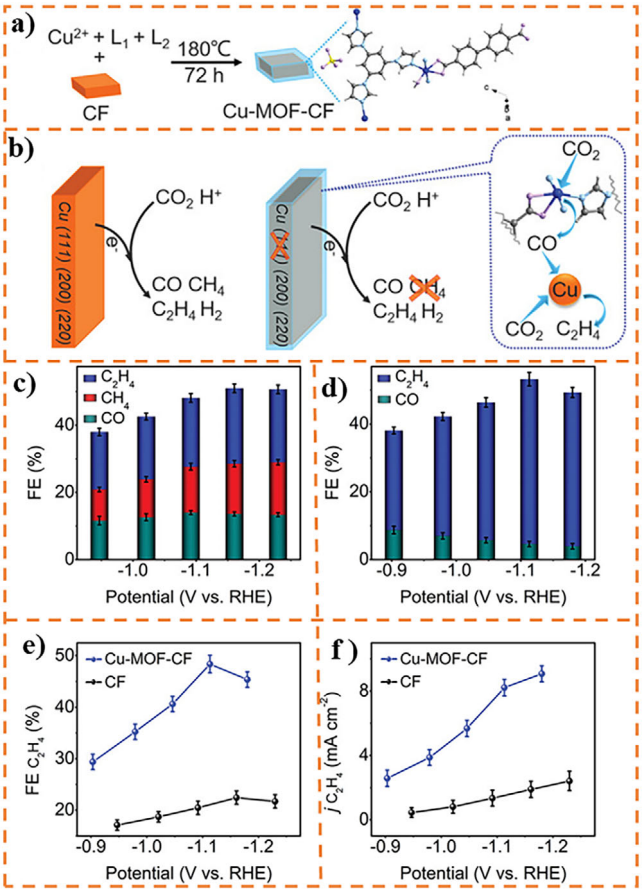

Figure 18. Schematic illustration of a) the preparation of Cu–MOF–CF and b) the main products of electrochemical CO_2RR catalyzed by CF (left) and tandem catalysis at Cu–MOF–CF (right) with the locally abundant CO provided by Cu–MOF for the C_2H_4 formation on CF (color scheme: Cu element, blue; N, cyan; O, pink; C, gray; S, yellow; H, light gray). The FE of CO, CH_4, and C_2H_4 catalyzed by c) CF, d) Cu–MOF–CF for CO_2RR. d) The FE and e) partial current densities of C_2H_4 catalyzed by CF and Cu–MOF–CF for CO_2RR. Reproduced with permission.[355] Copyright 2024, American Chemical Society.

exceeding 200 mA cm^{-2} and over 90% faradaic efficiencies for the formate.

Tandem catalysis also represents a promising and efficient strategy to overcome the challenges associated with CO_2 reduction. By combining distinct active sites tailored for specific reaction pathways—such as CO_2 activation, intermediate stabilization, and product formation-tandem catalysts can facilitate the production of complex hydrocarbons and oxygenates that are otherwise challenging to achieve.[354] In this sense, Yan and co-authors[355] reported the synthesis of a tandem catalyst, comprised of a combination of Cu foil (CF) with a single-site Cu^{2+} MOFwith an enhanced chemical environment allowing for a better selectivity for C_2H_4. The catalyst was obtained through an in situ hydrothermal growth of the $[Cu_2(L_1)_2(L_2)_2(H_2O)_2]$ MOF, where L_1 = 1,3,5-tris(1-imidazolyl)benzene and L_2 = 4,4′-biphenyldicarboxylate, on top different commercial CFs (**Figure 18a**). Structural analysis through PXRD showed an almost complete disappearance of the Cu(111) facet caused by the addition of the Cu-MOF, while at the same time, enhancing the Cu(200) facets. This modification in itself was responsible for a significant suppression of the production of CH_4 during CO_2 reduction, giving rise to the prevalence of C_2H_4 produced. Because of this the Cu-MOF-CF combined catalyst showed increased C_2H_4 selectivity, being the main product obtained throughout the electrochemical experiments, with a FE_{C2H4} of 48.6%, at −1.11 V, more than double that of single CF, with a FE_{C2H4} of 22.4%, at −1.16 V. Additionally, no CH_4 was obtained by the Cu-MOF-CF catalyst during the experiments (Figure 18b–f). Additionally, DFT calculations showed that the CO formation mainly happens through Cu-MOF over CF, due to a lower calculated free energy of the first electron transfer. Cu-MOF also showed a more favorable desorption energy of CO, indicating that the CO intermediates could be easily desorbed after the first electron transfer, allowing for an improved migration of CO to the CF, where the C—C coupling process could happen more favorably.

Chen et al.[356] reported the obtention of novel copper metal-organic polyhedrons (MOPs), with hastened C—C coupling kinetics, and with high selectivity towards C_2H_4 production. The authors have successfully obtained two different terpyridine and carboxyl-based copper metal-organic cages, named respectively Cu(I) and Cu(II). Structurally, the two cages differed in terms of connectivity and the general availability of Cu sites, with Cu(I) being coordinated to six nitrogen atoms, and having only one Cu site, while Cu(II) was bonded to oxygen atoms along an axis containing two available Cu sites. Moreover, structural characterizations revealed that Cu(II) also possessed, along the whole cuboctahedral structure, internal cavities with sufficient diameters to facilitate the adsorption of CO_2 molecules, showing great potential in stabilizing the adsorbed OCCO intermediates. These structural advantages, along with the fact that Cu active sites were present both internally and externally, lead to a lower energy barrier required to induce the formation of *OCCO intermediates, where DFT calculations showed that CO adsorption and further dimerization caused an increase in the *d*-band center of the double Cu sites, leading to an electron transfer from Cu to *CO, further promoting C–C coupling reactions. With this, the Cu(II) catalyst substantially outperformed both the obtained Cu(I) and Cu nanoparticles throughout all the evaluated potentials, achieving a FE_{C2H4} of 51% with a current density and turnover frequency of 469.4 mA.cm^{-2} and 520 h^{-1} respectively, while also being able to efficiently suppress the H_2 evolution process, while also generating CO, CH_4, ethanol, acetate, and formate in the process.

Table 2 compilates the electrochemical conditions applied for the above-mentioned publications, showcasing the type of electrochemical cell used, the electrolyte, and the main result obtained. Despite notable advancements, several challenges still need to be addressed. State-of-the-art systems frequently struggle to maintain high selectivity and activity relevant to industrial applications at current densities. Achieving partial current densities for C_{2+} products exceeding 500 mA cm^{-2} with sustained FEs above 80% remains a critical target. Furthermore, the long-term operational stability of Cu-based catalysts, particularly those with high-index facets or engineered oxidation states, is hindered by structural and compositional degradation.[357] Future research should emphasize the rational design of Cu-based catalysts that balance high activity, selectivity, and durability. Key strategies include stabilizing high-performance facets, optimizing alloy

© 2025 The Author(s). Advanced Functional Materials published by Wiley-VCH GmbH

16163028, 0, Downloaded from https://advanced.onlinelibrary.wiley.com/doi/10.1002/adfm.202502901 by EMBRAPA - Empresa Brasileira de Pesquisa Agropecuaria, Wiley Online Library on [06/06/2025]. See the Terms and Conditions (https://onlinelibrary.wiley.com/terms-and-conditions) on Wiley Online Library for rules of use; OA articles are governed by the applicable Creative Commons License

Table 2. Performance of state-of-the-art Cu-based electrocatalysts for the CO_2RR to hydrocarbons.

Catalyst	FE (%)	Product	Partial current density [mA cm^{-2}]	Electrochemical cell	Refs.
Metallic Cu(100)-rich films	86.6	C_{2+} products;	150	Membrane electrode assembly	[342]
CuO nanoplate	84.5	C_{2+} products	200	Flow cell	[344]
Co-doped Cu_2BDC_2 MOF	45	C_2H_4	282	Flow cell	[351]
Pot-Cu	82.5	C_{2+} products;	514.3	Flow cell	[343]
Cu-CuI	81	C_{2+} products;	400	Flow cell	[345]
Cu-CuI	71	C_{2+} products	591	Flow cell	[358]
Carboxyl-based Cu-MOP	51	C_2H_4	469.4	Flow cell	[356]
Single-Site Cu^{2+} MOF	48.6	C_2H_4	10	H-cell	[355]
$V_{tri\text{-}Cu}$-rich-Cu	80	C_{2+} products	754	Flow cell	[349]
SnCu-CNS	95.1	$HCOO^-$	230	Flow cell	[353]
Pb-alloyed Cu	90	HCOO-	500	Flow cell	[352]

compositions, and engineering surface properties. Achieving these goals will require advanced in situ characterization techniques, such as operand spectroscopy and high-resolution microscopy, combined with density functional theory calculations to establish design principles that guide the development of next-generation catalysts capable of supporting large-scale CO_2 utilization.

The photoelectrocatalysis technique represents a synergistic combination between the photoexcitation of semiconductors and electric conduction, integrating the applicability aspects of photocatalysis with enhanced charge separation kinetics. In this approach, the photocatalysts are usually applied as photoelectrodes in an electrochemical cell. Upon sufficient irradiation of the catalyst, the photoelectrocatalytic process is initiated, with the applied material fostering the formation of electron-hole pairs. The application of an external electric field then promotes the directed migration of photogenerated charges towards the electrode surface, effectively suppressing charge recombination, by spatially separating the photogenerated charges. If the photogenerated electrons and holes are not quickly separated, they can recombine, releasing energy as heat or light and thus becoming unavailable for the desired reactions. Photoelectrocatalytic systems facilitate carrier separation through overpotential adjustment and enable rapid multi-electron and proton transfer, enhancing catalytic reaction efficiency.[359]

This approach is particularly advantageous in CO_2 reduction, where multiple electron and proton transfers are required to form complex products. In CO_2 photoelectroreduction, the applied external bias plays a crucial role in overcoming the thermodynamic barrier for CO_2 reduction, effectively lowering the overpotential required for the reaction to proceed compared to photocatalytic processes. Furthermore, the applied bias can significantly influence the charge transfer kinetics at the electrode-electrolyte interface and also play a role in determining the selectivity of the reaction towards different products. By controlling the magnitude of the applied voltage, the energy levels of the catalyst surface and the adsorbed reaction intermediates can be altered, which in turn can favor specific reaction pathways over others, leading to the preferential formation of specific CO_2 reduction products.[360]

As expected from its catalytical activity in photo and electroreduction, Cu-based catalysts are also promising materials for the photoelectroreduction of CO_2. Brito et al. investigated the photoelectrochemical reduction of CO_2 using a Cu/Cu_2O electrodes.[361] The study revealed the formation of several products, including methanol, ethanol, formaldehyde, acetaldehyde, and acetone, under UV-visible radiation over a 3-hour period at 0.2 V (versus Ag/AgCl). Notably, the process led to removing 80% of the initial CO_2 in a 250 mL one-compartment cell with a 1 cm^2 cathode. The authors proposed that the reduction involves photogenerated electrons in the p-type Cu_2O semiconductor, with subsequent reactions involving radical species influencing the distribution of the resulting products. Furthermore, the research identified pH as a key factor affecting the selectivity of methanol formation.

Zhou et al. synthesized Cu-modified Bi_2Se_3 catalysts with selenium-deficient sites to enhance the photoelectrochemical reduction of CO_2 to formate.[362] The introduction of Cu improved the catalytic performance, achieving a maximum formate Faraday efficiency of 65% at a low overpotential of −0,5 V vs RHE with the catalyst containing 8% Cu. The authors attributed this enhancement to Cu's role in improving CO_2 adsorption, increasing the catalyst's electrochemical active surface area, and modifying the electronic structure of Bi_2Se_3. Additionally, the study demonstrated a high formate yield of almost 140 μmol h^{-1} cm^{-2} in a photoelectrocatalysis system using solar light.

In another work, Zhang et al. introduced a hydrophilic-hydrophobic $Cu-SnO_2$/ZIF-8 composite catalyst.[363] The material enabled the direct use of gas-phase CO_2, enhancing CO_2 activation and suppressing hydrogen evolution, achieving almost 69% Faraday efficiency for formic acid at a low overpotential of ≈364 mV, with a maximum current density reaching 12.8 mA cm^{-2}. The authors suggest that the ZIF-8 structure facilitates electron transfer and $Cu-SnO_2$ dispersion, providing more active sites. At the same time, the composite's unique hydrophilic-hydrophobic nature and small band gap contribute to its high performance.

In a study by Wang et al., a hybrid catalyst was designed featuring active Cu-N sites on a CuO photocathode for the photoelectrochemical reduction of CO_2.[364] The photocathode demonstrated enhanced performance, reaching a photocurrent density of −1.0 mA cm^{-2} at 0.2 V vs RHE, showing a 15.2% Faradaic efficiency for C_2 product formation in aqueous solution. Density functional theory calculations indicated that the Cu-N pair's

© 2025 The Author(s). Advanced Functional Materials published by Wiley-VCH GmbH

16163028, 0, Downloaded from https://advanced.onlinelibrary.wiley.com/doi/10.1002/adfm.202502901 by EMBRAPA - Empresa Brasileira de Pesquisa Agropecuaria, Wiley Online Library on [06/06/2025]. See the Terms and Conditions (https://onlinelibrary.wiley.com/terms-and-conditions) on Wiley Online Library for rules of use; OA articles are governed by the applicable Creative Commons License

unique arrangement, with an asymmetric d-p orbital on the CuO, facilitates C-C coupling by altering the binding energy of intermediate species. The improvement in C-C coupling was also observed by Wang et al., with the designed Cu@porphyrin-COFs nanorods catalyst.[365] This novel material yielded various C_1-C_3 products, including methanol, ethanol, ethane-1,1-diol, and acetone.

3.2. Hydrogen Evolution Reaction

The urgent need to reduce dependence on fossil fuels has driven significant advancements in developing technologies for producing sustainable and clean energy. Among these, photo or electrocatalytic H_2evolution stands out as a promising approach. In an ideal system, H_2 and O_2 are generated through catalytic reduction and oxidation, irrespective of whether the energy input is photonic or electrical. The overall thermodynamic potential required for water splitting into H_2 and O_2 is 1.23 V. This fundamental value establishes an energy threshold for photo- and electrocatalytic processes.

This 1.23 V requirement in photocatalysis translates to the minimum band gap energy a semiconductor must possess to enable water splitting. Furthermore, the semiconductor's conduction and valence band positions must facilitate photogenerated electron and hole transfers with sufficient energy to drive water reduction and oxidation. Similarly, the applied potential must surpass 1.23 V in electrocatalysis to provide the reaction's necessary thermodynamic driving force. The overpotential, which is the excess potential above the thermodynamic minimum, is a key parameter affecting the reaction kinetics in both photo- and electrocatalysis.

Developing catalysts that meet these criteria is critical for achieving efficient water splitting. Cu-based catalysts exhibit tunable electronic properties, including a wide range of bandgap values (from 1.2 to over 3.0 eV), making them versatile for light absorption in photocatalysis and for optimizing electrochemical potentials in electrocatalysis. Additionally, the conduction band edge of many Cu-based catalysts and their electrochemical potentials often align favorably with the H_2 evolution potential, which is advantageous for promoting H_2 production reactions in both photo- and electrochemical systems. The rational design of materials with optimized band structures or electrochemical potentials is crucial for enhanced performance in both domains.

Many standalone Cu-based catalysts have shown activity for H_2 production, including Cu_2O,[366, 367] CuO,[368] CuSe,[369] $CuCrO_2$,[370] $CuAlO_2$,[371] $CuFeO_2$,[372] $CuInS_2$,[185, 373] Cu_2ZnSnS_4, $Cu_{3-x}SnS_4$,[374] $CsCuCl_3$,[375] $Cs_3Bi_2I_9$,[376] $Cs_3Bi_{2x}Sb_{2-2x}I_9$ ($x \approx 0.3$)„[377] Cu-I-bpy (bpy = 4,4′-bipyridine)„[378] MOF-199,[379] etc. However, despite their promising attributes, pure Cu-based catalysts often encounter significant challenges in both photo- and electrocatalysis, including rapid electron-hole recombination or surface site deactivation and, in the case of photocatalysis, photocorrosion. This is particularly evident in materials like Cu_2O and CuO, where the reduction potentials, whether accessed through photon excitation or applied voltage, fall within their respective energy gaps or operational potential windows, leading to instability. Thus, the development of modified photo and electrocatalysts has garnered significant attention in recent scientific literature.

3.2.1. Electrocatalytic H_2 Evolution

At the HER electrode, hydrogen is generated through bubble release, proton movement, and electron transfer. These elements are crucial considerations in the electrode's design and development.[380] Doping has been identified as an effective approach for advancing electrode development. For instance, Han et al. developed a copper and palladium co-doped molybdenum disulfide (Cu−Pd−MoS_2) catalyst for the HER. The authors found that doping MoS_2 with Cu effectively improved its poor electrical conductivity, a significant limitation for its practical application. Simultaneously, Pd doping enhanced the phase transition in MoS_2 to the more catalytically favorable 1T phase. This combination of Cu and Pd doping created a synergistic effect that increased the number of active sites for the HER and modulated the electronic structure of MoS_2 to enhance its intrinsic catalytic activity. As a result, the co-doped Cu−Pd−MoS_2 catalyst demonstrated superior HER performance in acidic media, exhibiting a low overpotential of 93 mV at a current density of 10 mA cm^{-2}, a small Tafel slope of 77 mV dec^{-1}, and excellent stability of 50 h.

Heterojunctions are also a widely adopted strategy to improve the efficiency of Cu-based catalysts in water splitting. Wang et al. synthesized Cu_2S/MoS_2 heterojunction nanorod arrays on copper foam using a facile hydrothermal method.[381] The authors achieved nitrogen doping in situ and characterized the heterojunction interfacial texture and defect-rich nanoarray configuration using HRTEM, SEM, XPS, and EDX. The resulting heterojunction structure demonstrated enhanced HER electrocatalytic activity, with a low charge transfer resistance of 5.4 Ω at −0.2 V vs RHE, a high electrochemical double layer capacitance of about 49 mF cm^{-2}, a low overpotential of 91 mV at 10 mA cm^{-2}, and a small Tafel slope of 41 mVdec^{-1}.

Yoon et al. reported on the synthesis and HER electrocatalytic activity of unique cactus-like hollow nanoplates composed of $Cu_{2-x}S$@Ru.[382] The authors detailed a synthesis involving the initial formation of "Ru islands" on copper sulfide nanoparticles which led to the formation of a hollow nanostructure with thin Ru pillars. The resulting catalysts displayed excellent HER performance in alkaline media, characterized by a low overpotential of 82 mV at a current density of −10 mA cm^{-2} and a small Tafel slope of 48 mV dec^{-1}. This enhanced activity was attributed to the heterojunctions formed between metallic Ru, Ru oxide, and $Cu_{2-x}S$ phases, facilitating water dissociation and hydrogen adsorption.

As demonstrated in Yoon et al. study, transition metal chalcogenides have proven to be effective electrocatalysts., owing to their diverse electronic configurations and adaptable morphology. Recently, Cu-based chalcogenides such as Cu_2S, Cu_2Se, and Cu_2Te were reported as effective electrocatalysts for HER study. For example, Bae et al. reported the preparation of a catalyst composed of composite chalcogenide materials with layered Cu-based heterojunctions and investigated their charge transport properties in HER. In this method, when MoS_2 is deposited on transition metals like Cu, sulfidation reactions occur, leading to the formation of bulk layered heterojunctions (BLHJs) of Cu-Mo-S, containing MoS_2 flakes uniformly dispersed in the Cu_2S matrix. The resulting BLHJs showed efficient HER performance, achieving ≈10 mA cm^{-2} at a potential of −0.1 V vs a RHE, with a Tafel slope of 30–40 mV dec^{-1}.

© 2025 The Author(s). Advanced Functional Materials published by Wiley-VCH GmbH

16163028, 0, Downloaded from https://advanced.onlinelibrary.wiley.com/doi/10.1002/adfm.202502901 by EMBRAPA - Empresa Brasileira de Pesquisa Agropecuaria, Wiley Online Library on [06/06/2025]. See the Terms and Conditions (https://onlinelibrary.wiley.com/terms-and-conditions) on Wiley Online Library for rules of use; OA articles are governed by the applicable Creative Commons License

Fan et al. presented a method for the in situ growth of single-crystalline $\gamma-Cu_2S$ nanoplates on copper foam and investigated its application as an electrocatalyst for HER at neutral pH. The authors demonstrated that Co(II) acetate assisted in inhibiting the formation of Cu_2O), directing the formation of the $\gamma-Cu_2S$ crystal phase, and controlling the morphology of the resulting $\gamma-Cu_2S$ nanoplates. The resulting $\gamma-Cu_2S$/Cu foam material, used as an integrated 3D electrode, exhibited efficient HER activity, achieving a current density of 10 mA cm^{-2} at a small overpotential of 190 mV, demonstrating a 100% Faradaic yield and maintaining its activity for over 10 h.

It is interesting to notice that the pH conditions during electrocatalytic H_2 evolution is a crucial factor. Bhat and Nagaraja synthesized Cu_2S micro-hexagons via a hydrothermal method and evaluated their electrocatalytic activity for the HER in extreme acidic (0.5 M H_2SO_4, pH 0) and basic solutions (1 M KOH, pH 14).[383] The Cu_2S micro-hexagons demonstrated efficient HER performance in both extreme pH conditions, requiring overpotentials of 330 and 312 mV to achieve a current density of 10 mA cm^{-2} in basic and acidic solutions, respectively. The catalyst also exhibited good stability over 24 h.

3.2.2. Photocatalytic H_2 Evolution

In photocatalysis, sacrificial agents such as methanol, ascorbic acid, Na_2SO_3/Na_2S, $Na_2S_2O_3$, oxalic acid, and TEOA are commonly employed to consume photogenerated holes in most applications. Strategies such as coating Cu-based catalysts with protective layers to enhance stability or coupling them with other suitable semiconductors to form heterojunctions have been developed to improve their efficiency and durability in H_2 evolution reactions.

The low activity and durability of pure Cu-based catalysts remain significant barriers to further developing this technique. Passivation engineering provides a practical solution by offering additional protection to photocatalysts and facilitating the smooth transfer of photogenerated carriers. A passivation layer can be integrated during fabrication or applied as a coating in a separate step. For example, Daskalakis et al.[384] employed a sulfidation process to passivate surface sulfur defects in Cu-doped ZnS, forming Cu_2S/ZnS. This approach enhanced charge transfer, achieving an H_2 evolution rate of 1 mmol g^{-1} h^{-1}. Dey et al. used plasma treatment to create a nanoscale CuO surface layer on Cu_2O, which minimized interfacial defects. This significantly improved both the catalytic H_2 evolution performance and the stability of the Cu_2O photocatalyst. Moreover, nanometer-thick protective layers, such as TiO_2, ZnO, Al_2O_3, and carbon, are commonly applied to enhance the photostability of Cu-based photocatalysts. Li et al.[385] prepared a Cu_2O@C composite through photo-induced in situ synthesis, where the carbon shell prevented photo-corrosion of Cu_2O. The Cu_2O@C nanocomposite demonstrated an H_2 evolution rate of almost 1.3 mmol g^{-1} h^{-1} under visible light and maintained excellent stability without deactivation after five cycles. Similarly, rGO-enwrapped Cu−Cu_2O photocatalysts showed a remarkable H_2 evolution rate of 51.6 mmol g^{-1} h^{-1} with stable performance.[386] Ren et al.[387] encapsulated Cu^0 nanoparticles with ultrathin graphene using MOFs as precursors. This design resulted in exceptional stability, and the optimized Cu@C/$SrTiO_3$ achieved an H_2 evolution rate of 255.3 μmol g^{-1} h^{-1} with an apparent quantum efficiency of 3.8% at 420 nm.

TiO_2 is another widely used protective layer for Cu-based photocatalysts, particularly Cu_2O, to improve stability and H_2 evolution efficiency.[388–390] Among Cu-based compounds, $CuBi_2O_4$ is a promising photocatalyst with a narrow bandgap (≈1.8 eV) suitable for H_2 evolution.[391, 392] However, like Cu_2O, it faces challenges with self-reduction during photocatalytic reactions, likely caused by the trapping of photoelectrons in the Cu 3D band. Protective layers, such as TiO_2, have also effectively addressed this issue for $CuBi_2O_4$-based systems.[155, 393]

Heterojunctions are effective in enhancing light absorption and promoting the separation of photoinduced charge carriers. Beyond serving as a protective layer, TiO_2 is one of the most popular materials to couple with Cu-based photocatalysts for efficient H_2 evolution. Examples include Cu_2O/TiO_2,[394, 395] CuO/TiO_2,[396, 397] Cu_2S/TiO_2,[398] CuS/TiO_2,[399, 400] and $CuInS_2/TiO_2$.[401] Notably, coupling CuO or Cu_2O with TiO_2 enables H_2 production in pure water, achieving yields of 265 μmol h^{-1} and 290 μmol h^{-1} for CuO/TiO_2 and Cu_2O/TiO_2, respectively.[394] The formation of a Z-scheme heterojunction between CuS and TiO_2 preserves the strong reduction capability of CuS and the oxidation capability of TiO_2.[400] This configuration was employed to construct a bifunctional photocatalytic system for simultaneous H_2 evolution and selective oxidation of benzylamine to N-benzylidene benzylamine. Beyond TiO_2, many other semiconductors have been successfully coupled with Cu-based photocatalysts to form efficient heterojunctions. Examples include Cu_2O/g-C_3N_4,[402] CuO/g-C_3N_4,[403] Cu_2O/ZnO,[404, 405] Cu_2O/WO_3,[406] CuO/SnO_2,[407] Cu_2S/CdS,[408] $Cu_2S/MoS_2/TiO_2$,[409] CuS/ZnS,[410] CuS/CdS,[411, 412] CuS/g-C_3N_4/CdS,[413] $CuFeO_2/SnO_2$,[414] $CuInS_2/ZnIn_2S_4$,[415] $CuInS_2/Mo_2S_3$,[416] and Cu_2O/2D PyTTA-TPA COFs.[417] The list continues to grow as numerous semiconductors demonstrate compatibility and effectiveness in forming heterojunctions with Cu-based photocatalysts. A particularly noteworthy advantage of forming heterojunctions is their ability to enable certain systems to produce H_2 directly from pure water. For example, Cu_2O/WO_3 and CuS/CdS[412] heterojunctions have shown this capability, underscoring the promise of heterojunction engineering in advancing photocatalytic H_2 production.

Metallic Cu has emerged as a promising alternative to noble metals as a cocatalyst for photocatalytic H_2 evolution. However, the standalone use of Cu nanoparticles is limited due to their inherent instability, including tendencies toward aggregation and oxidation. Cu has been combined with semiconductors or non-semiconductors in photocatalytic systems to address these challenges. This approach enhances the dispersion and stability of Cu nanoparticles while introducing synergistic effects that boost photocatalytic performance.

In semiconductor-based systems, Cu/TiO_2 has been extensively investigated. Photoinduced electrons on TiO_2 are efficiently transferred to metallic Cu. These electrons accumulate on Cu, reducing protons or water to produce H_2. For instance, Xiao et al.[418] employed a microwave-assisted hydrothermal strategy to decorate Cu nanowires with TiO_2 nanorods. This hybrid system demonstrated exceptional photocatalytic activity,

© 2025 The Author(s). Advanced Functional Materials published by Wiley-VCH GmbH

16163028, 0, Downloaded from https://advanced.onlinelibrary.wiley.com/doi/10.1002/adfm.202502901 by EMBRAPA - Empresa Brasileira de Pesquisa Agropecuaria, Wiley Online Library on [06/06/2025]. See the Terms and Conditions (https://onlinelibrary.wiley.com/terms-and-conditions) on Wiley Online Library for rules of use; OA articles are governed by the applicable Creative Commons License

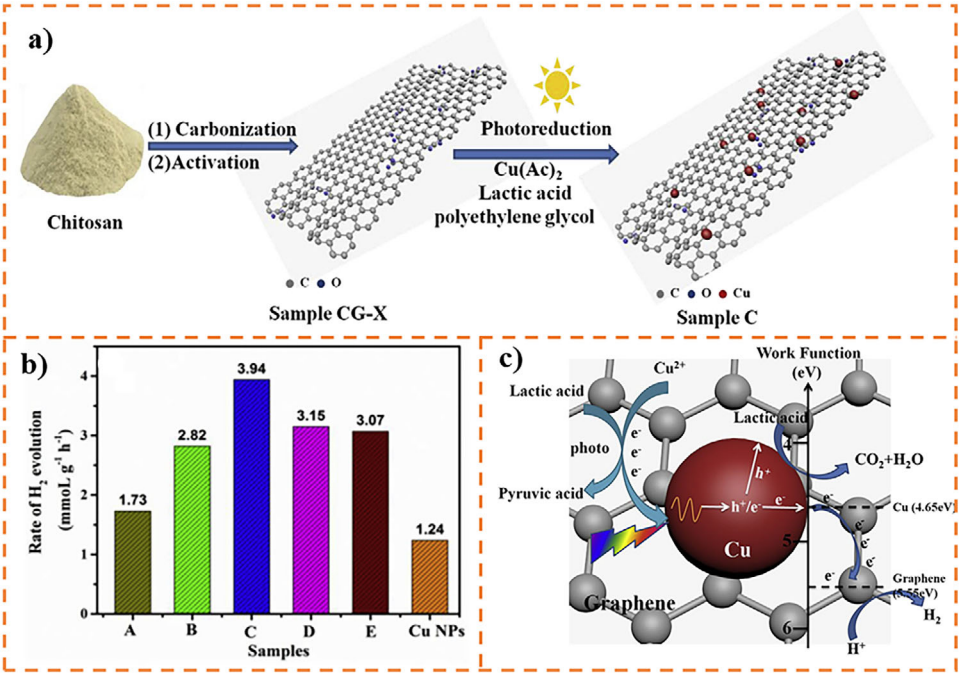

Figure 19. a) Illustration of the preparation procedure for samples, b) Photocatalytic H_2 evolution under solar light, c) Schematic of reaction mechanism over the Cu/graphene system. Reproduced with permission.[420] Copyright 2019, Elsevier.

achieving an H_2 production rate of 5104 μmol h^{-1} g^{-1} and an apparent quantum yield of 17.2%. The enhanced performance was attributed to the favorable geometry of the Cu/TiO_2 system, which provided a large interfacial contact area and facilitated efficient photoelectron transfer from TiO_2 to Cu. Song et al.[419] synthesized one-dimensional Cu/TiO_2 with Cu nanoparticles measuring 3–6 nm in diameter. The Cu nanoparticles exhibited LSPR absorption spanning the visible to near-infrared spectrum. The plasmon-induced photothermal effect significantly enhanced photocatalytic H_2 evolution, yielding 243.6 μmol of H_2 under full-spectrum light, which was double the yield obtained under UV-Vis irradiation. In addition to semiconductors, Cu nanoparticles have been successfully loaded onto various supports, including carbon materials,[101, 420] nitrides,[421–423] polymers,[424] and silica.[425, 426] For example, Huang et al.[420] prepared graphene nanosheets with fewer layers by carbonizing and activating chitosan, followed by the deposition of Cu nanoparticles via in-situ photoreduction (**Figure 19a**). The optimal Cu/graphene photocatalyst achieved an H_2 evolution rate of 3.94 mmol g^{-1} h^{-1}, which was 3.2 times higher than pure Cu nanoparticles (Figure 19b). The graphene support acted as an electron mediator and an acceptor, facilitating the separation of photoinduced electron-hole pairs (Figure 19c).

As previously discussed, Cu-based photocatalysts can undergo photocorrosion under irradiation during reactions. Interestingly, this phenomenon can sometimes enhance photocatalytic performance by generating plasmonic metallic Cu nanoparticles. Xi et al.[427] developed a Cu_2O/TiO_2 heterostructure for H_2 evolution, where metallic Cu particles formed after several hours of irradiation. These Cu particles played a crucial role in boosting H_2 generation by increasing the availability of photoinduced electrons and facilitating the separation of charge carriers. The in-situ reduction of Cu^+ to Cu^0 during photocatalysis was also confirmed by Sinatra et al.[395] Similarly, Esmat et al.[428] observed an in-situ structural transformation of CuO/TiO_2 nanosheets during photocatalytic H_2 evolution in the presence of ammonia-borane. Their findings revealed that CuO nanoparticles transformed into metallic Cu during the reaction. The plasmonic features of the in-situ generated metallic Cu significantly contributed to the photocatalytic activity, highlighting the dynamic role of Cu during photocatalytic processes.

It is worth mentioning that the Cu site plays a pivotal role in optimizing the photocatalytic H_2 evolution performance, particularly in systems featuring Cu SAs and doped Cu. Liu et al.[429] demonstrated that by tuning the electronic states of Cu sites in metal-organic supramolecular assembles from $\{Cu_2(bpybc)(phen)_2(H_2O)Br_{1.22}\}\cdot Br_{2.78}$ to $\{Cu_2(bpybc)(bpy)_2(H_2O)Br_{1.14}\}\cdot Br_{2.86}$ (bpybc = 1,1′-bis(4-carboxy benzyl)-4,4′-bipyridinium, phen = 1,10-phenanthroline, bpy = 2,2′-bipyridine), based on $\pi\cdots\pi$ stacking, the photocatalytic H_2 production rate was remarkably improved from 522 to 3620 μmol g^{-1} h^{-1}. Han et al.[430] constructed a MOF/COF heterostructured photocatalyst, Cu-NH_2-MIL-125/TpPa-2-COF, where Cu ions were immobilized by -NH_2 groups of MOF. The Cu ions alternated between Cu^{2+} and Cu^+ states, acting as active centers. During photocatalysis, photogenerated electrons transferred from the CB of TpPa-2-COF to the CB of Cu-NH_2-MIL-125, reducing Cu^{2+} to Cu^+. The reduced Cu^+ then facilitated the reduction of H^+ to H_2, regenerating Cu^{2+}. This efficient mechanism enabled a remarkable H_2 evolution rate of 9.2 mmol g^{-1} h^{-1}.

In recent years, Cu SAs have gained attention for their exceptional H_2 evolution capabilities. For instance, single-atom Cu was

© 2025 The Author(s). Advanced Functional Materials published by Wiley-VCH GmbH

16163028, 0, Downloaded from https://advanced.onlinelibrary.wiley.com/doi/10.1002/adfm.202502901 by EMBRAPA - Empresa Brasileira de Pesquisa Agropecuaria, Wiley Online Library on [06/06/2025]. See the Terms and Conditions (https://onlinelibrary.wiley.com/terms-and-conditions) on Wiley Online Library for rules of use; OA articles are governed by the applicable Creative Commons License

integrated into C_3N_4 sheet interlayers to create electron-transfer channels between layers.[431] Rapid interlayer charge transfer was realized with the additional help of N vacancy to allow more electrons to the Cu sites via the delocalized π-conjugated network of C_3N_4. This system achieved an H_2 evolution rate of 605.1 μmol g^{-1} h^{-1} without a cocatalyst and 11.2 mmol g^{-1} h^{-1} with a 1 wt% Pt cocatalyst under visible-light irradiation. Stabilizing high concentrations of single-atom Cu without aggregation remains a significant challenge. Zhang et al.[432] addressed this issue by employing a pre-encapsulation strategy, enabling the stabilization of Cu single atoms on TiO_2 at a loading of >1 wt% without aggregation. The Cu single atoms facilitated efficient charge transfer via the Cu^{2+}/Cu^{+} redox process, achieving an impressive H_2 evolution rate of 101.7 mmol g^{-1} h^{-1} under simulated solar irradiation. Fu et al.[433] further investigated the mechanism underlying single-atom photocatalysis using Cu-TiO_2 as a model system. Through ab initio quantum dynamics simulations, they revealed that the exceptional activity of Cu single atoms arises from their quasi-planar coordination structure formed upon H_2O adsorption. This structure enables the Cu atom to capture photoexcited hot electrons and transfer them into a hybridized orbital formed between Cu and H_2O, thereby enhancing photocatalytic performance.

3.3. Oxygen Reduction Reactions

The oxygen reduction reaction (ORR) is a critical process that underpins the performance of several essential clean energy technologies. In devices such as proton-exchange membrane fuel cells, alkaline fuel cells, direct methanol fuel cells, and metal-air batteries, the efficient conversion of oxygen is paramount. Despite its significance, the ORR is hindered by its inherently sluggish reaction kinetics, which involves multiple electron and proton transfer steps and the challenging cleavage of the strong O=O bond, leading to substantial overpotential. This kinetic limitation is a major bottleneck, significantly impacting these devices' overall efficiency, power density, and cost-effectiveness. For instance, in proton-exchange membrane fuel cells, the ORR kinetics are notoriously slow, estimated to be about six orders of magnitude slower than the hydrogen oxidation reaction occurring at the anode.[434–436]

To overcome the kinetic barriers of the ORR, efficient electrocatalysts are crucial. Platinum (Pt) and its alloys, typically supported on carbon (Pt/C), have long been established as state-of-the-art catalysts, exhibiting the highest activity and reasonable stability for ORR, particularly in the demanding acidic environment of proton-exchange membrane fuel cells. Nevertheless, the widespread adoption of Pt-based catalysts is hampered by two major factors: the high cost and the limited natural abundance. The catalyst cost, primarily due to Pt, can account for a substantial portion (40–50%) of the total cost of a proton-exchange membrane fuel cell stack.[434] These limitations have spurred intensive research toward developing alternative ORR catalysts based on earth-abundant, low-cost, and stable materials. In this context, various Cu-based catalysts have been explored for the ORR, including copper oxides, copper sulfides, copper alloys, Cu-SACs anchored on supports like nitrogen-doped carbon (Cu-N-C), and others.

To further understand the role of copper oxides in this reaction, Li et al. explored the structure-dependent electrocatalytic activity of Cu_2O nanocrystals towards the ORR in an alkaline environment.[437] The authors observed that Cu_2O nanocrystals' electrocatalytic activity depends on the exposed crystal facets, with the {100} facet exhibiting higher activity than the {111} facet. Notably, Cu_2O nanocubes with dominant {100} crystal planes demonstrated superior four-electron selectivity (n = ~3.7) and a low H_2O_2 yield of 15% during the ORR process. Furthermore, the Cu_2O nanocrystals retained approximately 91% of their initial current after 10000 seconds and exhibited better methanol tolerance and durability for ORR than commercial Pt/C materials. This facet preference for ORR can be modified depending on the material complexity and structure. For instance, Liu et al. synthesized Cu_2O-based composites with Co_3O_4 for use as non-noble catalysts in ORR and OER.[438] DFT calculations predicted Cu-sites in the Cu_2O-Co_3O_4 (111) structure to be the primary active sites for ORR. The resulting catalyst showed enhanced ORR activity, with a half-wave potential of 0.90 V, and exhibited better methanol tolerance than Pt/C. In another work, Chang et al. synthesized Cu_2O cubes, octahedra, and rhombic dodecahedra, exposing (100), (111), and (110) surfaces, respectively, and incorporated them into carbon nanotubes (CNTs) to study their electrocatalytic activity for ORR.[439] The rhombic dodecahedra/CNTs composite exhibited the highest ORR activity, with a limiting current density of 4.25 mA cm^{-2}, followed by the octahedra/CNTs (3.93 mA cm^{-2}) and the cubes/CNTs (3.67 mA cm^{-2}). Koutecký–Levich plots showed that the Cu_2O polyhedral were highly selective towards the four-electron pathway in the ORR, and DFT calculations indicated that the Cu_2O (110) surface had the weakest O_2 adsorption (-0.09 eV), contributing to its superior ORR activity.

Copper oxide catalysts were also studied in photo-assisted ORR systems. Recently, Li et al. engineered copper oxide with copper vacancies ($CuO_{-0.9\%}V_{Cu}$) to enhance its performance in ORR, specifically for photo-assisted Zn-air batteries.[440] The introduction of these vacancies optimized the chemisorption and activation of OOH intermediates on active Cu atoms. This process leads to a faster reduction rate of O_2. The photocathode attained an improved charge separation yield of 59% and a transfer yield of 70% in ORR reactions. This approach allowed the ZABs to achieve higher discharge voltage and energy efficiency.

Alloying copper with palladium represents a viable approach to decreasing the quantity of noble materials in catalysts. Fouda-Onana et al. investigated Pd-Cu alloys as catalysts for the ORR in acidic media.[441] The study revealed that the electrocatalytic activity of Pd-Cu alloys is enhanced by adding Cu, with the $Pd_{50\%}Cu_{50\%}$ alloy demonstrating the highest activity for the ORR. This enhanced activity was attributed to an optimal d-band property that facilitates the dissociative adsorption of OOH, considered a critical step in the ORR. Furthermore, the study revealed that the ORR on Pd-Cu alloys proceeds through a four-electron transfer mechanism, with a Tafel slope of 60 mV dec^{-1} at low overpotentials, indicating a chemical rate-determining step.

Cu-SACs materials, particularly Cu-N-C SACs, have been reported for ORR, demonstrating significant potential. For example, in 2022, Yang et al. developed a nitrogen-doped porous carbon material containing atomically dispersed Cu and Cu clusters.[442] The resulting catalyst showed excellent ORR

© 2025 The Author(s). Advanced Functional Materials published by Wiley-VCH GmbH

16163028, 0, Downloaded from https://advanced.onlinelibrary.wiley.com/doi/10.1002/adfm.202502901 by EMBRAPA - Empresa Brasileira de Pesquisa Agropecuaria, Wiley Online Library on [06/06/2025]. See the Terms and Conditions (https://onlinelibrary.wiley.com/terms-and-conditions) on Wiley Online Library for rules of use; OA articles are governed by the applicable Creative Commons License

activity in both alkaline and acidic media. In an alkaline medium, the catalyst achieved a half-wave potential of 0.88 V and a diffusion-limiting current density of 5.88 mA cm^{-2}, outperforming commercial Pt/C catalysts. Notably, it also displayed state-of-the-art performance in an acidic medium, with a half-wave potential of 0.80 V and a diffusion-limiting current density of 5.86 mA cm^{-2}, surpassing previously documented Cu-based catalysts.

Yao et al. investigated the effect of carbon defects on Cu-SACs. The catalyst exhibited significant ORR activity, characterized by a half-wave potential of 0.89 V versus RHE and a limiting current density of 6.5 mA cm^{-2}, which exceeded Pt/C catalysts. The Cu-SACs also showed remarkable durability, maintaining high activity over 30 000 cycles in ORR tests and 1100 h in Zn–air battery operation, indicating their potential for practical application in energy conversion devices.

Cu SACs have also been reported for photocatalysis application on ORR. For instance, Zhang et al. investigated the photocatalytic efficiency of single-atom Cu-doped C_3N_4 catalyst on ORR.[443] The study revealed a direct one-step electron transfer process where single-atom-induced hybridization states facilitate the direct trapping of hot carriers. Specifically, the photogenerated electron transfer time was found to be 325 fs for Cu single-atom-doped systems, which is considerably faster than the conventional two-step process. Moreover, the system exhibited a nanosecond-level photogenerated carrier lifetime, indicating high photocatalytic efficiency.

Beyond energy generation via the preferred four-electron ($4e^-$) pathway, the ORR can also proceed via a two-electron ($2e^-$) pathway to selectively produce hydrogen peroxide (H_2O_2).[135] H_2O_2 is a valuable chemical product and a green oxidant, which makes this synthesis an alternative to the energy-demanding anthraquinone process and an attractive approach for organic degradation in environment remediation applications.[444] In this context, research has demonstrated that modifications of copper materials can influence the efficiency and selectivity of ORR catalysts. Venkatesan et al. synthesized Cu-doped perovskite and investigated its electrocatalytic activity for ORR.[445] The authors observed that the catalyst selectivity increased from 30% for the undoped perovskite to 65% for the Cu-doped perovskite. Furthermore, the onset potential for the ORR was shifted to lower potential values with copper doping, indicating improved reaction kinetics. Similarly, Deng et al. synthesized Cu-doped TiO_2 and found it to be a highly selective and efficient electrocatalyst for the $2e^-$ ORR.[446] The incorporation of Cu into the TiO_2 led to lattice distortion and the formation of oxygen vacancies and Ti^{3+} species. The resulting electrocatalyst exhibited an improved onset potential of 0.79 V and a high H_2O_2 selectivity of 91.2%.

In another instance within the field of photocatalysis, Sahu et al. report a strategic heterojunction of $Zn_{0.5}Cd_{0.5}Se$ quantum dots with CuS nanosheets, resulting in an impressive H_2O_2 production rate of 3.7 mmol g^{-1} h^{-1} when exposed to visible light.[447] This performance surpasses that of the individual components. The system demonstrates sustained stability over five cycles, indicating its potential for durable application in photocatalytic H_2O_2 synthesis. Zhang et al. also attained enhanced photocatalytic ORR performance using Cu-based catalysts.[448] The authors synthesized an S-scheme heterojunction semiconductor by growing copper-indium-sulfide ($CuInS_2$) catalysts on the surface of polymeric carbon nitride (PCN) via a low-temperature hydrothermal method. The yield of H_2O_2 reached 1247.6 µmol L^{-1} h^{-1}, which was notably higher than that of PCN (107.4 µmol L^{-1} h^{-1}) and $CuInS_2$ (78.0 µmol L^{-1} h^{-1}).

In summary, despite the promise, utilizing Cu-based materials for ORR faces significant challenges. Their intrinsic catalytic activity is often lower than that of Pt, especially for the demanding $4e^-$ reduction in acidic media. Selectivity control between the $2e^-$ (H_2O_2) and $4e^-$ (H_2O/OH^-) pathways can be difficult. Perhaps most critically, stability remains a significant concern. Copper species can be prone to dissolution or oxidation state changes under electrochemical potentials, particularly in corrosive acidic environments. Furthermore, copper oxides like Cu_2O, while attractive for their light-absorbing properties in photocatalysis and photoelectrocatalysis, suffer from severe photocorrosion. Therefore, replacing Pt with Cu is economically desirable, ensuring adequate long-term stability under operating conditions emerges as a primary hurdle that must be overcome through rational material design and engineering.

3.4. Nitrogen Fixation

Ammonia (NH_3) is one of the most essential chemical and industrial products, widely used in applications such as agricultural fertilizers and artificial fibers. However, the conversion of N_2 to NH_3 poses significant challenges due to the high dissociation energy of the N≡N triple bond (941 kJ mol^{-1}) and the complex process of transferring multiple electrons and protons. The Haber-Bosch process remains the most commonly employed method for synthesizing NH_3 from N_2. Despite its widespread use, this process is highly energy-intensive, requiring elevated pressures (over 100 bar) and temperatures (500 °C), which result in substantial energy consumption and carbon emissions.[449]

In response to the limitations of the Haber-Bosch process, electrocatalytic nitrogen reduction reaction and photocatalytic nitrogen reduction reaction have emerged as promising sustainable alternatives for ammonia production. The photocatalytic N_2 fixation process relies on sustainable solar energy and water as inputs. Solar energy generates charge carriers (electrons and holes), while water provides the necessary protons to convert N_2 into NH_3 under environmentally friendly conditions. The reactions involved in photocatalytic N_2 fixation can be summarized as follows:

$$\text{Photocatalyst} \xrightarrow{h\nu} h^+ + e^- \quad (1)$$

$$2H_2O + 4h^+ \rightarrow O_2 + 4H^+ \quad (2)$$

$$N_2 + 6H^+ + 6e^- \rightarrow 2NH_3 \quad (3)$$

$$\text{Total reaction}: \ 2N_2 + 6H_2O \rightarrow 4NH_3 + 3O_2 \quad (4)$$

By directly converting solar energy into chemical energy, photocatalytic N_2 fixation presents a pathway toward zero-emission ammonia production.

The electrocatalytic N_2 reduction utilizes an external electrical potential to convert N_2 into $2NH_3$. This method offers improved operational control through product efficiency, as it can modulate the energy potential. If powered by renewable electricity sources

© 2025 The Author(s). Advanced Functional Materials published by Wiley-VCH GmbH

16163028, 0, Downloaded from https://advanced.onlinelibrary.wiley.com/doi/10.1002/adfm.202502901 by EMBRAPA - Empresa Brasileira de Pesquisa Agropecuaria, Wiley Online Library on [06/06/2025]. See the Terms and Conditions (https://onlinelibrary.wiley.com/terms-and-conditions) on Wiley Online Library for rules of use; OA articles are governed by the applicable Creative Commons License

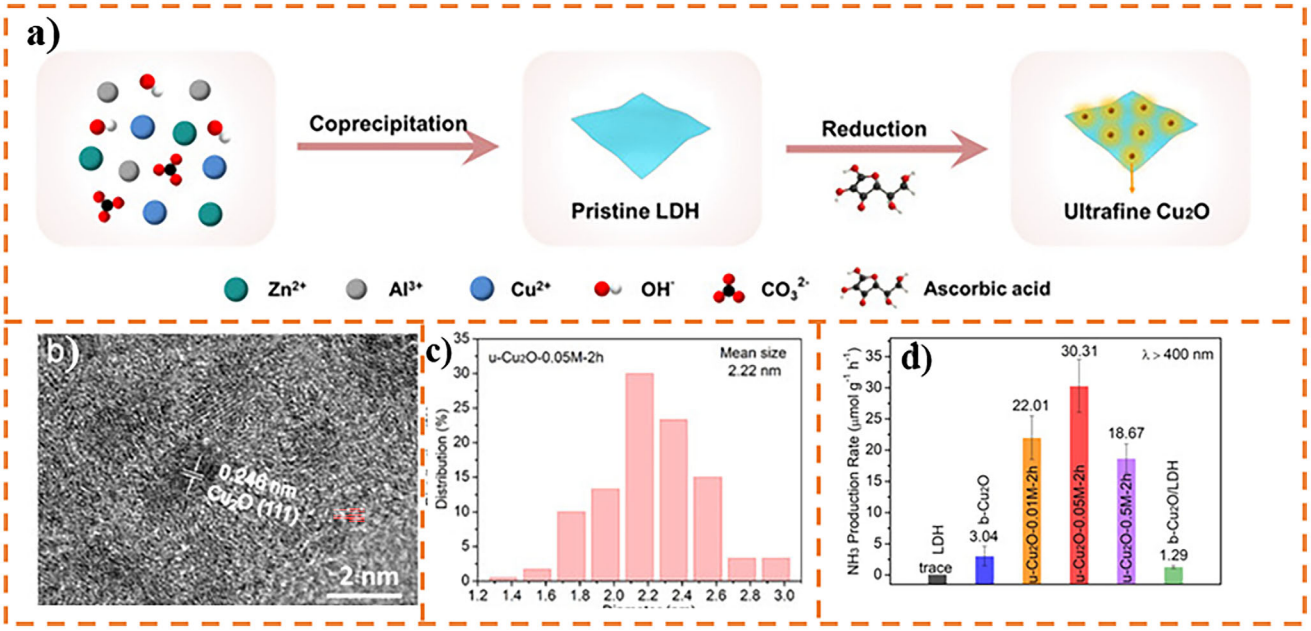

Figure 20. a) Synthetic strategy for preparing ultrafine Cu_2O-loaded LDH, b) HRTEM of u-Cu_2O-0.05M-2h, and c) the corresponding size distribution histogram, d) photocatalytic NH_3 production rate for different samples in N_2-saturated water under visible light irradiation for 1h. Reproduced with permission.[454] Copyright 2020, John Wiley and Sons.

and operated under ambient conditions, this method can also offer a potentially carbon-free route to ammonia synthesis.

While photo- and electrocatalytic N_2 reduction has seen significant progress, its broad application is still hindered by fundamental limitations. The substantial activation energy required to break the N_2 triple bond poses a considerable obstacle. In photocatalytic systems, electron-hole recombination drastically reduces quantum yields. Concurrently, in electrocatalytic environments, the HER, with its lower overpotential, outcompetes N_2 reactions in aqueous electrolytes, leading to diminished Faradaic efficiency and selectivity for ammonia synthesis. This competition is exacerbated under ambient conditions, where the overpotential gap between HER and N_2 reduction narrows.[449, 450]

Schrauzer first successfully demonstrated photocatalytic N_2 conversion to NH_3 on TiO_2.[451] Even today, many studies on N_2 fixation employ TiO_2-based systems as photocatalysts. However, the practical application of TiO_2 is significantly limited by its wide bandgap, which restricts its photoresponse to the ultraviolet (UV) region. This limitation has spurred the development of alternative materials, including BiOBr, g-C_3N_4, MoS_2, CuO, Cu_2O, etc. Cu-based photocatalysts have emerged as a promising group due to their suitable conduction and valence band positions, enabling efficient N_2 reduction and H_2O oxidation under visible light.

Among Cu-based photo and electrocatalysts, Cu_2O is the most widely utilized material for N_2 fixation. Its potential was recognized as early as 1989 when Tennakone et al.[452] demonstrated N_2 reduction to NH_3 on hydrous $Cu_2O{\cdot}xH_2O$, using CuCl as a hole scavenger. More recently, Wang et al.[453] synthesized platelike Cu_2O mesocrystals by introducing Cl^- ions as crystal growth modifiers. These mesocrystals achieved an N_2 reduction rate to NH_3 of 85.1 μmol g^{-1} h^{-1} under visible light ($\lambda > 420$ nm). The mesocrystals comprised nanocrystals with diameters of approximately 20 nm, but further size reduction to ultrafine structures (less than 10 nm) revealed surprising enhancements in activity. Zhang et al.[454] developed sub-3 nm ultrafine Cu_2O platelets via CuZnAl-layered double hydroxide (LDH) in situ topotactic transformation. This innovative approach resulted in an exceptional NH_3 production rate of 4.10 mmol gCu_2O^{-1} h^{-1} under visible light ($\lambda > 400$ nm), demonstrating the potential of nanostructured Cu_2O for high-performance photocatalytic N_2 fixation (**Figure 20**).

Despite advancements in Cu_2O-based catalysts, their N_2 fixation performance, along with that of other single-material systems, remains suboptimal. This is primarily due to the insufficient availability of active sites on the surface for N_2 adsorption and, in photocatalysts, the rapid recombination of photogenerated electron-hole pairs. Various strategies have been employed to address these challenges, including defect engineering, which involves introducing foreign metal dopants, incorporating cocatalysts, and designing plasmonic nanostructures.

Gu et al. developed a Cu-doped cobalt selenide nanosheet electrocatalyst with selenium vacancies for the electrochemical reduction of nitrate to ammonia.[455] The electrocatalyst showed a Faradaic efficiency of ≈93% and an ammonia yield rate of 2360 μg h^{-1} cm^{-2} at −0.60 V vs RHE. The study demonstrated that introducing Cu dopants and Se vacancies enhances electron transfer from Cu to Co atoms, creating electron-deficient Cu sites that facilitate nitrate dissociation and stabilize intermediates, achieving selective and efficient ammonia production.

Additionally, generating vacancies as adsorption sites and constructing heterostructures have proven effective for enhancing charge carrier separation and promoting surface reactions. For example, Iridium (Ir) clusters modified on Cu_2O{111} achieved an NH_3 yield of 173.8 μg $g_{cat.}^{-1}$ h^{-1}, which was 3.3 times higher

© 2025 The Author(s). Advanced Functional Materials published by Wiley-VCH GmbH

16163028, 0, Downloaded from https://advanced.onlinelibrary.wiley.com/doi/10.1002/adfm.202502901 by EMBRAPA - Empresa Brasileira de Pesquisa Agropecuaria, Wiley Online Library on [06/06/2025]. See the Terms and Conditions (https://onlinelibrary.wiley.com/terms-and-conditions) on Wiley Online Library for rules of use; OA articles are governed by the applicable Creative Commons License

16163028, 0, Downloaded from https://advanced.onlinelibrary.wiley.com/doi/10.1002/adfm.202502901 by EMBRAPA - Empresa Brasileira de Pesquisa Agropecuaria, Wiley Online Library on [06/06/2025]. See the Terms and Conditions (https://onlinelibrary.wiley.com/terms-and-conditions) on Wiley Online Library for rules of use; OA articles are governed by the applicable Creative Commons License

than that of pristine Cu_2O{111}.[456] This enhancement was attributed to the Ir clusters, which likely reduced the reaction energy barrier and facilitated photoinduced charge separation.

Constructing Cu_2O-based heterostructures has been a more widely adopted strategy for improving photo and electrocatalytic N_2 fixation. For example, Cui et al.[457] coated ultrafine Cu_2O (~7 nm) onto $W_{18}O_{49}$ ultrathin nanowires to form an S-scheme heterostructure with abundant oxygen vacancies. These vacancies promoted the chemisorption and activation of N_2 molecules. This system achieved an NH_3 production rate of 252.4 μmol g^{-1} h^{-1}, which was 11.8 times higher than $W_{18}O_{49}$ alone. Cu_2O clusters were combined with MIL-100(Fe) to form a heterojunction, resulting in an NH_3 production rate 25 times higher than that of MIL-100(Fe) alone.[458] This remarkable improvement was attributed to fast photogenerated electron transfer facilitated by the Cu–O surface interaction and efficient electron-hole separation enabled by the type-II heterojunction.

Biset-Peiró et al. explored using a composite electrode that combines Cu and Cu_2O to enhance nitrate conversion and titanium Ti to improve faradaic efficiency to ammonia in the electrochemical reduction of nitrate. The study found that the performance of the electrodes is highly influenced by pH and nitrate concentration. The composite electrode achieved a 92% faradaic efficiency to ammonia and productivity of 0.28 mmol $NH_3 \cdot cm^{-2} \cdot h^{-1}$ at −0.5 V vs RHE.

Zhang et al. fabricated a Cu–Cu_2O/multicomponent hydroxide heterojunction with superior N_2 adsorption ability.[459] This photochemical system achieved an NH_3 yield of over 210 μmol g^{-1} h^{-1} under full-spectrum irradiation. The multicomponent hydroxide and Cu–Cu_2O acted as oxidation and reduction sites, respectively, enabling effective charge separation and utilization. Several other efficient heterostructures have been developed for photo and electrocatalytic N_2 fixation, such as Cu_2O/g-C_3N_4,[460] Cu_2O/BiOCl,[461] Cu_2O/Cu(OH),[462] and Cu_2O/BN.[463] While Cu_2O remains the most extensively studied Cu-based catalyst, other Cu-based materials have also shown promise, often in combination with other materials to form hybrids. Examples include Cu/CuO,[117] CuO/TiO_2,[464] WO_3/CuO/Cu mesh,[465] UiO-66(−NH_2)/$CuInS_2$,[466] UiO-66(−NH_2)/Cu_7S_4,[467] Cu_2O/SnS_2/SnO_2,[468] ZnCuInS/BiOI,[469] g-C_3N_4/$CuFeO_2$.[470]

Moreover, Cu can also act as an active center for N_2 fixation, making it a versatile component in catalytic systems. Regulating and modifying the local coordination environment of metal centers in catalysts has proven to be an effective strategy for enhancing the catalyst's activity. Fang et al.[471] developed Cu single atom/$Ti_3C_2O_x$ photocatalysts. In this system, Cu sites in the Cu-N_x-Ti^{3+} structure acted as electron-rich aggregates bridged to electron-donating Ti^{3+} defects. Incorporating Cu enhanced the charge density within the asymmetric Cu-N_3-Ti^{3+} coordination environment, facilitating N_2 adsorption and activation. This design achieved an impressive NH_3 production rate of 29 μmol g^{-1} h^{-1}. Zhang et al.[472] introduced coordinatively unsaturated $Cu^{\delta+}$ into ultrathin ZnAl-LDH nanosheets, which were engineered to include abundant oxygen vacancies. The synergistic effects of the oxygen vacancies and the electron-rich $Cu^{\delta+}$ centers significantly promoted N_2 adsorption, charge separation, and transfer. The optimal photocatalyst achieved a remarkable NH_3 production rate of 110 μmol g^{-1} h^{-1}.

Wang et al. developed a novel Cu/oxygen vacancy-rich Cu-Mn_3O_4 heterostructured ultrathin nanosheet array electrocatalyst on Cu foam (Cu/Cu-Mn_3O_4NSAs/CF) using a one-step hydrothermal approach.[473] The authors demonstrated that the two-dimensional ultrathin nanosheet arrays, the heterogeneous nanointerface, and oxygen vacancies synergistically enhance the nitrate-to-ammonia activity at the active centers. The resulting Cu/Cu-Mn_3O_4 NSAs/CF catalyst demonstrated excellent performance for the electrocatalytic nitrate reduction to ammonia with high ammonia selectivity (87%) and FE (92%).

Cu^0 also plays a vital role as an electron donor in plasmonic photocatalysis. Hou et al.[474] utilized porous CuFe frameworks for photocatalytic N_2 fixation, achieving an outstanding NH_3 production rate of 342 μmol g_{cat}^{-1} h^{-1}. Mechanistic studies revealed that the surface Fe atoms served as active centers for N_2 adsorption, forming nitrogen-containing complexes. Simultaneously, the Cu frameworks generated "hot electrons" through surface plasmon resonance (SPR), enhancing the efficiency of the overall reaction.

In another interesting work, Perales-Rondon et al. fabricated copper electrodes using a 3D-printing technique for nitrate-to-ammonia conversion.[475] The 3D-printed electrodes were prepared using the fused fabrication filament printing technique with a Cu-containing filament. The 3D-printed electrodes were sintered and nanostructured using an electrochemical method, followed by a chemical treatment to produce a faceted surface. The electrodes have shown to be highly efficient for ammonia synthesis, with a faradaic efficiency of 96% and a high ammonia selectivity of 95%.

3.5. Degradation of Organic Pollutants

The world faces a severe drinking water shortage exacerbated by groundwater contamination. A significant contributor to water pollution is the release of organic pollutants from chemical industries, which often contain high concentrations of toxic and non-biodegradable substances. Common organic dyes, such as rhodamine B (RhB), methylene blue (MB), methyl orange (MO), and congo red (CR), are among the primary pollutants.

In addition to water contamination, indoor air quality has gained substantial attention recently. Volatile organic compounds (VOCs), including benzene, toluene, and formaldehyde, are some of the most prominent toxic gases threatening public health. Traditional physical and chemical methods for treating these pollutants have significant limitations, including high energy consumption and low efficiency.

To address these challenges, advanced oxidation processes (AOPs) have emerged as a sustainable and cost-effective alternative. AOPs rely on the generation of highly reactive radicals, such as hydroxyl radicals (·OH), superoxide anion radicals ($O_2^{\bullet-}$), and other reactive oxygen species (ROS), which effectively degrade organic pollutants. Common AOPs include photocatalysis, Fenton-based reactions, electrochemical oxidation, and ozonation.

Photocatalytic and electrocatalytic oxidative degradation processes leverage the generation of reactive species to decompose organic pollutants. In photocatalysis, light irradiation excites the catalyst, creating electron-hole pairs. The photogenerated holes (h^+) can directly oxidize pollutants or react with water to produce

© 2025 The Author(s). Advanced Functional Materials published by Wiley-VCH GmbH

hydroxyl radicals (•OH). Simultaneously, electrons (e^-) react with oxygen to form superoxide radicals ($O_2\bullet^-$), which may further generate singlet oxygen ($^1O_2$). These reactive oxygen species (ROS),•OH, $O_2\bullet^-$, and $^1O_2$, are potent oxidizing agents capable of degrading organic pollutants. In electrocatalysis, an applied potential drives similar oxidation reactions, generating ROS at the electrode surface.

Conventional photocatalysts such as TiO_2 and ZnO have limitations, particularly their inability to efficiently utilize visible light from the solar spectrum due to their wide band gaps. Cu-based photocatalysts, with their narrower band gaps, offer enhanced visible light absorption, making them attractive for sustainable environmental remediation. Similarly, in electrocatalysis, selecting Cu-based electrodes can optimize the generation of ROS and to improve pollutant degradation. In both photo and electrocatalysis, the tunability of Cu-based materials allows the control of reaction pathways and the efficient degradation of a wide range of organic pollutants, offering promising avenues for environmental applications.

Significant advancements in Cu-based catalysts have been achieved over the past decades. Numerous Cu-based catalysts, including Cu_2O,[476–479] CuO,[480] $CuFeO_2$,[481, 482] CuS,[483–485] Cu_2S,[486–488] $CuInS_2$,[184, 489] NiCu,[490] and CuI—triazole MOFs (CuTz-1),[491] have demonstrated exceptional effectiveness in degrading persistent pollutants such as textile and food dyes, benzene, toluene, and formaldehyde. Strategies to improve the generation and lifetime of the charge carriers have further enhanced their catalytic performance.

These strategies include doping and coupling with metals, carbon materials, or other semiconductors. Take Cu_2O, for instance; it has been extensively coupled with cocatalysts such as rGO,[492, 493] metals like Ag,[494] Cu[495, 496] Au,[101, 497] and Pt,[498] semiconductors to form a heterojunction with TiO_2,[499, 500] CuO[501, 502] BiOBr,[503] CeO_2,[504] g-C_3N_4,[505] $BiVO_4$,[506] and α-Fe_2O_3.[507] Additionally, multicomponent systems, including Cu_2O coupled with Cu/AgBr/Ag,[110] rGO/In_2O_3,[508] g-C_3N_4/ZnO,[509] Cu/CuO,[136] Cu/g-C_3N_4,[510]Cu/Fe,[511] graphite/Cu,[512] $Cu(Cr_{0.1},Al_{0.9})_2O_4$,[513] and Ag/$TiO_2$[514] have also been developed to boost catalytic performance.

Beyond the rational design and construction of catalysts for enhanced electro and photocatalytic reactions, another critical factor influencing activity is the catalyst's ability to adsorb pollutants, providing more reaction opportunities. Adsorption capacity directly affects the reaction rate, making it a limiting factor in electro and photocatalytic degradation. Various approaches have been employed to improve adsorption performance, such as increasing the surface area by reducing particle size, designing unique nanostructures, and exposing crystal facets with higher adsorption capabilities.

It is widely accepted that smaller catalyst sizes result in higher specific surface areas, which can enhance pollutant adsorption. However, there is ongoing debate about whether smaller sizes universally lead to superior catalytic activity. Cu-based catalysts with small particle sizes have been extensively utilized for pollutant degradation, often showing better catalytic performance due to their higher surface areas.[515] Contradictory findings have also been reported. For example, Karthikeyan et al.[516] synthesized Cu_2O nanocubes with tunable sizes ranging from 50 to 500 nm. They observed an inverse relationship between photocatalytic activity for phenol degradation and H_2 production and the nanocube size. They demonstrated that despite their lower surface areas, larger Cu_2O nanocubes exhibited slower radiative recombination of photoinduced electron-hole pairs, contributing to better photocatalytic performance. Conversely, Tang et al.[517] argued for an optimal size for Cu_2O nanocubes in MO degradation. By testing sizes ranging from 20 to 400 nm, they identified 30 nm as the most effective size for achieving maximum photocatalytic efficiency.

It has been reported that unique nanostructures, such as hierarchical, hollow, or porous forms, exhibit high electro and photodegradation activity. These structures offer a high surface area, which enhances the adsorption and desorption of reactants while providing more active sites for catalytic reactions. Over the years, numerous Cu-based catalysts with unique morphologies have successfully removed organic pollutants. Examples include Cu nanocubes,[518] surface-capped chalcocite (Cu_2S) snowflakes,[487] hierarchical Cu_2S microsponges,[487] graphene-like-nanosheet CuS,[519] CuO nanowires/Cu_2O,[520] multimodal hierarchical porous structured Cu_2O@nanoporous Cu composite ribbon,[521] Cu_2O nanowire arrays on Cu mesh,[522] and Cu_2O on silicon nanowires.[523] For instance, Jiang et al.[520] synthesized CuO with various morphologies, including nanowires, nanotetrahedra, and nanospheres supported on Cu_2O. These morphologies displayed significantly enhanced photocatalytic activity for methyl orange MO degradation compared to pristine Cu_2O. Among these, the CuO nanowires /Cu_2O demonstrated a specific reaction rate of 1.6 μmol min^{-1} g^{-1}, which is 260 times higher than that of pristine Cu_2O.

Furthermore, preferential adsorption of organic pollutants on specific crystal facets offers an opportunity to optimize photocatalytic performance. Studies have shown that the photocatalytic activity of Cu_2O for degrading MO is highly dependent on its exposed crystal facets.[479, 524–530] Similar facet-dependent activity of Cu_2O has been observed in the degradation of other pollutants, such as toluene,[531] MB,[477] and RhB.[478] This facet-dependent behavior has also been demonstrated in other Cu-based photocatalysts. For example, $CuFeO_2$[532] and CuO[533] have shown selective pollutant degradation activities based on their exposed crystal facets, underscoring the critical role of structural design in enhancing photocatalytic performance.

The synergistic effect of adsorption and catalytic degradation has been shown to enhance pollutant removal efficiency significantly. Improved catalytic activity can be achieved by utilizing porous materials with high surface areas to facilitate efficient pollutant adsorption. Such materials provide an ideal interface for adsorbing and accommodating organic molecules, creating a foundation for effective degradation. For example, porous KAPs-B (Knitting Aromatic compound Polymers-Benzene) with excellent adsorption ability loaded on Cu_2O for MO degradation,[534] micro-fibrous structured sepiolite immobilized Cu_2O/Cu for CR degradation,[535] Cu_2S-Cu-TiO_2 mesoporous carbon-composite for MO removal[536] and Cu_2S@ biomass carbon tube for MB degradation.[537] Zhang et al.[538] further enhanced the adsorption capacity of Cu_2O nanoparticles by supporting them on wood-based biochar (MBC). This composite material achieved an impressive maximum adsorption capacity for MO of 1610 mg g^{-1}. Leveraging an adsorption-photocatalytic degradation mechanism, the system demonstrated a

© 2025 The Author(s). Advanced Functional Materials published by Wiley-VCH GmbH

16163028, 0, Downloaded from https://advanced.onlinelibrary.wiley.com/doi/10.1002/adfm.202502901 by EMBRAPA - Empresa Brasileira de Pesquisa Agropecuaria, Wiley Online Library on [06/06/2025]. See the Terms and Conditions (https://onlinelibrary.wiley.com/terms-and-conditions) on Wiley Online Library for rules of use; OA articles are governed by the applicable Creative Commons License

photocatalytic degradation efficiency of 94.5% for MO under visible light irradiation.

This characteristic is similarly observed in electrocatalysis. For instance, Hefnawy et al. explored the adsorption behavior of CO on electrocatalytic activity for urea electrooxidation. The authors usedDFT calculations to investigate the CO tolerance of the Cu-doped NiO, showing that Cu doping can modify the electronic properties and minimize CO chemisorption, thus improving the electrode's stability and efficiency.

3.6. Organic Synthesis and Oxidation Reactions

Organic chemicals are crucial in producing many products, including pharmaceuticals, food additives, and pesticides. Over the years, the chemical industry has developed diverse methods to meet the demands of synthesizing these compounds. However, the increasing emphasis on cost reduction, environmental sustainability, and process efficiency has heightened the need for innovative and greener approaches to chemical production. Traditional methods of organic synthesis typically rely on high-temperature and high-pressure conditions, resulting in significant energy consumption and environmental impact. Furthermore, balancing high activity and selectivity in such processes is often challenging. These limitations have driven the exploration of alternative methods, with photocatalytic and electrocatalytic approaches emerging as up-and-coming solutions.

Photocatalysis and electrocatalysis offer a sustainable and energy-efficient route for organic synthesis, operating under milder reaction conditions than traditional methods. Photocatalysis harnesses solar energy, while electrocatalysis utilizes externally applied electrical potential, enabling precise control over reaction pathways and enhancing product selectivity. In photocatalysis, photogenerated charge carriers, electrons, and holes drive reduction and oxidation reactions, respectively. Similarly, in electrocatalysis, electrons are supplied or withdrawn at the electrode surface to facilitate redox transformations. The selectivity of both processes is intrinsically linked to the control of these charge transfer events.

Both catalytic systems have the key advantage of being able to direct organic synthesis through either reductive or oxidative pathways. However, achieving precise control over reaction selectivity remains a critical challenge. Cu-based catalysts have demonstrated remarkable potential in addressing this challenge owing to their tunable electronic properties and catalytic activity, making them suitable for a wide array of organic transformations.

In photocatalytic and electrocatalytic systems, the strategic use of electron or hole scavengers (or redox mediators in electrocatalysis) can significantly enhance reaction efficiency and selectivity. These species suppress undesired side reactions and promote the formation of target products. Consequently, Cu-based catalysts, when integrated with optimized reaction designs and appropriate mediators/scavengers, are increasingly recognized for their capacity to drive sustainable and selective organic synthesis processes. The integration of both photon and electron-driven catalysis opens up a broader range of reaction pathways, and the potential to combine both methods (photoelectrocatalysis) provides synergistic advantages.

3.6.1. Oxidation of Alcohols

Selective oxidation of organic compounds, particularly alcohols, has been a research subject in both photocatalysis and electrocatalysis. The redox potentials of alcohols generally align favorably with the valence band edge of many Cu-based semiconductors in photocatalysis, and with suitable potentials in electrocatalysis, making them viable catalysts. However, achieving high selectivity is crucial, as oxidation can yield multiple products, including desired carbonyl compounds (aldehydes and ketones) or undesired byproducts such as carboxylic acids and CO_2. Therefore, controlling reaction pathways to maximize selectivity is a central challenge, addressed through careful manipulation of reaction conditions—solvent choice, oxidant selection (O_2, for example), and, critically, catalyst design.

Partial oxidation of alcohols to aldehydes or ketones is of particular interest due to their significance as intermediates in synthesizing pharmaceuticals, fine chemicals, and agrochemicals. For instance, Bisht et al.[539] developed a CuO-Bi-BiOBr ternary Z-scheme photocatalytic system that efficiently oxidizes various alcohols to their corresponding aldehydes or ketones. Remarkably, this system operates in an open atmosphere and under sunlight irradiation without requiring an external oxygen source. They achieved high product selectivity (>99%) and conversion rates (>99%). In this ternary system, photogenerated electrons in the CB of BiOBr recombine with holes in the VB of CuO, facilitated by Bi bridges that enhance the recombination rate. This mechanism results in an accumulation of electrons in the CB of CuO and holes in the VB of BiOBr. The absorbed O_2 is reduced to superoxide radicals ($\cdot O_2^-$) by the electrons in CuO's CB, which subsequently oxidize alcohols to the desired aldehydes or ketones. This process, illustrated in **Figure 21a**, highlights the importance of rational catalyst design for achieving high selectivity and efficiency in targeted oxidation reactions.

The selective oxidation of benzyl alcohol to benzaldehyde is a desirable reaction due to its industrial significance. Various Cu-based catalytic systems have been explored for this purpose, including carbon quantum dots coated Cu_2O,[540] Au or Pd particle decorated Cu_2O,[541] 3D printed Cu-Cu_2O-MoS_2 composites,[542] CuO/Cu_2O heterostructure,[543] and Cu doped $SrTiO_3$.[544] These systems have demonstrated remarkable efficiency and selectivity in driving this oxidation process under mild conditions. Additionally, in an interesting study, Zhang et al. developed a method for the electrocatalytic oxidation of benzyl alcohols to benzyl aldehydes using a 3D-printed copper monosubstituted phosphotungstate-based polyacrylate resin (Cu-LPOMS@PPAR) catalyst.[545] The method uses electrochemical anodic oxidation. The authors report that the 3D-printed catalyst showed good yields of 95% and excellent functional group tolerance.

A notable trend in modern photocatalysis is the effective utilization of photogenerated electrons and holes by coupling two useful synergistic reactions—one at the reduction and the other at the oxidation sides. A particularly attractive paired reaction is the simultaneous reduction of CO_2 and oxidation of benzyl alcohol, which enables efficient use of the charge carriers and enhances overall reaction efficiency. Chen et al.[546] developed a Cu_2O/Cu nanocomposite via an in situ reduction method that successfully facilitated the production of benzyl acetate by coupling CO_2 reduction with benzyl alcohol oxidation under visible

© 2025 The Author(s). Advanced Functional Materials published by Wiley-VCH GmbH

16163028, 0, Downloaded from https://advanced.onlinelibrary.wiley.com/doi/10.1002/adfm.202502901 by EMBRAPA - Empresa Brasileira de Pesquisa Agropecuaria, Wiley Online Library on [06/06/2025]. See the Terms and Conditions (https://onlinelibrary.wiley.com/terms-and-conditions) on Wiley Online Library for rules of use; OA articles are governed by the applicable Creative Commons License

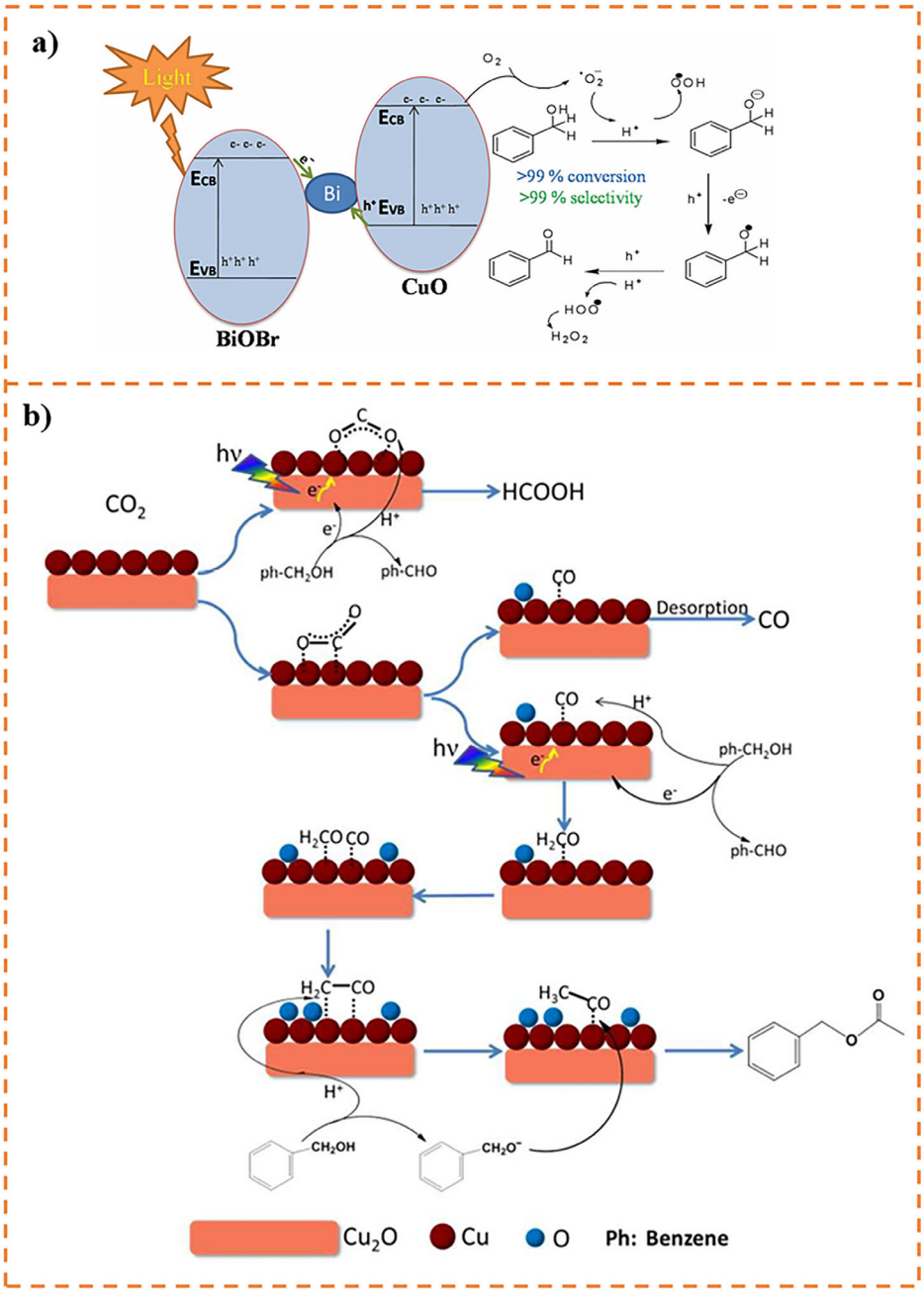

Figure 21. a) Electron transfer in CuO-Bi-BiOBr and mechanism for selective photo-oxidation of alcohols. b) Mechanism coupling of photocatalytic CO_2 reduction and benzyl alcohol oxidation to benzyl acetate. a) Reproduced with permission.[539] Copyright 2021, Royal Society of Chemistry. b) Reproduced with permission.[546] Copyright 2022, Royal Society of Chemistry.

light. The mechanism revealed that the presence of Cu^0 played a crucial role in enabling the coupling reaction (Figure 21b). Similarly, a Cu_2O-RGO/$BiVO_4$ system has been employed for simultaneous CO_2 reduction and benzyl alcohol oxidation, showcasing its versatility and potential for dual-function photocatalytic processes.[547]

For Cu-based electrocatalytic systems, alcohol oxidation has great relevance for application on direct alcohol fuel cells (DAFCs), which are being explored as efficient power sources.[548] Most studies focus on the oxidation of methanol,[549–551] ethanol,[548, 552] benzylalcohol,[553] cyclohexanol,[554] and others.

3.6.2. Oxidation of Aromatics

The hydroxylation of aromatics plays a crucial role in producing industrial chemicals such as phenol, catechol, and hydroquinone, which serve as essential precursors for

© 2025 The Author(s). Advanced Functional Materials published by Wiley-VCH GmbH

16163028, 0, Downloaded from https://advanced.onlinelibrary.wiley.com/doi/10.1002/adfm.202502901 by EMBRAPA - Empresa Brasileira de Pesquisa Agropecuaria, Wiley Online Library on [06/06/2025]. See the Terms and Conditions (https://onlinelibrary.wiley.com/terms-and-conditions) on Wiley Online Library for rules of use; OA articles are governed by the applicable Creative Commons License

pharmaceutical products and other chemical industries. Among these, phenol is in exceptionally high demand. Recently, photocatalytic phenol production from benzene has gained attention as a sustainable approach. This process typically involves either the hydroxylation of benzene, where an H atom on the aromatic ring is replaced by an OH group, or the hydrolysis of a substituent on the aromatic ring.

Zhang et al.[555] developed Cu@ZSM-5 zeolite with well-dispersed Cu single sites within the channels of the MFI structure. This material was applied in the photocatalytic hydroxylation of benzene to phenol, achieving a benzene conversion rate of 27.9% and a phenol selectivity of 97.6%. In another study, Zhang et al.[556] incorporated Cu clusters into g-C_3N_4 through a two-step thermal polymerization process, resulting in black ferromagnetic Cu-g-C_3N_4 nanosheets. The Cu-N bonding was formed by intercalating Cu atoms into a dicyandiamide-based supramolecular precursor. This photocatalytic system demonstrated an impressive benzene-to-phenol conversion rate of 90.4% with a phenol selectivity of 99.1%. Notably, it also exhibited significant activity for H_2 generation and CO_2 reduction under visible light, showcasing its capacity to drive both reduction and oxidation reactions efficiently through photogenerated electrons and holes. Additionally, other Cu-based systems have shown strong potential for benzene-to-phenol conversion. Examples include Cu-based MOFs derived from CuO@tubular carbon nitride,[557] octanethiol-modified Cu_2O-graphene,[558] and CuZnSbO.[559]

3.6.3. Oxidation of Cyclohexane

The partial oxidation of cyclohexane to KA oil, a mixture of cyclohexanol and cyclohexanone, is a crucial industrial process. KA oil is an indispensable precursor in synthesizing ε-caprolactam, a key intermediate for nylon production. Various Cu-based photocatalytic systems, including Cu-doped mesoporous TiO_2,[560] copper vanadates,[561] and Cu/carbon quantum dots,[562] have demonstrated effectiveness in this conversion. Shahzeydi et al.[563] developed a system where Cu metallic particles were immobilized on the surface of amorphous C_3N_4 (a-C_3N_4) using a pulse laser ablation technique in liquid. The photocatalytic performance for cyclohexane oxidation was optimized by varying the laser irradiation time. For instance, the Cu-20min/a-C_3N_4 catalyst achieved a 25.5% conversion of cyclohexane with 52% selectivity to adipic acid. Remarkably, with increased laser irradiation time, the Cu-40min/a-C_3N_4 catalyst exhibited an 88% cyclohexane conversion rate and 95% selectivity to KA oil, showcasing the tunable nature of this approach. Peng et al.[564] introduced a more intricate hierarchical photocatalyst, MoS_2@Cu/Cu_2O@C, which displayed significantly higher cyclohexane oxidation performance than its individual components. The superior activity was attributed to the forming of a heterojunction, which enhanced the generation and separation of photogenerated electrons and holes. Additionally, the presence of Cu^0 played a pivotal role in capturing electrons effectively and suppressing electron-hole recombination, benefiting from its LSPR effect.

Siboonruang et al. explored the electrochemical oxidation of cyclohexane to KA oil.[565] They described the reaction involving O_2 as the primary oxygen source, similar to thermochemical oxidation. Their study showed that the reaction is initiated by the formation of cyclohexyl or hydroxyl radicals, with the specific initiation step varying depending on the electrode material. They also found that undivided two-electrode cells can produce misleading results due to crossover effects, where products from one electrode interfere with the reactions at the other electrode. This research highlights the complexities of electrochemical cyclohexane oxidation and emphasizes the importance of considering factors like electrode material and reactor design for accurate analysis and optimization of the process.

3.6.4. Synthesis of Nitrogen-Containing Compounds

Imines are essential organic intermediates with broad applications in pharmaceuticals and fine chemicals. They can be synthesized through the photocatalytic oxidation of amines, offering a sustainable and efficient pathway. Cu-based systems have shown remarkable potential in this reaction. For example, a Cu-based metal–organic framework (Cu-BTC)@CuS@CeO_2 composite was employed to oxidize amines under visible to near-infrared light irradiation.[566] The enhanced performance of this system was attributed to several synergistic factors: efficient charge separation facilitated by the heterojunction, a high density of active sites, improved light absorption due to the hollow structure, and Lewis acid sites. These features collectively promoted superior photocatalytic activity. Recently, Gao et al.[567] achieved the simultaneous reduction of CO_2 and oxidation of amines using Cd-doped CdS quantum dots. This innovative system generated syngas and secondary amines in a single photoredox cycle. The presence of doped Cu improved charge separation efficiency and served as active catalytic sites, enhancing the overall reaction performance. In another recent work, Hu et al.[568] developed a Cu@CuO_x/WO_3 composite photocatalyst, which exhibited outstanding catalytic activity in converting various amine derivatives into their corresponding imines. Both experimental studies and DFTcalculations confirmed that Cu_2O served as the primary active site in this system, enabling efficient and selective amine oxidation.

Qi et al. reported an efficient and selective electrochemical method for synthesizing phenols and anilines from arylboronic acids in aqueous ammonia.[569] The technique allows for the selective formation of either phenols or anilines by changing the concentration of aqueous ammonia and the anode potential in an undivided cell. For phenol synthesis, using an aqueous ammonia concentration of 0.13 M and an anode potential of 0.6 V vs Ag/AgCl, the reaction yielded up to 92% phenols with a C—O:C—N selectivity ratio of up to 30:1. Conversely, for aniline synthesis, employing 2.61 M aqueous ammonia and an anode potential of 0.2 V vs Ag/AgCl resulted in up to 86% yield of anilines with a C—N:C—O selectivity ratio of up to 21:1. These electrochemical reactions proceeded with high reaction rates and good chemoselectivity, and without the need for alkali base, ligand, or organic solvent.

4. Comparative Analysis of Cu-Based Catalysts in Photo and Electrocatalysis

Copper is rapidly emerging as a cornerstone in sustainable catalysis, powering advancements in both photocatalysis and

© 2025 The Author(s). Advanced Functional Materials published by Wiley-VCH GmbH

16163028, 0, Downloaded from https://advanced.onlinelibrary.wiley.com/doi/10.1002/adfm.202502901 by EMBRAPA - Empresa Brasileira de Pesquisa Agropecuaria, Wiley Online Library on [06/06/2025]. See the Terms and Conditions (https://onlinelibrary.wiley.com/terms-and-conditions) on Wiley Online Library for rules of use; OA articles are governed by the applicable Creative Commons License

16163028, 0, Downloaded from https://advanced.onlinelibrary.wiley.com/doi/10.1002/adfm.202502901 by EMBRAPA - Empresa Brasileira de Pesquisa Agropecuaria, Wiley Online Library on [06/06/2025]. See the Terms and Conditions (https://onlinelibrary.wiley.com/terms-and-conditions) on Wiley Online Library for rules of use; OA articles are governed by the applicable Creative Commons License

electrocatalysis. Its abundance and cost-effectiveness position it as a compelling alternative to precious metals, driving innovation in energy conversion and environmental remediation.

Both photocatalysis and electrocatalysis leverage Cu's ability to undergo facile redox transitions, enabling efficient charge transfer processes. This is crucial for activating reactant molecules and facilitating desired chemical transformations. Moreover, Cu's versatility allows for synthesizing diverse nanostructures (e.g., nanoparticles, nanowires, oxides, sulfides), tailoring the catalyst's surface area, morphology, and electronic properties to optimize performance in specific applications. While sharing fundamental advantages, their strengths and weaknesses manifest differently across photocatalysis and electrocatalysis domains. This analysis dissects the distinct advantages and limitations of Cu-based materials across these two crucial fields.

4.1. Photocatalysis

Cu's prowess in photocatalysis stems from its unique ability to interact with light. Cu-nanomaterials exhibit localized surface plasmon resonance, enhancing light absorption across a broad spectrum, including the visible and near-infrared regions. This heightened light harvesting capability improves efficiency in organics degradation, hydrogen production, and CO_2 reduction processes. Furthermore, when coupled with semiconductors, Cu facilitates efficient charge separation, hindering electron-hole recombination and boosting catalytic performance. Cu-complexes also demonstrate strong photoexcited reducing power, enabling selective organic transformations.

However, challenges remain. Cu oxides, such as Cu_2O, can suffer from rapid electron-hole recombination and photocorrosion, limiting their long-term stability. Cu can unexpectedly exhibit an oxidizing role in certain systems, counteracting the desired reduction processes. Achieving high selectivity for specific products can also be difficult, and leaching of Cu species can occur, raising environmental concerns.

4.2. Electrocatalysis

Cu-based electrocatalysts demonstrate excellent activity towards various electrochemical reactions, including the oxygen evolution reaction (OER), hydrogen evolution reaction, and CO_2 electroreduction.

In electrocatalysis, Cu stands out as the only monometallic catalyst capable of reducing CO_2 into valuable multicarbon products like hydrocarbons and alcohols with appreciable efficiency. The catalytic properties of Cu can be finely tuned by controlling its particle size, morphology, and surface composition, allowing for the optimization of specific electrochemical reactions. Modifying Cu with other metals can effectively suppress the competing hydrogen evolution reaction, enhancing selectivity for CO_2 reduction products. Advanced reactor configurations, like gas diffusion electrodes, amplify catalytic current densities, signifying rapid reaction rates.

Despite these strengths, electrocatalytic CO_2 reduction on Cu catalysts often requires significant overpotentials, leading to lower energy efficiency. The HER remains a persistent competitor, and achieving high selectivity for a single desired product among the multitude of possibilities presents a considerable challenge. Cu catalysts are also susceptible to poisoning and deactivation by adsorbed species, and leaching can occur under electrochemical conditions. The complex, multistep nature of CO_2 electroreduction on copper necessitates further research to elucidate and control the reaction pathways fully.

4.3. Final Perspectives

Copper-based catalysts hold immense promise for advancing sustainable technologies in photocatalysis and electrocatalysis. While challenges such as stability and selectivity remain, ongoing research on material design, surface engineering, and reaction optimization continuously expands their capabilities. Copper's unique properties and economic viability firmly establish it as a key player in the quest for cleaner energy and a more sustainable future.

5. Conclusion

As the urgency of addressing climate change and the global energy crisis intensifies, Cu-based catalysts stand out as versatile and accessible materials capable of meeting these demands. Their excellent electrical conductivity, inherent catalytic activity, abundance, affordability, and adaptability lay a solid foundation for continued innovation, ensuring their pivotal role in transitioning towards sustainable energy and a cleaner environment. The practical application of Cu-based catalysts faces hurdles; however, as research continues to delve into their synthesis, characterization, and application, it is expected that further improvements in their catalytic efficiency, selectivity, and stability will be attained. From our perspective, while the practical application of Cu-based catalysts encounters certain challenges, ongoing research into their synthesis, characterization, and application is anticipated to yield enhancements in their catalytic efficiency, selectivity, and stability. The development of novel heterostructures, single-atom catalysts, and advanced modification techniques holds the potential to unlock unprecedented catalytic capabilities and expand the applicability of these materials across diverse fields. By bridging fundamental research with scalable applications, Cu-based catalysts could help pave the way to achieving ambitious climate and energy goals, making the future of these materials vast with the potential for advancing renewable energy and environmental technology.

Acknowledgements

J.C.d.A., Y.W., and T.A.R. contributed equally to this work. The authors are grateful to the BRICS STI Framework Programme (52261145703), CNPq/MCTI/BRICS-STI (Grant No. 440117/2022-4), CNPq (Grant Nos. 406026/2023-8, 385120/2024-9, and 407878/2022-0), FAPESP (Grant Nos: 2024/16381-8, 2018/01258-5, 2022/01787-3, and 2017/11986-5) and FAPEMIG (Grant Nos. APQ-06609-24, APQ-00366-24, APQ-02473-23, APQ-04311-23) for financial support. CAPES (Coordination for the Improvement of Higher Education Personnel Finance Code 001); Agronano Network (Embrapa Research Network); and SISNANO/ MCTI, FINEP (Grant No. 1516 #01.17.0021.00) and MCTI/FINEP/FNDCT (Grant No.

 © 2025 The Author(s). Advanced Functional Materials published by Wiley-VCH GmbH

0966/24 #01.25.0086.00). The authors also acknowledge the support of Brazilian S&T&I Ministry through SISNANO (CNPq proj #442575/2019-0) and INCT Programs (CNPq proj #406925/2022-4). D.B. and A.E. are grateful to the funding from the Russian Federation represented by the Ministry of Science and Higher Education, Russia (Grant No. 075-15-2022-1223). J.H.P., Y.W., and T.H. are grateful for the supports from the National Natural Science Foundation of China (Grant Nos. 51772094 and 22461142141).

Open access funding enabled and organized by Projekt DEAL.

Conflict of Interest

The authors declare no conflict of interest.

Keywords

classification, Copper-based catalysts, environmental remediation, methods, Photo- and electrocatalysis, sustainable energy, synthesis

Received: January 30, 2025
Revised: April 11, 2025
Published online:

[1] J. Baillie, Y.-P. Zhang, *Science* **2018**, *361*, 1051.
[2] H. Ritchie, L. Rodés-Guirao, E. Mathieu, M. Gerber, E. Ortiz-Ospina, J. Hasell, M. Roser, *Population Growth* **2023**.
[3] Y. Lu, Z. A. Khan, M. S. Alvarez-Alvarado, Y. Zhang, Z. Huang, M. Imran, *Sustainability* **2020**, *12*, 5078.
[4] W. Z. Lidicker, *Global Ecol. Conserv.* **2020**, *24*, 01232.
[5] J. H. Brown, W. R. Burnside, A. D. Davidson, J. P. DeLong, W. C. Dunn, M. J. Hamilton, N. Mercado-Silva, J. C. Nekola, J. G. Okie, W. H. Woodruff, W. Zuo, *BioScience* **2011**, *61*, 19.
[6] H. Ritchie, P. Rosado, M. Roser, *Energy Prod. Consumption* **2024**.
[7] A. Qazi, F. Hussain, N. A. Rahim, G. Hardaker, D. Alghazzawi, K. Shaban, K. Haruna, *IEEE Access* **2019**, *7*, 63837.
[8] M. Qu, P. Ahponen, L. Tahvanainen, D. Gritten, B. Mola-Yudego, P. Pelkonen, *Renewable Sustainable Energy Rev.* **2011**, *15*, 3649.
[9] A. M. Saleh, A. B. Haris, N. B. Ahmad, *Int. J. Energy Econ. Policy* **2014**, *4*, 26.
[10] A. Raheem, S. A. Abbasi, A. Memon, S. R. Samo, Y. H. Taufiq-Yap, M. K. Danquah, R. Harun, *Energy, Sustain. Soc.* **2016**, *6*, 16.
[11] N. Saracoglu, G. Gunduz, *Energy Sources, Pt. A: Recov., Utiliz., Environ. Effects* **2009**, *31*, 1708.
[12] F. Fornara, P. Pattitoni, M. Mura, E. Strazzera, *J. Environ. Psychol.* **2016**, *45*, 1.
[13] A. Mardani, A. Jusoh, E. Zavadskas, F. Cavallaro, Z. Khalifah, *Sustainability* **2015**, *7*, 13947.
[14] T. Kousksou, P. Bruel, A. Jamil, T. El Rhafiki, Y. Zeraouli, *Sol. Energy Mater. Sol. Cells* **2014**, *120*, 59.
[15] K. P. Tsagarakis, A. Mavragani, A. Jurelionis, I. Prodan, T. Andrian, D. Bajare, A. Korjakins, S. Magelinskaite-Legkauskiene, V. Razvan, L. Stasiuliene, *Renewable Energy* **2018**, *121*, 412.
[16] H. Ritchie, P. Rosado, M. Roser (**2023**), Primary energy consumption from fossil fuels, nuclear and renewables Published online at OurWorldinData.org. Retrieved from:, https://ourworldindata.org/grapher/sub-energy-fossil-renewables-nuclear?tab=table.
[17] H. Ritchie, P. Rosado, M. Roser, *Energy* **2024**.
[18] H. Lucas, S. Pinnington, L. F. Cabeza, *Sol. Energy* **2018**, *173*, 449.
[19] P. Trop, D. Goricanec, *Energy* **2016**, *108*, 155.
[20] O. M. de la Salud, W. H. Organization, E. C. E. Health, *WHO Global Air Quality Guidelines: Particulate Matter (PM2.5 and PM10), Ozone, Nitrogen Dioxide, Sulfur Dioxide and Carbon Monoxide*, World Health Organization, Geneva, Switzerland **2021**.
[21] S. Federal, *Protocolo de Quioto e Legislação Correlata*, Senado Federal, Secretaria Especial de Editoração e Publicação, Brasília **2004**.
[22] A. L. Junges, V. Y. Santos, N. T. Massoni, *Experiências em Ensino de Ciências* **2018**, *13*, 126.
[23] S. G. Philander, *Encyclopedia of Global Warming and Climate Change*, SAGE, Los Angeles, CA **2008**.
[24] D. De Wrachien, B. Schultz, M. B. Goli, *Irrigation Drainage* **2021**, *70*, 981.
[25] R. M. Goody, J. C. G. Walker, *Atmosferas Planetárias* (Ed.: E. Blucher), Prentice-Hall, Inc., Hoboken, NJ **1972**.
[26] D. G. Kaufman, *Biosphere 2000: Protecting Our Global Environment*, Kendall/Hunt Pub. Co., Dubuque, IA **2000**.
[27] D. J. Hofmann, J. H. Butler, P. P. Tans, *Atmos. Environ.* **2009**, *43*, 2084.
[28] G. P. Peters, R. M. Andrew, J. G. Canadell, P. Friedlingstein, R. B. Jackson, J. I. Korsbakken, C. Le Quéré, A. Peregon, *Nat. Clim. Chang.* **2020**, *10*, 3.
[29] S. Roe, C. Streck, M. Obersteiner, S. Frank, B. Griscom, L. Drouet, O. Fricko, M. Gusti, N. Harris, T. Hasegawa, Z. Hausfather, P. Havlík, J. House, G.-J. Nabuurs, A. Popp, M. J. S. Sánchez, J. Sanderman, P. Smith, E. Stehfest, D. Lawrence, *Nat. Clim. Chang.* **2019**, *9*, 817.
[30] H. Ritchie, P. Rosado, M. Roser, *Per capita CO_2 emissions* **2024**.
[31] A. Rafiee, K. Rajab Khalilpour, D. Milani, M. Panahi, *J. Environ. Chem. Eng.* **2018**, *6*, 5771.
[32] H. Ritchie, P. Rosado, M. Roser, *Greenhouse gas emissions by gas* **2024**.
[33] UN, *Paris agreement* **2015**.
[34] S. Fawzy, A. I. Osman, J. Doran, D. W. Rooney, *Environ. Chem. Lett.* **2020**, *18*, 2069.
[35] World Meteorological Organization, *Proceedings of the World Climate Conference: A Conference of Experts on Climate and Mankind Geneva, 12–23 February 1979*, Secretariat of the World Meteorological Organization, Geneva, **1979**.
[36] United Nations Framework Convention on Climate Change. What is the Kyoto Protocol?, https://unfccc.int/kyoto_protocol (accessed: January 2025).
[37] IPCC, *Global Warming of 1.5°C. An IPCC Special Report on the impacts of global warming of 1.5°C above pre-industrial levels and related global greenhouse gas emission pathways, in the context of strengthening the global response to the threat of climate change, sustainable development, and efforts to eradicate poverty* (Eds: V. Masson-Delmotte, P. Zhai, H.-O. Pörtner, D. Roberts, J. Skea, P. R. Shukla, A. Pirani, W. Moufouma-Okia, C. Péan, R. Pidcock, S. Connors, J. B. R. Matthews, Y. Chen, X. Zhou, M. I. Gomis, E. Lonnoy, T. Maycock, M. Tignor, T. Waterfield), Cambridge University Press, Cambridge, UK .**2018**.
[38] E. Bevacqua, C.-F. Schleussner, J. Zscheischler, *Nat. Clim. Chang.* **2025**, *15*, 262.
[39] N. M. Hosny, I. Gomaa, M. G. Elmahgary, *Appl. Surface Sci. Adv.* **2023**, *15*, 100395.
[40] Y. Chen, M. Lin, D. Zhuang, *Chemosphere* **2022**, *297*, 133932.
[41] M. Petrovic, Gonzalez, S., Barceló, D., *TrAC, Trends Anal. Chem.* **2003**, *22*, 685.
[42] D. Papagiannaki, M. H. Belay, N. P. F. Gonçalves, E. Robotti, A. Bianco-Prevot, R. Binetti, P. Calza, *Chem. Eng. J. Adv.* **2022**, *10*, 100245.
[43] A. N. M. A. Haque, N. Sultana, A. S. M. Sayem, S. A. Smriti, *Sustainability* **2022**, *14*, 11098.
[44] R. O. Alves De Lima, A. P. Bazo, D. M. F. Salvadori, C. M. Rech, D. De Palma Oliveira, G. De Aragão Umbuzeiro, *Mutation Res./Genetic Toxicol. Environ. Mutagenesis* **2007**, *626*, 53.
[45] V. Vaiano, I. De Marco, *Separations* **2023**, *10*, 230.
[46] M. Popović, S. Morović, M. Kovačić, K. Košutić, *Membranes* **2024**, *14*, 239.
[47] H. K. Bayabil, F. T. Teshome, Y. C. Li, *Front. Environ. Sci.* **2022**, *10*, 873499.

© 2025 The Author(s). Advanced Functional Materials published by Wiley-VCH GmbH

16163028, 0, Downloaded from https://advanced.onlinelibrary.wiley.com/doi/10.1002/adfm.202502901 by EMBRAPA - Empresa Brasileira de Pesquisa Agropecuaria, Wiley Online Library on [06/06/2025]. See the Terms and Conditions (https://onlinelibrary.wiley.com/terms-and-conditions) on Wiley Online Library for rules of use; OA articles are governed by the applicable Creative Commons License

[48] A. Boretti, L. Rosa, *npj Clean Water* **2019**, *2*, 15.
[49] S. Ali, A. Razzaq, H. Kim, S.-I. In, *Chem. Eng. J.* **2022**, *429*, 131579.
[50] M. B. Gawande, A. Goswami, F.-X. Felpin, T. Asefa, X. Huang, R. Silva, X. Zou, R. Zboril, R. S. Varma, *Chem. Rev.* **2016**, *116*, 3722.
[51] G. Pacchioni, *ACS Catal.* **2024**, *14*, 2730.
[52] A. E. A. Gent, *Methanol production* **1976**.
[53] R. Guil-López, N. Mota, J. Llorente, E. Millán, B. Pawelec, J. L. G. Fierro, R. M. Navarro, *Materials* **2019**, 12.
[54] M. Savy, S. B. G. Magner, *Comptes Rendus Hebdomadaires Des Seances De L Academie Des Sciences Serie C* **1968**, *267*, 863.
[55] B. IN, *USSR* **1968**, *42*, 1036.
[56] K. Hirano, K. Inoue, T. Yatsu, *J. Photochem. Photobiol. A: Chem.* **1992**, *64*, 255.
[57] Y. Hori, K. Kikuchi, A. Murata, S. Suzuki, *Chem. Lett.* **1986**, *15*, 897.
[58] Y. Hori, K. Kikuchi, S. Suzuki, *Chem. Lett.* **1985**, *14*, 1695.
[59] A. Murata, Y. Hori, *Bull. Chem. Soc. Jpn.* **1991**, *64*, 123.
[60] K. Adachi, K. Ohta, T. Mizuno, *Sol. Energy* **1994**, *53*, 187.
[61] C.-C. Yang, Y.-H. Yu, B. van der Linden, J. C. S. Wu, G. Mul, *J. Am. Chem. Soc.* **2010**, *132*, 8398.
[62] K. A. Adegoke, R. O. Adegoke, A. O. Ibrahim, S. A. Adegoke, O. S. Bello, *Sustainable Mater. Technol.* **2020**, *25*, 00200.
[63] S. Nitopi, E. Bertheussen, S. B. Scott, X. Liu, A. K. Engstfeld, S. Horch, B. Seger, I. E. L. Stephens, K. Chan, C. Hahn, J. K. Nørskov, T. F. Jaramillo, I. Chorkendorff, *Chem. Rev.* **2019**, *119*, 7610.
[64] I. A. Rutkowska, A. Wadas, E. Szaniawska, A. Chmielnicka, A. Zlotorowicz, P. J. Kulesza, *Curr. Opin. Electrochem.* **2020**, *23*, 131.
[65] S. J. Hoseini, R. H. Fath, *RSC Adv.* **2016**, *6*, 76964.
[66] C. Y. Toe, Z. Zheng, H. Wu, J. Scott, R. Amal, Y. H. Ng, *Angew. Chem. Int. Ed.* **2018**, *57*, 13613.
[67] G. M. Tomboc, S. Choi, T. Kwon, Y. J. Hwang, K. Lee, *Adv. Mater.* **2020**, *32*, 1908398.
[68] D.-E. Lee, S. Moru, R. Bhosale, W.-K. Jo, S. Tonda, *Appl. Surf. Sci.* **2022**, *599*, 153973.
[69] Y. Yu, X. Dong, P. Chen, Q. Geng, H. Wang, J. Li, Y. Zhou, F. Dong, *ACS Nano* **2021**, *15*, 14453.
[70] Y. Yu, Y. He, P. Yan, S. Wang, F. Dong, *Proc. Natl. Acad. Sci. U.S.A.* **2023**, *120*, 2307320120.
[71] H. Khan, R. C. Pawar, H. Charles, C. S. Lee, *Appl. Surf. Sci.* **2023**, *636*, 157832.
[72] A. E. Nogueira, J. A. Oliveira, G. T. S. T. Da Silva, C. Ribeiro, *Sci. Rep.* **2019**, *9*, 1316.
[73] S. Singh, R. Punia, K. K. Pant, P. Biswas, *Chem. Eng. J.* **2022**, *433*, 132709.
[74] T. Li, N. Tsubaki, Z. Jin, *J. Mater. Sci. Technol.* **2024**, *169*, 82.
[75] J. A. Torres, J. C. Da Cruz, A. E. Nogueira, G. T. S. T. Da Silva, J. A. De Oliveira, C. Ribeiro, *J. Environ. Chem. Eng.* **2022**, *10*, 107291.
[76] Y. Xin, K. Yu, L. Zhang, Y. Yang, H. Yuan, H. Li, L. Wang, J. Zeng, *Adv. Mater.* **2021**, *33*, 2008145.
[77] S. C. Priya, S. Vijayalakshmi, S. G. Raghavendra, S. Yıldızhan, J. Ranjitha, *Mater. Today: Proc.* **2023**, *80*, 3075.
[78] X. Li, J. You, J. Li, Z. Wang, Y. Zhao, J. Xu, M. Duan, H. Zhang, *ChemCatChem* **2024**, *16*, 202301108.
[79] C. Li, J. He, Y. Xiao, Y. Li, J.-J. Delaunay, *Energy Environ. Sci.* **2020**, *13*, 3269.
[80] F. Hu, X. Xu, Y. Sun, C. Hu, S. Shen, Y. Wang, L. Gong, L. Li, S. Peng, *Angew. Chem., Int. Ed.* **2025**, *64*, 202419456.
[81] F. Zhong, R. Li, B. K. Mai, P. Liu, G. C. Fu, *Nature* **2025**, *640*, 107.
[82] C. Li, J. Wang, *Small* **2024**, *20*, 2404798.
[83] A. D. Kute, R. P. Gaikwad, I. R. Warkad, M. B. Gawande, *Green Chem.* **2022**, *24*, 3502.
[84] B. K. Ghosh, S. Hazra, B. Naik, N. N. Ghosh, *Powder Technol.* **2015**, *269*, 371.
[85] Q. Liu, D. Zhou, Y. Yamamoto, R. Ichino, M. Okido, *Trans. Nonferrous Metals Soc. China* **2012**, *22*, 117.
[86] M. Jin, G. He, H. Zhang, J. Zeng, Z. Xie, Y. Xia, *Angew. Chem., Int. Ed.* **2011**, *50*, 10560.
[87] J. Xiong, Y. Wang, Q. Xue, X. Wu, *Green Chem.* **2011**, *13*, 900.
[88] S. V. Saikova, S. A. Vorob'ev, R. B. Nikolaeva, Y.u. L. Mikhlin, *Russ. J. Gen. Chem.* **2010**, *80*, 1122.
[89] Y. Wang, A. V. Biradar, G. Wang, K. K. Sharma, C. T. Duncan, S. Rangan, T. Asefa, *Chem. Eur. J.* **2010**, *16*, 10735.
[90] P. K. Khanna, S. Gaikwad, P. V. Adhyapak, N. Singh, R. Marimuthu, *Mater. Lett.* **2007**, *61*, 4711.
[91] S. Yokoyama, H. Takahashi, T. Itoh, K. Motomiya, K. Tohji, *Adv. Powder Technol.* **2014**, *25*, 999.
[92] J. Albo Sánchez, M. I. Qadir, M. Samperi, J. Alves Fernandes, I. de Pedro del Valle, J. Dupont, *Chem. Eng. J.* **2021**, *404*, 126643.
[93] L. Xiao, Q. Zhang, P. Chen, L. Chen, F. Ding, J. Tang, Y.-J. Li, C.-T. Au, S.-F. Yin, *Appl. Catal., B* **2019**, *248*, 380.
[94] S. Zhang, B. Peng, S. Yang, H. Wang, H. Yu, Y. Fang, F. Peng, *Int. J. Hydrogen Energy* **2015**, *40*, 303.
[95] Q. Yang, M. Long, L. Tan, Y. Zhang, J. Ouyang, P. Liu, A. Tang, *ACS Appl. Mater. Interfaces* **2015**, *7*, 12719.
[96] Q. Shen, Z. Chen, X. Huang, M. Liu, G. Zhao, *Environ. Sci. Technol.* **2015**, *49*, 5828.
[97] E. Kazuma, T. Yamaguchi, N. Sakai, T. Tatsuma, *Nanoscale* **2011**, *3*, 3641.
[98] C. Peng, P. Wei, X. Li, Y. Liu, Y. Cao, H. Wang, H. Yu, F. Peng, L. Zhang, B. Zhang, *Nano Energy* **2018**, *53*, 97.
[99] X.-J. Lv, S.-X. Zhou, C. Zhang, H.-X. Chang, Y. Chen, W.-F. Fu, *J. Mater. Chem.* **2012**, *22*, 18542.
[100] P. Zhang, T. Song, T. Wang, H. Zeng, *Appl. Catal., B* **2017**, *206*, 328.
[101] P. Zhang, T. Song, T. Wang, H. Zeng, *Appl. Catal., B* **2018**, *225*, 172.
[102] S. Cao, C.-J. Wang, G.-Q. Wang, Y. Chen, X.-J. Lv, W.-F. Fu, *RSC Adv.* **2020**, *10*, 5930.
[103] R. Gleißner, H. Noei, S. Chung, G. D. L. Semione, E. E. Beck, A.-C. Dippel, O. Gutowski, G. Gizer, V. Vonk, A. Stierle, *J. Phys. Chem. C* **2021**, *125*, 23561.
[104] X. Guo, C. Hao, G. Jin, H.-Y. Zhu, X.-Y. Guo, *Angew. Chem., Int. Ed.* **2014**, *53*, 1973.
[105] W. J. Foo, C. Zhang, G. W. Ho, *Nanoscale* **2013**, *5*, 759.
[106] L. Zhang, Y. Yang, Z. Zhou, J. Li, G. Chen, L. Zhou, Y. Qiu, Y. Sun, *Chem. Eng. J.* **2023**, *452*, 139273.
[107] Y.-F. Zhang, L.-G. Qiu, Y.-P. Yuan, Y.-J. Zhu, X. Jiang, J.-D. Xiao, *Appl. Catal., B* **2014**, *144*, 863.
[108] I. Mondal, S. Gonuguntla, U. Pal, *J. Phys. Chem. C* **2019**, *123*, 26073.
[109] I. Shown, H.-C. Hsu, Y.-C. Chang, C.-H. Lin, P. K. Roy, A. Ganguly, C.-H. Wang, J.-K. Chang, C.-I. Wu, L.-C. Chen, *Nano Lett.* **2014**, *14*, 6097.
[110] J. He, D. W. Shao, L. C. Zheng, L. J. Zheng, D. Q. Feng, J. P. Xu, X. H. Zhang, W. C. Wang, W.-H. Wang, F. Lu, *Appl. Catal., B* **2017**, *203*, 917.
[111] Z. Li, J. Liu, D. Wang, Y. Gao, J. Shen, *Int. J. Hydrogen Energy* **2012**, *37*, 6431.
[112] F. Zhang, Y.-H. Li, M.-Y. Qi, Z.-R. Tang, Y.-J. Xu, *Appl. Catal., B* **2020**, *268*, 118380.
[113] D. Gupta, S. R. Meher, N. Illyaskutty, Z. C. Alex, *J. Alloys Compd.* **2018**, *743*, 737.
[114] J. Liu, X. Huang, Y. Li, K. M. Sulieman, X. He, F. Sun, *Cryst. Growth Des.* **2006**, *6*, 1690.
[115] J. C. De Almeida, T. A. Rodrigues, G. T. S. T. Da Silva, C. Ribeiro, V. R. De Mendonça, *Mater. Adv.* **2024**, *5*, 6479.
[116] X. Jiang, T. Herricks, Y. Xia, *Nano Lett.* **2002**, *2*, 1333.
[117] J. Zhao, Z. Shen, J. Yu, Y. Guo, M. A. Mushtaq, Y. Ding, Z. Song, W. Zhang, X. Huang, Y. Li, D. Liu, X. Cai, *J. Hazard. Mater.* **2022**, *439*, 129653.
[118] F. Teng, W. Yao, Y. Zheng, Y. Ma, Y. Teng, T. Xu, S. Liang, Y. Zhu, *Sens. Actuators, B* **2008**, *134*, 761.

© 2025 The Author(s). Advanced Functional Materials published by Wiley-VCH GmbH

16163028, 0, Downloaded from https://advanced.onlinelibrary.wiley.com/doi/10.1002/adfm.202502901 by EMBRAPA - Empresa Brasileira de Pesquisa Agropecuaria, Wiley Online Library on [06/06/2025]. See the Terms and Conditions (https://onlinelibrary.wiley.com/terms-and-conditions) on Wiley Online Library for rules of use; OA articles are governed by the applicable Creative Commons License

[119] A. Umar, A. A. Alshahrani, H. Algarni, R. Kumar, *Sens. Actuators, B* **2017**, *250*, 24.
[120] M. I. Said, A. A. Othman, *RSC Adv.* **2021**, *11*, 37801.
[121] A. Hajnorouzi, *Ultrason. Sonochem.* **2020**, *64*, 105020.
[122] X.-Y. Yu, R.-X. Xu, C. Gao, T. Luo, Y. Jia, J.-H. Liu, X.-J. Huang, *ACS Appl. Mater. Interfaces* **2012**, *4*, 1954.
[123] A. Aslani, *Phys. B* **2011**, *406*, 150.
[124] Z. Hong, Y. Cao, J. Deng, *Mater. Lett.* **2002**, *52*, 34.
[125] G. D. Moon, J. B. Joo, I. Lee, Y. Yin, *Nanoscale* **2014**, *6*, 12002.
[126] J. F. de Brito, F. Tavella, C. Genovese, C. Ampelli, M. V. B. Zanoni, G. Centi, S. Perathoner, *Appl. Catal., B* **2018**, *224*, 136.
[127] S. Harish, J. Archana, M. Sabarinathan, M. Navaneethan, K. D. Nisha, S. Ponnusamy, C. Muthamizhchelvan, H. Ikeda, D. K. Aswal, Y. Hayakawa, *Appl. Surf. Sci.* **2017**, *418*, 103.
[128] J.-Y. Ho, M. H. Huang, *J. Phys. Chem. C* **2009**, *113*, 14159.
[129] G.-Z. Yuan, C.-F. Hsia, Z.-W. Lin, C. Chiang, Y.-W. Chiang, M. H. Huang, *Chem. Eur. J.* **2016**, *22*, 12548.
[130] C.-Y. Chu, M. H. Huang, *J. Mater. Chem. A* **2017**, *5*, 15116.
[131] A. Radi, D. Pradhan, Y. Sohn, K. T. Leung, *ACS Nano* **2010**, *4*, 1553.
[132] Y. Luo, Y. Tu, Q. Ren, X. Dai, L. Xing, J. Li, *J. Solid State Chem.* **2009**, *182*, 182.
[133] G. Wang, R. van den Berg, C. de Mello Donega, K. P. de Jong, P. E. de Jongh, *Appl. Catal., B* **2016**, *192*, 199.
[134] F. H. Alsultany, S. F. H. Alhasan, E. T. Salim, *J. Inorg. Organomet. Polym. Mater.* **2021**, *31*, 3749.
[135] Q. Zhai, S. Xie, W. Fan, Q. Zhang, Y. Wang, W. Deng, Y. Wang, *Angew. Chem., Int. Ed.* **2013**, *52*, 5776.
[136] H. Li, Z. Su, S. Hu, Y. Yan, *Appl. Catal., B* **2017**, *207*, 134.
[137] S. Mosleh, M. R. Rahimi, M. Ghaedi, K. Dashtian, S. Hajati, *Ultrason. Sonochem.* **2018**, *40*, 601.
[138] M. Iqbal, Y. Wang, H. Hu, M. He, A. H. Shah, L. Lin, P. Li, K. Shao, A. R. Woldu, T. He, *Appl. Surf. Sci.* **2018**, *443*, 209.
[139] J. Chen, S. Shen, P. Guo, M. Wang, P. Wu, X. Wang, L. Guo, *Appl. Catal., B* **2014**, *152*, 335.
[140] X. Zhong, Y. Zhu, Q. Sun, M. Jiang, J. Li, J. Yao, *Chem. Eng. J.* **2022**, *442*, 136156.
[141] X. Zou, H. Fan, Y. Tian, S. Yan, *CrystEngComm* **2014**, *16*, 1149.
[142] W. Wang, C. Deng, S. Xie, Y. Li, W. Zhang, H. Sheng, C. Chen, J. Zhao, *J. Am. Chem. Soc.* **2021**, *143*, 2984.
[143] H. Huang, J. Zhang, L. Jiang, Z. Zang, *J. Alloys Compd.* **2017**, *718*, 112.
[144] P. D. Tran, S. K. Batabyal, S. S. Pramana, J. Barber, L. H. Wong, S. C. J. Loo, *Nanoscale* **2012**, *4*, 3875.
[145] D. Mateo, J. Albero, H. García, *Energy Environ. Sci.* **2017**, *10*, 2392.
[146] Z. Wang, S. Zhao, S. Zhu, Y. Sun, M. Fang, *CrystEngComm* **2011**, *13*, 2262.
[147] R. Gusain, P. Kumar, O. P. Sharma, S. L. Jain, O. P. Khatri, *Appl. Catal., B* **2016**, *181*, 352.
[148] U. A. Joshi, A. M. Palasyuk, P. A. Maggard, *J. Phys. Chem. C* **2011**, *115*, 13534.
[149] N. King, P. P. Sahoo, L. Fuoco, S. Stuart, D. Dougherty, Y. Liu, P. A. Maggard, *Chem. Mater.* **2014**, *26*, 2095.
[150] P. P. Sahoo, B. Zoellner, P. A. Maggard, *J. Mater. Chem. A* **2015**, *3*, 4501.
[151] N. King, R. D. Sommer, P. Watkins-Curry, J. Y. Chan, P. A. Maggard, *Cryst. Growth Des.* **2015**, *15*, 552.
[152] I. Sullivan, P. P. Sahoo, L. Fuoco, A. S. Hewitt, S. Stuart, D. Dougherty, P. A. Maggard, *Chem. Mater.* **2014**, *26*, 6711.
[153] Q.-L. Liu, Z.-Y. Zhao, R.-D. Zhao, J.-H. Yi, *J. Alloys Compd.* **2020**, *819*, 153032.
[154] Y. Wang, H. Wang, A. R. Woldu, X. Zhang, T. He, *Catal. Today* **2019**, *335*, 388.
[155] Y. Wang, H. Wang, T. He, *Chemosphere* **2021**, *264*, 128508.
[156] L. Tian, Z.-J. Tang, L.-Y. Hao, T. Dai, J.-P. Zou, Z.-Q. Liu, *Angew. Chem.* **2024**, *136*, 202401434.
[157] K. Shetty, L. Renuka, H. P. Nagaswarupa, H. Nagabhushana, K. S. Anantharaju, D. Rangappa, S. C. Prashantha, K. Ashwini, *Mater. Today: Proc.* **2017**, *4*, 11806.
[158] R. Li, M. Cai, Z. Xie, Q. Zhang, Y. Zeng, H. Liu, G. Liu, W. Lv, *Appl. Catal., B* **2019**, *244*, 974.
[159] X. Wang, Y. Ke, H. Pan, K. Ma, Q. Xiao, D. Yin, G. Wu, M. T. Swihart, *ACS Catal.* **2015**, *5*, 2534.
[160] N. Ghorai, H. N. Ghosh, *J. Phys. Chem. C* **2019**, *123*, 28401.
[161] P. Qiu, Y. Zhu, Y. Qin, X. Shi, L. Chen, *APL Mater.* **2016**, *4*.
[162] A. Cuevas, R. Romero, D. Leinen, E. A. Dalchiele, J. R. Ramos-Barrado, F. Martin, *Sol. Energy Mater. Sol. Cells* **2015**, *134*, 199.
[163] K. Itoh, T. Kuzuya, K. Sumiyama, *Mater. Trans.* **2006**, *47*, 1953.
[164] X. Jiang, Y. Xie, J. Lu, W. He, L. Zhu, Y. Qian, *J. Mater. Chem.* **2000**, *10*, 2193.
[165] Y. Xie, A. Riedinger, M. Prato, A. Casu, A. Genovese, P. Guardia, S. Sottini, C. Sangregorio, K. Miszta, S. Ghosh, *J. Am. Chem. Soc.* **2013**, *135*, 17630.
[166] Y. Wang, F. Liu, Y. Ji, M. Yang, W. Liu, W. Wang, Q. Sun, Z. Zhang, X. Zhao, X. Liu, *Dalton Trans.* **2015**, *44*, 10431.
[167] Y. Wang, Y. Hu, Q. Zhang, J. Ge, Z. Lu, Y. Hou, Y. Yin, *Inorg. Chem.* **2010**, *49*, 6601.
[168] W. van der Stam, Q. A. Akkerman, X. Ke, M. A. van Huis, S. Bals, C. de Mello Donega, *Chem. Mater.* **2015**, *27*, 283.
[169] D. Zhou, D. Liu, W. Xu, Z. Yin, X. Chen, P. Zhou, S. Cui, Z. Chen, H. Song, *ACS Nano* **2016**, *10*, 5169.
[170] B. Zhao, X. Long, Q. Zhao, M. Shakouri, R. Feng, L. Lin, Y. Zeng, Y. Zhang, X.-Z. Fu, J.-L. Luo, *Mater. Today Nano* **2023**, *23*, 100362.
[171] M. Mousavi-Kamazani, Z. Zarghami, M. Salavati-Niasari, *J. Phys. Chem. C* **2016**, *120*, 2096.
[172] M. R. Kim, H. A. Hafez, X. Chai, L. V. Besteiro, L. Tan, T. Ozaki, A. O. Govorov, R. Izquierdo, D. Ma, *Nanoscale* **2016**, *8*, 12946.
[173] X. Yu, X. An, *Mater. Lett.* **2010**, *64*, 252.
[174] L. Chen, Y.-B. Chen, L.-M. Wu, *J. Am. Chem. Soc.* **2004**, *126*, 16334.
[175] S. Jeong, Y. Kim, *J. Ind. Eng. Chem.* **2024**, *137*, 491.
[176] S. Wang, S. Yang, *Chem. Mater.* **2001**, *13*, 4794.
[177] C. Wu, J.-B. Shi, C.-J. Chen, Y.-C. Chen, Y.-T. Lin, P.-F. Wu, S.-Y. Wei, *Mater. Lett.* **2008**, *62*, 1074.
[178] T.-Y. Ding, M.-S. Wang, S.-P. Guo, G.-C. Guo, J.-S. Huang, *Mater. Lett.* **2008**, *62*, 4529.
[179] L. Zhao, L. Zhou, C. Sun, Y. Gu, W. Wen, X. Fang, *CrystEngComm* **2018**, *20*, 6529.
[180] M. Venkata-Haritha, C. V. V. M. Gopi, Y.-S. Lee, H.-J. Kim, *RSC Adv.* **2016**, *6*, 101185.
[181] W. van der Stam, S. Gradmann, T. Altantzis, X. Ke, M. Baldus, S. Bals, C. de Mello Donega, *Chem. Mater.* **2016**, *28*, 6705.
[182] Y. Liu, D. Yin, M. T. Swihart, *Chem. Mater.* **2018**, *30*, 1399.
[183] D. Pan, L. An, Z. Sun, W. Hou, Y. Yang, Z. Yang, Y. Lu, *J. Am. Chem. Soc.* **2008**, *130*, 5620.
[184] N. Chumha, W. Pudkon, A. Chachvalvutikul, T. Luangwanta, C. Randorn, B. Inceesungvorn, A. Ngamjarurojana, S. Kaowphong, *Mater. Res. Express* **2020**, *7*, 015074.
[185] L. Zheng, Y. Xu, Y. Song, C. Wu, M. Zhang, Y. Xie, *Inorg. Chem.* **2009**, *48*, 4003.
[186] M. Esmaeili-Zare, M. Behpour, *Int. J. Hydrogen Energy* **2020**, *45*, 16169.
[187] A. Barhoi, B. Mahto, H. Ali, S. Hussain, *J. Mater. Chem. A* **2025**.
[188] Q. A. Akkerman, A. Genovese, C. George, M. Prato, I. Moreels, A. Casu, S. Marras, A. Curcio, A. Scarpellini, T. Pellegrino, L. Manna, V. Lesnyak, *ACS Nano* **2015**, *9*, 521.
[189] Q. Luo, Y. Zeng, L. Chen, C. Ma, *Chem. Asian J.* **2014**, *9*, 2309.
[190] S. C. Riha, B. A. Parkinson, A. L. Prieto, *J. Am. Chem. Soc.* **2009**, *131*, 12054.

© 2025 The Author(s). Advanced Functional Materials published by Wiley-VCH GmbH

16163028, 0, Downloaded from https://advanced.onlinelibrary.wiley.com/doi/10.1002/adfm.202502901 by EMBRAPA - Empresa Brasileira de Pesquisa Agropecuaria, Wiley Online Library on [06/06/2025]. See the Terms and Conditions (https://onlinelibrary.wiley.com/terms-and-conditions) on Wiley Online Library for rules of use; OA articles are governed by the applicable Creative Commons License

[191] F. Ozel, E. Aslan, B. Istanbullu, O. Akay, I. H. Patir, *Appl. Catal., B* **2016**, *198*, 67.
[192] M. Wei, Q. Du, R. Wang, G. Jiang, W. Liu, C. Zhu, *Chem. Lett.* **2014**, *43*, 1149.
[193] M. Z. Ansari, M. Faraz, S. Munjal, V. Kumar, N. Khare, *Adv. Powder Technol.* **2017**, *28*, 2402.
[194] M. Burhanuz Zaman, R. A. Mir, R. Poolla, *Int. J. Hydrogen Energy* **2019**, *44*, 23023.
[195] G. K. Grandhi, N. S. M. Viswanath, H. B. Cho, J. H. Han, S. M. Kim, S. Choi, W. B. Im, *J. Phys. Chem. Lett.* **2020**, *11*, 7723.
[196] L. Xie, B. Chen, F. Zhang, Z. Zhao, X. Wang, L. Shi, Y. Liu, L. Huang, R. Liu, B. Zou, Y. Wang, *Photon. Res.* **2020**, *8*, 768.
[197] Z. Zhang, X. Wang, J. Qian, J. Xu, *J. Energy Chem.* **2024**, *92*, 521.
[198] L. Zheng, A. Nozariasbmarz, Y. Hou, J. Yoon, W. Li, Y. Zhang, H. Wu, D. Yang, T. Ye, M. Sanghadasa, K. Wang, B. Poudel, S. Priya, K. Wang, *Nat. Commun.* **2022**, *13*, 7399.
[199] W. Meng, C. Wang, G. Xu, G. Luo, Z. Deng, *Molecules* **2024**, *29*, 1162.
[200] T.-H. Le, S. Lee, H. Jo, M. Kim, J. Lee, M. Chang, H. Yoon, *ACS Appl. Nano Mater.* **2021**, *4*, 7621.
[201] P. Cheng, L. Sun, L. Feng, S. Yang, Y. Yang, D. Zheng, Y. Zhao, Y. Sang, R. Zhang, D. Wei, W. Deng, K. Han, *Angew. Chem. Int. Ed.* **2019**, *58*, 16087.
[202] F. Gao, X. Zhu, Q. Feng, W. Zhong, W. Liu, H. Xu, Y. Liu, *Nano Energy* **2022**, *98*, 107270.
[203] M. Aamir, M. Sher, M. A. Malik, N. Revaprasadu, J. Akhtar, *Mater. Lett.* **2016**, *183*, 135.
[204] Q. Yao, J. Li, X. Li, X. Zheng, Z. Wang, X. Tao, *Adv. Opt. Mater.* **2022**, *10*, 2201161.
[205] H.-B. Zhao, J.-F. Liao, Y. Teng, H.-Y. Chen, D.-B. Kuang, *ACS Appl. Mater. Interfaces* **2022**, *14*, 43354.
[206] S. Cheng, A. Beitlerova, R. Kucerkova, M. Nikl, G. Ren, Y. Wu, *Phys. Rapid Res.* **2020**, *14*, 2000374.
[207] S. C. Tang, Y. J. Li, J. Yang, T. Zhao, J. Tian, Y. J. Wang, Z. Y. Ji, Y. Li, Y. Dai, T. He, Y.-W. Zhang, A. V. Emeline, Q. Pang, D. W. Bahnemann, J. H. Pan, *ChemSusChem* **2025**, *18*, 202402094.
[208] T. Jun, K. Sim, S. Iimura, M. Sasase, H. Kamioka, J. Kim, H. Hosono, *Adv. Mater.* **2018**, *30*, 1804547.
[209] J. Sheng, Y. He, M. Huang, C. Yuan, S. Wang, F. Dong, *ACS Catal.* **2022**, *12*, 2915.
[210] J. Huang, M. Li, Z. Liu, J. Hua, H. Zeng, Y. Chen, J. Su, *CrystEngComm* **2023**, *25*, 6091.
[211] C. Schneider, D. Bodesheim, J. Keupp, R. Schmid, G. Kieslich, *Nat. Commun.* **2019**, *10*, 4921.
[212] S. Wang, S. S. Park, C. T. Buru, H. Lin, P.-C. Chen, E. W. Roth, O. K. Farha, C. A. Mirkin, *Nat. Commun.* **2020**, *11*, 2495.
[213] P. Valvekens, F. Vermoortele, D. De Vos, *Catal. Sci. Technol.* **2013**, *3*, 1435.
[214] A. E. Baumann, D. A. Burns, B. Liu, V. S. Thoi, *Commun. Chem.* **2019**, *2*, 86.
[215] X. Chen, K. Geng, R. Liu, K. T. Tan, Y. Gong, Z. Li, S. Tao, Q. Jiang, D. Jiang, *Angew. Chem., Int. Ed.* **2020**, *59*, 5050.
[216] R. Wei, C. A. Gaggioli, G. Li, T. Islamoglu, Z. Zhang, P. Yu, O. K. Farha, C. J. Cramer, L. Gagliardi, D. Yang, B. C. Gates, *Chem. Mater.* **2019**, *31*, 1655.
[217] S. Kandambeth, K. Dey, R. Banerjee, *J. Am. Chem. Soc.* **2019**, *141*, 1807.
[218] D. B. Shinde, L. Cao, A. D. Dinga Wonanke, X. Li, S. Kumar, X. Liu, M. N. Hedhili, A.-H. Emwas, M. Addicoat, K.-W. Huang, Z. Lai, *Chem. Sci.* **2020**, *11*, 5434.
[219] Z. Wang, S. Zhang, Y. Chen, Z. Zhang, S. Ma, *Chem. Soc. Rev.* **2020**, *49*, 708.
[220] Y. Tian, S.-Q. Xu, C. Qian, Z.-F. Pang, G.-F. Jiang, X. Zhao, *Chem. Commun.* **2016**, *52*, 11704.
[221] S. Navalón, A. Dhakshinamoorthy, M. Álvaro, B. Ferrer, H. García, *Chem. Rev.* **2023**, *123*, 445.
[222] S. Wang, X. Wang, *Small* **2015**, *11*, 3097.
[223] L. Yao, A. M. Pütz, H. Vignolo-González, B. V. Lotsch, *J. Am. Chem. Soc.* **2024**, *146*, 9479.
[224] B. Mishra, A. Alam, A. Chakraborty, B. Kumbhakar, S. Ghosh, P. Pachfule, A. Thomas, *Adv. Mater.* **2025**, *37*, 2413118.
[225] W. Tu, Y. Yang, C. Chen, T. Zhou, T. Li, H. Wang, S. Wu, Y. Zhou, D. O'Hare, Z. Zou, R. Xu, *Small Struct.* **2023**, *4*, 2200233.
[226] L. Zeng, X. Guo, C. He, C. Duan, *ACS Catal.* **2016**, *6*, 7935.
[227] R. Singh, G. Singh, N. George, G. Singh, S. Gupta, H. Singh, G. Kaur, J. Singh, *Catalysts* **2023**, *13*.
[228] D. Shi, C. He, B. Qi, C. Chen, J. Niu, C. Duan, *Chem. Sci.* **2015**, *6*, 1035.
[229] Q. Su, Q. Guo, H. Wang, M. Liu, C. Zuo, *Carbon Resources Conversion* **2024**, *7*, 100211.
[230] U. Nwosu, S. Siahrostami, *Catal. Sci. Technol.* **2023**, *13*, 3740.
[231] X. Deng, R. Li, S. Wu, L. Wang, J. Hu, J. Ma, W. Jiang, N. Zhang, X. Zheng, C. Gao, L. Wang, Q. Zhang, J. Zhu, Y. Xiong, *J. Am. Chem. Soc.* **2019**, *141*, 10924.
[232] J. Albo, D. Vallejo, G. Beobide, O. Castillo, P. Castaño, A. Irabien, *ChemSusChem* **2017**, *10*, 1100.
[233] L. Wang, P. Jin, J. Huang, H. She, Q. Wang, *ACS Sustainable Chem. Eng.* **2019**, *7*, 15660.
[234] X. Han, Y.-J. Chu, M. Dong, W. Chen, G. Ding, L.-L. Wen, K.-Z. Shao, Z. Su, M. Zhang, X. Wang, G.-G. Shan, *Inorg. Chem.* **2022**, *61*, 5869.
[235] W. Su, S. Zhong, Y. Fan, *Appl. Catal. B: Environ. Energy* **2024**, *354*, 124145.
[236] M. Dong, Q. Pan, F. Meng, X. Yao, S. You, G. Shan, C. Sun, X. Wang, Z. Su, *J. Colloid Interface Sci.* **2024**, *662*, 807.
[237] Q. Zhao, Y. Wang, M. Li, S. Zhu, T. Li, J. Yang, T. Lin, E. P. Delmo, Y. Wang, J. Jang, M. Gu, M. Shao, *SmartMat* **2022**, *3*, 183.
[238] R. López, R. Gómez, M. E. Llanos, *Catal. Today* **2009**, *148*, 103.
[239] X. YANG, S. WANG, H. SUN, X. WANG, J. LIAN, *Trans. Nonferrous Metals Soc. China* **2015**, *25*, 504.
[240] A. Tamarani, R. Zainul, I. Dewata, *J. Phys.: Conf. Ser.* **2019**, *1185*, 012020.
[241] X. Bokhimi, A. Morales, O. Novaro, T. López, O. Chimal, M. Asomoza, R. Gómez, *Chem. Mater.* **1997**, *9*, 2616.
[242] I.-H. Tseng, J. C. S. Wu, H.-Y. Chou, *J. Catal.* **2004**, *221*, 432.
[243] S. M. Reda, M. Khairy, M. A. Mousa, *Arabian J. Chem.* **2020**, *13*, 86.
[244] L. C.-K. Liau, J.-S. Huang, *J. Alloys Compd.* **2017**, *702*, 153.
[245] P. Jongnavakit, P. Amornpitoksuk, S. Suwanboon, N. Ndiege, *Appl. Surf. Sci.* **2012**, *258*, 8192.
[246] M. Fu, Y. Li, S. wu, P. Lu, J. Liu, F. Dong, *Appl. Surf. Sci.* **2011**, *258*, 1587.
[247] A. Goktas, F. Aslan, A. Tumbul, *J. Sol-Gel Sci. Technol.* **2015**, *75*, 45.
[248] M. Nikzad, M. R. Khanlary, S. Rafiee, *Appl. Phys. A* **2019**, *125*, 507.
[249] H. Lemziouka, L. E. H. Omari, R. Moubah, A. Boutahar, S. Bahhar, M. Abid, H. Lassri, *Mater. Today: Proc.* **2021**, *37*, 3940.
[250] A. Nihore, F. Aziz, N. Oswal, P. Jain, O. Subohi, N. Gupta, *Mater. Today: Proc.* **2019**, *18*, 3651.
[251] Y. Zhao, J. Shen, J. Yuan, H. Mao, X. Cheng, Z. Xu, Z. Bian, *Nano Energy* **2024**, *124*, 109499.
[252] D. Han, Y. Han, J. Li, X. Liu, K. W. K. Yeung, Y. Zheng, Z. Cui, X. Yang, Y. Liang, Z. Li, S. Zhu, X. Yuan, X. Feng, C. Yang, S. Wu, *Appl. Catal., B* **2020**, *261*, 118248.
[253] Z. Li, G. Zhu, W. Zhang, L. Zhu, B. Cao, J. Gao, X. Shi, Y. Huang, P. Liu, M. Hojamberdiev, *Chem. Eng. J.* **2023**, *452*, 139378.
[254] M. Mittal, M. Sharma, O. P. Pandey, *Sol. Energy* **2014**, *110*, 386.
[255] C. Karunakaran, G. Abiramasundari, P. Gomathisankar, G. Manikandan, V. Anandi, *J. Colloid Interface Sci.* **2010**, *352*, 68.

© 2025 The Author(s). Advanced Functional Materials published by Wiley-VCH GmbH

16163028, 0, Downloaded from https://advanced.onlinelibrary.wiley.com/doi/10.1002/adfm.202502901 by EMBRAPA - Empresa Brasileira de Pesquisa Agropecuaria, Wiley Online Library on [06/06/2025]. See the Terms and Conditions (https://onlinelibrary.wiley.com/terms-and-conditions) on Wiley Online Library for rules of use; OA articles are governed by the applicable Creative Commons License

[256] Y. Feng, D. Chen, M. Niu, Y. Zhong, Z. He, S. Ma, K. Yuan, H. Ding, K. Lv, L. Guo, W. Zhang, M. Ma, *Appl. Catal. B: Environ. Energy* **2025**, *365*, 124931.
[257] B. Roy, S. Mahato, S. Bose, A. Ghorai, S. K. Srivastava, N. C. Das, S. K. Ray, *Chem. Mater.* **2023**, *35*, 1601.
[258] M. Li, J. Xu, Y. Song, F. Chen, *CrystEngComm* **2022**, *24*, 7962.
[259] N. K. Tailor, S. Singh, N. Singh, P. K. Nayak, S. K. Saini, S. Das, G. Venkanna, S. P. Senanayak, M. Kumar, D. Ghosh, K. Tripathi, K. K. Pant, S. Satapathi, *Adv. Energy Mater.* **2024**, *14*, 2402087.
[260] L. Li, Z. Zhang, *Chem. Eng. J.* **2022**, *434*, 134811.
[261] Y. Wang, H. Wang, L. Guo, T. He, *J. Colloid Interface Sci.* **2023**, *648*, 889.
[262] T. Arai, S. Senda, Y. Sato, H. Takahashi, K. Shinoda, B. Jeyadevan, K. Tohji, *Chem. Mater.* **2008**, *20*, 1997.
[263] D. Li, Y. Zhao, Y. Miao, C. Zhou, L.-P. Zhang, L.-Z. Wu, T. Zhang, *Adv. Mater.* **2022**, *34*, 2207793.
[264] B.-H. Lee, S. Park, M. Kim, A. K. Sinha, S. C. Lee, E. Jung, W. J. Chang, K.-S. Lee, J. H. Kim, S.-P. Cho, H. Kim, K. T. Nam, T. Hyeon, *Nat. Mater.* **2019**, *18*, 620.
[265] F. Huang, F. Wang, Y. Liu, L. Guo, *Adv. Mater.* **2024**, *n/a*, 2416708.
[266] A. M. Abdel-Mageed, B. Rungtaweevoranit, M. Parlinska-Wojtan, X. Pei, O. M. Yaghi, R. J. Behm, *J. Am. Chem. Soc.* **2019**, *141*, 5201.
[267] G. Wang, C.-T. He, R. Huang, J. Mao, D. Wang, Y. Li, *J. Am. Chem. Soc.* **2020**, *142*, 19339.
[268] X. Xiao, Y. Gao, L. Zhang, J. Zhang, Q. Zhang, Q. Li, H. Bao, J. Zhou, S. Miao, N. Chen, J. Wang, B. Jiang, C. Tian, H. Fu, *Adv. Mater.* **2020**, *32*, 2003082.
[269] Y. Duan, Y. Wang, W. Zhang, J. Zhang, C. Ban, D. Yu, K. Zhou, J. Tang, X. Zhang, X. Han, L. Gan, X. Tao, X. Zhou, *Adv. Funct. Mater.* **2023**, *33*, 2301729.
[270] Y. Ma, Y. Zhang, Y. Ma, T. Lv, B. Xiao, X. Kuang, X. Deng, J. Zhang, J. Zhao, Q. Liu, *Nanoscale* **2022**, *14*, 15889.
[271] M. A. R. da Silva, J. C. Gil, N. V. Tarakina, G. T. S. T. Silva, J. B. G. Filho, K. Krambrock, M. Antonietti, C. Ribeiro, I. F. Teixeira, *Chem. Commun.* **2022**, *58*, 7419.
[272] B. Syal, P. Kumar, P. Gupta, *ACS Appl. Nano Mater* **2023**, *6*, 4987.
[273] X. Bai, X. Zhao, Y. Zhang, C. Ling, Y. Zhou, J. Wang, Y. Liu, *J. Am. Chem. Soc.* **2022**, *144*, 17140.
[274] Y. Zhang, S. Ye, M. Gao, Y. Li, X. Huang, J. Song, H. Cai, Q. Zhang, J. Zhang, *ACS Nano* **2022**, *16*, 1142.
[275] S. Das, W. M. A. Wan Daud, *RSC Adv.* **2014**, *4*, 20856.
[276] M. Muratori, H. Kheshgi, B. Mignone, L. Clarke, H. McJeon, J. Edmonds, *Int. J. Greenhouse Gas Control* **2017**, *57*, 34.
[277] S.-Y. Lee, J.-U. Lee, I.-B. Lee, J. Han, *Appl. Energy* **2017**, *189*, 725.
[278] F. Marpani, M. Pinelo, A. S. Meyer, *Biochem. Eng. J.* **2017**, *127*, 217.
[279] H. Ritchie, M. Roser, *CO_2 Emissions* **2020**.
[280] G. Centi, E. A. Quadrelli, S. Perathoner, *Energy Environ. Sci.* **2013**, *6*, 1711.
[281] D. Gielen, F. Boshell, D. Saygin, *Nat. Mater.* **2016**, *15*, 117.
[282] W. Zheng, X. Yang, Z. Li, B. Yang, Q. Zhang, L. Lei, Y. Hou, *Angew. Chem., Int. Ed.* **2023**, *62*, 202307283.
[283] N. Theaker, J. M. Strain, B. Kumar, J. P. Brian, S. Kumari, J. M. Spurgeon, *Electrochim. Acta* **2018**, *274*, 1.
[284] Q. Shi, B. Zhang, Z. Wu, D. Yang, H. Wu, J. Shi, Z. Jiang, *ChemSusChem* **2025**, *18*, 202401916.
[285] C. A. Huff, M. S. Sanford, *J. Am. Chem. Soc.* **2011**, *133*, 18122.
[286] J. Li, Y. Chen, B. Yao, W. Yang, X. Cui, H. Liu, S. Dai, S. Xi, Z. Sun, W. Chen, Y. Qin, J. Wang, Q. He, C. Ling, D. Wang, Z. Zhang, *J. Am. Chem. Soc.* **2024**, *146*, 5693.
[287] W. A. Thompson, E. Sanchez Fernandez, M. M. Maroto-Valer, *ACS Sustainable Chem. Eng.* **2020**, *8*, 4677.
[288] Y. Ji, Y. Luo, *J. Am. Chem. Soc.* **2016**, *138*, 15896.
[289] S. C. Markham, *J. Chem. Educ.* **1955**, *32*, 540.
[290] A. Fujishima, K. Honda, *Nature* **1972**, *238*, 37.
[291] J. C. De Almeida, M. T. Corrêa, R. H. Koga, D. M. S. Del Duque, O. F. Lopes, G. T. S. T. Da Silva, C. Ribeiro, V. R. De Mendonça, *New J. Chem.* **2020**, *44*, 18216.
[292] F. C. Soares, J. C. De Almeida, R. H. Koga, D. M. D. S. Del Duque, G. T. S. T. Da Silva, C. Ribeiro, V. R. De Mendonça, *Mater. Chem. Phys.* **2022**, *290*, 126588.
[293] A. H. Navidpour, M. B. Ahmed, J. L. Zhou, *Nanomaterials* **2024**, *14*, 135.
[294] F. Quddus, A. Shah, F. J. Iftikhar, N. S. Shah, A. Haleem, *Catalysts* **2023**, *13*, 511.
[295] K. Bano, S. Kaushal, P. P. Singh, *Polyhedron* **2021**, *209*, 115465.
[296] O. F. Lopes, E. C. Paris, C. Ribeiro, *Appl. Catal., B* **2014**, *144*, 800.
[297] H. Charles, R. C. Pawar, H. Khan, C. S. Lee, *Int. J. Precis. Eng. Manuf.-Green Tech.* **2023**, *10*, 1061.
[298] T. Inoue, A. Fujishima, S. Konishi, K. Honda, *Nature* **1979**, *277*, 637.
[299] X. Chang, T. Wang, J. Gong, *Energy Environ. Sci.* **2016**, *9*, 2177.
[300] T. Li, H. Huang, S. Wang, Y. Mi, Y. Zhang, *Nano Res.* **2023**, *16*, 8542.
[301] C. Wang, J. Xu, Z. Zhou, *Energies* **2022**, *15*, 8117.
[302] L. Zhao, J. Wang, W. Yang, H. Hou, R. Yan, *Environ. Chem. Lett.* **2023**, *21*, 1499.
[303] X. Chen, S. Shen, L. Guo, S. S. Mao, *Chem. Rev.* **2010**, *110*, 6503.
[304] M. Gattrell, N. Gupta, A. Co, *J. Electroanal. Chem.* **2006**, *594*, 1.
[305] M. R. Hoffmann, S. T. Martin, W. Choi, D. W. Bahnemann, *Chem. Rev.* **1995**, *95*, 69.
[306] G. Silva, O. Lopes, E. Dias, J. Torres, A. Nogueira, L. Faustino, F. Prado, A. Patrocínio, C. Ribeiro, *Quím. Nova* **2021**.
[307] C. Huang, B. Song, P. Wang, L. Zhang, *Colloids Surf. A* **2023**, *656*, 130396.
[308] A. H. Pinto, A. E. Nogueira, C. J. Dalmaschio, I. N. Frigini, J. C. De Almeida, M. M. Ferrer, O. M. Berengue, R. A. Gonçalves, V. R. De Mendonça, *Solids* **2022**, *3*, 327.
[309] Y. Wang, J. A. Torres, M. Shviro, M. Carmo, T. He, C. Ribeiro, *Prog. Mater. Sci.* **2022**, *130*, 100965.
[310] M. Reli, P. Nadrah, M. Filip Edelmannová, R. Ricka, A. Sever Škapin, U. Lavrenčič Štangar, K. Kočí, *Mater. Sci. Semicond. Process.* **2024**, *169*, 107927.
[311] J. Fu, B. Zhu, C. Jiang, B. Cheng, W. You, J. Yu, *Small* **2017**, *13*, 1603938.
[312] H. Han, T. Han, Y. Luo, M. A. Mushtaq, Y. Jia, C. Liu, *J. Ind. Eng. Chem.* **2023**, *128*, 81.
[313] K. Yang, Z. Yang, C. Zhang, Y. Gu, J. Wei, Z. Li, C. Ma, X. Yang, K. Song, Y. Li, Q. Fang, J. Zhou, *Chem. Eng. J.* **2021**, *418*, 129344.
[314] A. W. Morawski, M. Gano, K. Ćmielewska, E. Kusiak-Nejman, I. Pełech, P. Staciwa, E. Ekiert, U. Narkiewicz, *Catalysts* **2023**, *13*, 1270.
[315] W. Shi, X. Guo, C. Cui, K. Jiang, Z. Li, L. Qu, J.-C. Wang, *Appl. Catal., B* **2019**, *243*, 236.
[316] W. Cai, Z. Qian, C. Hu, W. Zheng, L. Luo, Y. Zhao, *Chem. Eng. J.* **2024**, *479*, 147718.
[317] R. A. Geioushy, S. M. El-Sheikh, I. M. Hegazy, A. Shawky, S. El-Sherbiny, A.-H. T. Kandil, *Mater. Res. Bull.* **2019**, *118*, 110499.
[318] G. T. S. T. Da Silva, A. E. Nogueira, J. A. Oliveira, J. A. Torres, O. F. Lopes, C. Ribeiro, *Appl. Catal., B* **2019**, *242*, 349.
[319] A. D. Handoko, J. Tang, *Int. J. Hydrogen Energy* **2013**, *38*, 13017.
[320] S. Yao, B.-Q. Sun, P. Zhang, Z.-Y. Tian, H.-Q. Yin, Z.-M. Zhang, *Appl. Catal., B* **2022**, *317*, 121702.
[321] Y. Bessekhouad, D. Robert, J.-V. Weber, *Catal. Today* **2005**, *101*, 315.
[322] A. Gedamu Tamirat, J. Rick, A. Aregahegn Dubale, W.-N. Su, B.-J. Hwang, *Nanoscale Horiz.* **2016**, *1*, 243.
[323] S. N. Habisreutinger, L. Schmidt-Mende, J. K. Stolarczyk, *Angew. Chem., Int. Ed.* **2013**, *52*, 7372.
[324] P. D. Tran, L. H. Wong, J. Barber, J. S. C. Loo, *Energy Environ. Sci.* **2012**, *5*, 5902.
[325] J. Hao, B. Qi, J. Wei, D. Li, F. Zeng, *Fuel* **2021**, *287*, 119439.

© 2025 The Author(s). Advanced Functional Materials published by Wiley-VCH GmbH

16163028, 0, Downloaded from https://advanced.onlinelibrary.wiley.com/doi/10.1002/adfm.202502901 by EMBRAPA - Empresa Brasileira de Pesquisa Agropecuaria, Wiley Online Library on [06/06/2025]. See the Terms and Conditions (https://onlinelibrary.wiley.com/terms-and-conditions) on Wiley Online Library for rules of use; OA articles are governed by the applicable Creative Commons License

[326] A. E. Nogueira, G. T. S. T. Silva, J. A. Oliveira, O. F. Lopes, J. A. Torres, M. Carmo, C. Ribeiro, *ACS Appl. Energy Mater.* **2020**, *3*, 7629.
[327] L. Li, C. Guo, T. Li, C. Yang, F. Chen, W. Wang, R. Yan, J. Ning, Y. Hu, *Appl. Surf. Sci.* **2024**, *651*, 159220.
[328] F. Fang, Y. Liu, X. Sun, C. Fu, Y. Prakash Bhoi, W. Xiong, W. Huang, *Appl. Surf. Sci.* **2021**, *564*, 150407.
[329] J. Liu, M. Liu, X. Yang, H. Chen, S. F. Liu, J. Yan, *ACS Sustainable Chem. Eng.* **2020**, *8*, 6055.
[330] G. Yang, J. Xiong, M. Lu, W. Wang, W. Li, Z. Wen, S. Li, W. Li, R. Chen, G. Cheng, *J. Colloid Interface Sci.* **2022**, *624*, 348.
[331] J. Xiong, M. Zhang, M. Lu, K. Zhao, C. Han, G. Cheng, Z. Wen, *Chin. Chem. Lett.* **2022**, *33*, 1313.
[332] H. Ge, B. Zhang, H. Liang, M. Zhang, K. Fang, Y. Chen, Y. Qin, *Appl. Catal., B* **2020**, *263*, 118133.
[333] X. Zhang, Y. L. Chen, R.-S. Liu, D. P. Tsai, *Rep. Prog. Phys.* **2013**, *76*, 046401.
[334] H. Lai, W. Xiao, Y. Wang, T. Song, B. Long, S. Yin, A. Ali, G.-J. Deng, *Chem. Eng. J.* **2021**, *417*, 129295.
[335] X. He, M. Liu, Z. Liang, Z. Wang, P. Wang, Y. Liu, H. Cheng, Y. Dai, Z. Zheng, B. Huang, *J. Solid State Chem.* **2021**, *298*, 122113.
[336] H. Zhao, J. Huang, Q. Qin, H. Chen, D. Kuang, *Small* **2023**, *19*, 2302022.
[337] F. Xue, X. Lai, Y. Xu, *ChemCatChem* **2024**, *16*, 202400590.
[338] H. Xie, T. Wang, J. Liang, Q. Li, S. Sun, *Nano Today* **2018**, *21*, 41.
[339] A. Vasileff, C. Xu, Y. Jiao, Y. Zheng, S.-Z. Qiao, *Chem* **2018**, *4*, 1809.
[340] D. Tian, Z. Wang, Z. Xu, Y. Zhu, Y. Yan, J. Yang, S. He, Z. Xue, Z. Wang, K. Li, W. Fan, M. Xue, Z. Qu, W. Xia, M. Liu, *Adv. Compos. Hybrid Mater.* **2025**, *8*, 49.
[341] J. C. de Almeida, O. F. Lopes, M. Shviro, G. T. S. T. Da Silva, C. Ribeiro, V. R. De Mendonça, *Nanoscale* **2024**, *16*, 18455.
[342] G. Zhang, Z.-J. Zhao, D. Cheng, H. Li, J. Yu, Q. Wang, H. Gao, J. Guo, H. Wang, G. A. Ozin, T. Wang, J. Gong, *Nat. Commun.* **2021**, *12*, 5745.
[343] J. Jiao, X. Kang, J. Yang, S. Jia, Y. Peng, S. Liu, C. Chen, X. Xing, M. He, H. Wu, B. Han, *J. Am. Chem. Soc.* **2024**, *146*, 15917.
[344] W. Liu, P. Zhai, A. Li, B. Wei, K. Si, Y. Wei, X. Wang, G. Zhu, Q. Chen, X. Gu, R. Zhang, W. Zhou, Y. Gong, *Nat. Commun.* **2022**, *13*, 1877.
[345] P.-P. Yang, X.-L. Zhang, P. Liu, D. J. Kelly, Z.-Z. Niu, Y. Kong, L. Shi, Y.-R. Zheng, M.-H. Fan, H.-J. Wang, M.-R. Gao, *J. Am. Chem. Soc.* **2023**, *145*, 8714.
[346] Y. Wang, P. Han, X. Lv, L. Zhang, G. Zheng, *Joule* **2018**, *2*, 2551.
[347] Z. Gu, N. Yang, P. Han, M. Kuang, B. Mei, Z. Jiang, J. Zhong, L. Li, G. Zheng, *Small Methods* **2019**, *3*, 1800449.
[348] Z. Ni, H. Liang, Z. Yi, R. Guo, C. Liu, Y. Liu, H. Sun, X. Liu, *Coord. Chem. Rev.* **2021**, *441*, 213983.
[349] R. Chen, X. Zu, J. Zhu, Y. Zhao, Y. Li, Z. Hu, S. Wang, M. Fan, S. Zhu, H. Zhang, B. Ye, Y. Sun, Y. Xie, *Adv. Mater.* **2024**, *36*, 2314209.
[350] Y. Cai, J. Fu, Y. Zhou, Y.-C. Chang, Q. Min, J.-J. Zhu, Y. Lin, W. Zhu, *Nat. Commun.* **2021**, *12*, 586.
[351] B. Kim, Y. C. Tan, Y. Ryu, K. Jang, H. G. Abbas, T. Kang, H. Choi, K.-S. Lee, S. Park, W. Kim, P.-P. Choi, S. Ringe, J. Oh, *ACS Energy Lett.* **2023**, *8*, 3356.
[352] T. Zheng, C. Liu, C. Guo, M. Zhang, X. Li, Q. Jiang, W. Xue, H. Li, A. Li, C.-W. Pao, J. Xiao, C. Xia, J. Zeng, *Nat. Nanotechnol.* **2021**, *16*, 1386.
[353] X. Jiang, X. Li, Y. Kong, C. Deng, X. Li, Q. Hu, H. Yang, C. He, *Small* **2022**, *18*, 2204148.
[354] Y. Zhu, X. Cui, H. Liu, Z. Guo, Y. Dang, Z. Fan, Z. Zhang, W. Hu, *Nano Res.* **2021**, *14*, 4471.
[355] T. Yan, P. Wang, W.-Y. Sun, *Small* **2023**, *19*, 2206070.
[356] S. Chen, X. Zheng, P. Zhu, Y. Li, Z. Zhuang, H. Wu, J. Zhu, C. Xiao, M. Chen, P. Wang, D. Wang, Y.-L. He, *Angew. Chem., Int. Ed.* **2024**, *63*, 202411591.
[357] S. Popović, M. Smiljanić, P. Jovanovič, J. Vavra, R. Buonsanti, N. Hodnik, *Angew. Chem.* **2020**, *132*, 14844.
[358] H. Li, T. Liu, P. Wei, L. Lin, D. Gao, G. Wang, X. Bao, *Angew. Chem., Int. Ed.* **2021**, *60*, 14329.
[359] P. Chen, Y. Zhang, Y. Zhou, F. Dong, *Nano Mater. Sci.* **2021**, *3*, 344.
[360] Y. Zhang, S. Zhou, K. Sun, *Nanomaterials* **2023**, *13*.
[361] J. F. de Brito, A. R. Araujo, K. Rajeshwar, M. V. B. Zanoni, *Chem. Eng. J.* **2015**, *264*, 302.
[362] W. Zhou, H. Yang, N. Gao, D. Zhang, Z. Li, F. Gao, C. Nan, *J. Alloys Compd.* **2022**, *903*, 163707.
[363] D. Zhang, H. Yang, Y. Li, Z. Li, N. Gao, W. Zhou, Z. Liang, *Int. J. Electrochem. Sci.* **2021**, *16*, 150951.
[364] K. Wang, Y. Liu, Q. Wang, Y. Zhang, X. Yang, L. Chen, M. Liu, X. Qiu, J. Li, W. Li, *Appl. Catal., B* **2022**, *316*, 121616.
[365] B. Wang, F. Yang, Y. Dong, Y. Cao, J. Wang, B. Yang, Y. Wei, W. Wan, J. Chen, H. Jing, *Chem. Eng. J.* **2020**, *396*, 125255.
[366] D. Barreca, P. Fornasiero, A. Gasparotto, V. Gombac, C. Maccato, T. Montini, E. Tondello, *ChemSusChem* **2009**, *2*, 230.
[367] Y.-H. Zhang, B.-B. Jiu, F.-L. Gong, J.-L. Chen, H.-L. Zhang, *J. Alloys Compd.* **2017**, *729*, 563.
[368] F. Naaz, A. Sharma, M. Shahazad, T. Ahmad, *ChemistrySelect* **2022**, *7*, 202201800.
[369] M. Mondal, S. Maity, A. Ghosh, S. Ghosh, S. Bhattacharya, *Energy Nexus* **2024**, *14*.
[370] S. Saadi, A. Bouguelia, M. Trari, *Sol. Energy* **2006**, *80*, 272.
[371] N. Koriche, A. Bouguelia, A. Aider, M. Trari, *Int. J. Hydrogen Energy* **2005**, *30*, 693.
[372] M. Younsi, A. Aider, A. Bouguelia, M. Trari, *Sol. Energy* **2005**, *78*, 574.
[373] S. Li, H. Shao, K. Ding, M. Yao, M. Dou, Y. Cheng, K. Zhang, N. Yang, Y. Ma, Y. Chen, *ACS Appl. Nano Mater.* **2023**, *6*, 21853.
[374] N. Ali, T. T. Tsega, Y. Cao, S. Abbas, W. Li, A. Iqbal, H. Fazal, Z. Xin, J. Zai, X. Qian, *Nano Res.* **2021**, *14*, 3358.
[375] Y. Li, C. Zhuang, S. Qiu, J. Gao, Q. Zhou, Z. Sun, Z. Kang, X. Han, *Appl. Catal., B* **2023**, *337*, 122881.
[376] M. Li, S. Xu, L. Wu, H. Tang, B. Zhou, J. Xu, Q. Yang, T. Zhou, Y. Qiu, G. Chen, G. I. N. Waterhouse, K. Yan, *ACS Energy Lett.* **2022**, *7*, 3370.
[377] G. Chen, P. Wang, Y. Wu, Q. Zhang, Q. Wu, Z. Wang, Z. Zheng, Y. Liu, Y. Dai, B. Huang, *Adv. Mater.* **2020**, *32*, 2001344.
[378] D. Shi, R. Zheng, M.-J. Sun, X. Cao, C.-X. Sun, C.-J. Cui, C.-S. Liu, J. Zhao, M. Du, *Angew. Chem., Int. Ed.* **2017**, *56*, 14637.
[379] J. Zhao, Y. Wang, J. Zhou, P. Qi, S. Li, K. Zhang, X. Feng, B. Wang, C. Hu, *J. Mater. Chem. A* **2016**, *4*, 7174.
[380] C. Tan, H. Zhang, *Chem. Soc. Rev.* **2015**, *44*, 2713.
[381] X. Wang, J. Wang, X. Zhang, Q. Tian, M. Liu, N. Cai, Y. Xue, W. Chen, W. Li, F. Yu, *ChemCatChem* **2019**, *11*, 1354.
[382] D. Yoon, J. Lee, B. Seo, B. Kim, H. Baik, S. H. Joo, K. Lee, *Small* **2017**, *13*, 1700052.
[383] K. S. Bhat, H. S. Nagaraja, *J. Sci.: Adv. Mater. Devices* **2020**, *5*, 361.
[384] I. Daskalakis, I. Vamvasakis, I. T. Papadas, S. Tsatsos, S. A. Choulis, S. Kennou, G. S. Armatas, *Inorg. Chem. Front.* **2020**, *7*, 4687.
[385] L. Na, M. Shuhong, Y. Wenjun, Z. Jing, *J. Fuel Chem. Technol.* **2024**, *52*, 698.
[386] N. Li, W. Yan, Y. Niu, S. Qu, P. Zuo, H. Bai, N. Zhao, *ACS Appl. Mater. Interfaces* **2021**, *13*, 9838.
[387] L. Ren, L. Tong, X. Yi, W. Zhou, D. Wang, L. Liu, J. Ye, *Chem. Eng. J.* **2020**, *390*, 124558.
[388] X. Li, B. Liu, Y. Chen, X. Fan, Y. Li, F. Zhang, G. Zhang, W. Peng, *Nanotechnology* **2018**, *29*, 505603.
[389] H. V. Le, T. T. D. Ung, P. D. Tran, H. V. Mai, B. D. Do, L. Q. Nguyen, *J. Phys. D: Appl. Phys.* **2023**, *56*, 465502.
[390] M. B. Akbar, Y. Gong, Y. Wang, A. R. Woldu, X. Zhang, T. He, *Nanotechnology* **2021**, *32*, 395707.
[391] G. Sharma, Z. Zhao, P. Sarker, B. A. Nail, J. Wang, M. N. Huda, F. E. Osterloh, *J. Mater. Chem. A* **2016**, *4*, 2936.

© 2025 The Author(s). Advanced Functional Materials published by Wiley-VCH GmbH

16163028, 0, Downloaded from https://advanced.onlinelibrary.wiley.com/doi/10.1002/adfm.202502901 by EMBRAPA - Empresa Brasileira de Pesquisa Agropecuaria, Wiley Online Library on [06/06/2025]. See the Terms and Conditions (https://onlinelibrary.wiley.com/terms-and-conditions) on Wiley Online Library for rules of use; OA articles are governed by the applicable Creative Commons License

[392] S. Sekar, S. Sadhasivam, E. K. Nangai, S. Saravanan, D. Y. Kim, S. Lee, *Int. J. Energy Res.* **2023**, *2023*, 5038466.
[393] Q. Zhang, B. Zhai, Z. Lin, X. Zhao, P. Diao, *J. Phys. Chem. C* **2021**, *125*, 1890.
[394] K. Lalitha, G. Sadanandam, V. D. Kumari, M. Subrahmanyam, B. Sreedhar, N. Y. Hebalkar, *J. Phys. Chem. C* **2010**, *114*, 22181.
[395] L. Sinatra, A. P. LaGrow, W. Peng, A. R. Kirmani, A. Amassian, H. Idriss, O. M. Bakr, *J. Catal.* **2015**, *322*, 109.
[396] S. Xu, D. D. Sun, *Int. J. Hydrogen Energy* **2009**, *34*, 6096.
[397] J. Yu, Y. Hai, M. Jaroniec, *J. Colloid Interface Sci.* **2011**, *357*, 223.
[398] V. Navakoteswara Rao, N. Lakshmana Reddy, M. Mamatha Kumari, P. Ravi, M. Sathish, K. M. Kuruvilla, V. Preethi, K. R. Reddy, N. P. Shetti, T. M. Aminabhavi, M. V. Shankar, *Appl. Catal., B* **2019**, *254*, 174.
[399] M. Chandra, K. Bhunia, D. Pradhan, *Inorg. Chem.* **2018**, *57*, 4524.
[400] J. Liu, X. Sun, Y. Fan, Y. Yu, Q. Li, J. Zhou, H. Gu, K. Shi, B. Jiang, *Small* **2024**, *20*, 2306344.
[401] M. Inada, S. Yase, A. Tada, T. Yamane, Y. Miyaji, M. Hirahara, Y. Harada, S. Fujii, T. Fukushima, S. Dohshi, S. Higashimoto, *Mater. Today Catal.* **2024**, *7*, 100080.
[402] C. Ji, S.-N. Yin, S. Sun, S. Yang, *Appl. Surf. Sci.* **2018**, *434*, 1224.
[403] P. Karthik, T. R. Naveen Kumar, B. Neppolian, *Int. J. Hydrogen Energy* **2020**, *45*, 7541.
[404] Y.-H. Zhang, X.-L. Cai, Y.-L. Li, M.-M. Liu, C.-L. Ding, J.-L. Chen, S.-M. Fang, *Chem. Phys. Lett.* **2019**, *734*, 136748.
[405] Y. Lou, Y. Zhang, L. Cheng, J. Chen, Y. Zhao, *ChemSusChem* **2018**, *11*, 1505.
[406] C.-C. Hu, J.-N. Nian, H. Teng, *Sol. Energy Mater. Sol. Cells* **2008**, *92*, 1071.
[407] X.-J. Zheng, Y.-J. Wei, L.-F. Wei, B. Xie, M.-B. Wei, *Int. J. Hydrogen Energy* **2010**, *35*, 11709.
[408] J. Zhang, W. Li, Y. Li, L. Zhong, C. Xu, *Appl. Catal., B* **2017**, *217*, 30.
[409] Z. Li, H. Li, S. Wang, F. Yang, W. Zhou, *Chem. Eng. J.* **2022**, *427*, 131830.
[410] J. Zhang, J. Yu, Y. Zhang, Q. Li, J. R. Gong, *Nano Lett.* **2011**, *11*, 4774.
[411] L. J. Zhang, T. F. Xie, D. J. Wang, S. Li, L. L. Wang, L. P. Chen, Y. C. Lu, *Int. J. Hydrogen Energy* **2013**, *38*, 11811.
[412] F. Zhang, H.-Q. Zhuang, W. Zhang, J. Yin, F.-H. Cao, Y.-X. Pan, *Catal. Today* **2019**, *330*, 203.
[413] F. Cheng, H. Yin, Q. Xiang, *Appl. Surf. Sci.* **2017**, *391*, 432.
[414] A. Derbal, S. Omeiri, A. Bouguelia, M. Trari, *Int. J. Hydrogen Energy* **2008**, *33*, 4274.
[415] Z. Guan, J. Pan, Q. Li, G. Li, J. Yang, *ACS Sustainable Chem. Eng.* **2019**, *7*, 7736.
[416] B. Yang, F. Jin, X. Pan, X. Jin, Z. Jin, *ACS Appl. Mater. Interfaces* **2024**, *16*, 36333.
[417] Y. Liu, H. Tan, Y. Wei, M. Liu, J. Hong, W. Gao, S. Zhao, S. Zhang, S. Guo, *ACS Nano* **2023**, *17*, 5994.
[418] S. Xiao, P. Liu, W. Zhu, G. Li, D. Zhang, H. Li, *Nano Lett.* **2015**, *15*, 4853.
[419] R. Song, M. Liu, B. Luo, J. Geng, D. Jing, *AIChE J.* **2020**, *66*, 17008.
[420] T. Huang, Z. Xu, G. Zeng, P. Zhang, T. Song, Y. Wang, T. Wang, S. Huang, T. Wang, H. Zeng, *Carbon* **2019**, *143*, 257.
[421] D. Zhan, J. Tian, Q. Fu, P. Liu, Y. Zhao, W. Liu, D. Li, Y. Huang, C. Han, *Appl. Surf. Sci.* **2023**, *641*, 158463.
[422] Y. Zhu, A. Marianov, H. Xu, C. Lang, Y. Jiang, *ACS Appl. Mater. Interfaces* **2018**, *10*, 9468.
[423] J. Li, Y. Huang, B. Luo, L. Ma, D. Jing, *J. Colloid Interface Sci.* **2022**, *626*, 975.
[424] S. Ghosh, S. R. Keshri, S. Bera, R. N. Basu, *Int. J. Hydrogen Energy* **2020**, *45*, 6159.
[425] S. Ahmad, S. B. Khan, A. M. Asiri, *Int. J. Hydrogen Energy* **2023**, *48*, 6399.
[426] Y. Yamada, S. Shikano, T. Akita, S. Fukuzumi, *Catal. Sci. Technol.* **2015**, *5*, 979.
[427] Z. Xi, C. Li, L. Zhang, M. Xing, J. Zhang, *Int. J. Hydrogen Energy* **2014**, *39*, 6345.
[428] M. Esmat, E. Doustkhah, M. Abdelbar, R. Tahawy, H. El-Hosainy, M. Abdelhameed, Y. Ide, N. Fukata, *ACS Sustainable Chem. Eng.* **2022**, *10*, 4143.
[429] N. Liu, J. Jiang, Z. Chen, B. Wu, S. Zhang, Y.-Q. Zhang, P. Cheng, W. Shi, *Angew. Chem., Int. Ed.* **2023**, *62*, 202312306.
[430] W. Han, L.-H. Shao, X.-J. Sun, Y.-H. Liu, F.-M. Zhang, Y. Wang, P.-Y. Dong, G.-L. Zhang, *Appl. Catal., B* **2022**, *317*, 121710.
[431] J. Shen, C. Luo, S. Qiao, Y. Chen, Y. Tang, J. Xu, K. Fu, D. Yuan, H. Tang, H. Zhang, C. Liu, *ACS Catal.* **2023**, *13*, 6280.
[432] Y. Zhang, J. Zhao, H. Wang, B. Xiao, W. Zhang, X. Zhao, T. Lv, M. Thangamuthu, J. Zhang, Y. Guo, J. Ma, L. Lin, J. Tang, R. Huang, Q. Liu, *Nat. Commun.* **2022**, *13*, 58.
[433] Y. Fu, K. Lu, A. Hu, J. Huang, L. Guo, J. Zhou, J. Zhao, O. V. Prezhdo, M. Liu, *J. Am. Chem. Soc.* **2023**, *145*, 28166.
[434] M. Ghosh, R. Ezhov, S. E. Braley, Y. Losovyj, G. Bury, Y. N. Pushkar, J. M. Smith, *ACS Appl. Energy Mater.* **2024**, *7*, 6717.
[435] R. Ma, G. Lin, Y. Zhou, Q. Liu, T. Zhang, G. Shan, M. Yang, J. Wang, *npj Comput. Mater.* **2019**, *5*, 78.
[436] M. K. Debe, *Nature* **2012**, *486*, 43.
[437] Q. Li, P. Xu, B. Zhang, H. Tsai, S. Zheng, G. Wu, H.-L. Wang, *J. Phys. Chem. C* **2013**, *117*, 13872.
[438] J. Liu, J. Xie, R. Wang, B. Liu, X. Meng, X. Xu, B. Tang, Z. Cai, J. Zou, *Chem. Eng. J.* **2022**, *450*, 137961.
[439] C.-C. Chang, J.-C. Kao, Y.-C. Lo, J.-P. Chou, S.-C. Lin, C.-C. Wen, M. H. Huang, *J. Mater. Chem. A* **2025**.
[440] J. Li, C. Dang, Q. Zhu, L. Li, W. Zhang, *Acta Mater.* **2025**, *287*, 120781.
[441] F. Fouda-Onana, S. Bah, O. Savadogo, *J. Electroanal. Chem.* **2009**, *636*, 1.
[442] Z. Yang, K. Jiang, G. Tong, C. Ke, H. Wu, P. Liu, J. Zhang, H. Ji, J. Zhu, C. Lu, X. Zhuang, *Chem. Eng. J.* **2022**, *437*, 135377.
[443] T. Zhang, X. Niu, Q. Chen, J. Wang, *J. Phys. Chem. Lett.* **2025**, *16*, 675.
[444] J. M. Campos-Martin, G. Blanco-Brieva, J. L. G. Fierro, *Angew. Chem., Int. Ed.* **2006**, *45*, 6962.
[445] S. V. Venkatesan, A. H. B. Mostaghimi, V. Thangadurai, S. Siahrostami, *Electrochem. Sci. Adv* **2023**, *3*, 2100140.
[446] Z. Deng, L. Li, Y. Ren, C. Ma, J. Liang, K. Dong, Q. Liu, Y. Luo, T. Li, B. Tang, Y. Liu, S. Gao, A. M. Asiri, S. Yan, X. Sun, *Nano Res.* **2022**, *15*, 3880.
[447] J. Sahu, B. P. Mishra, K. Parida, *ACS Appl. Energy Mater.* **2025**, *8*, 388.
[448] Y. Zhang, X. Chen, Y. Ye, J. Chen, *J. Catal.* **2023**, *419*, 9.
[449] W. Tan, H. Zhao, L. Ding, N. Ren, X. Yu, A. Wang, M. Zhao, *ACS Appl. Nano Mater* **2025**, *8*, 2632.
[450] T. Hu, X. Cheng, J. Luo, Y. Yan, Q. Zhang, Y. Li, *ACS Catal.* **2024**, *14*, 14539.
[451] G. N. Schrauzer, T. D. Guth, *J. Am. Chem. Soc.* **1977**, *99*, 7189.
[452] K. Tennakone, S. Punchihewa, R. Tantrigoda, *Solar Energy Mater.* **1989**, *18*, 217.
[453] J. Wang, F. Tang, J. Gao, C. Yao, S. Zhang, L. Li, *Nanoscale* **2022**, *14*, 15091.
[454] S. Zhang, Y. Zhao, R. Shi, C. Zhou, G. I. N. Waterhouse, Z. Wang, Y. Weng, T. Zhang, *Angew. Chem., Int. Ed.* **2021**, *60*, 2554.
[455] Z. Gu, Y. Zhang, X. Wei, Z. Duan, Q. Gong, K. Luo, *Adv. Mater.* **2023**, *35*, 2303107.
[456] W. Zhang, Q. Tan, T. Liu, Z. Liang, Y. Huang, Y. He, D. Han, D. Qin, L. Niu, *ACS Mater. Lett.* **2024**, *6*, 3007.
[457] D. Cui, S. Wang, X. Yang, L. Xu, F. Li, *Small* **2024**, *20*, 2306229.
[458] X. Huang, Y. Shi, C. Liu, Z. Wang, J. Bi, J. C. Yu, L. Wu, *Appl. Surf. Sci.* **2023**, *640*, 158443.

© 2025 The Author(s). Advanced Functional Materials published by Wiley-VCH GmbH

16163028, 0, Downloaded from https://advanced.onlinelibrary.wiley.com/doi/10.1002/adfm.202502901 by EMBRAPA - Empresa Brasileira de Pesquisa Agropecuaria, Wiley Online Library on [06/06/2025]. See the Terms and Conditions (https://onlinelibrary.wiley.com/terms-and-conditions) on Wiley Online Library for rules of use; OA articles are governed by the applicable Creative Commons License

[459] H. Zhang, Y. Chen, Y. Pan, L. Bao, J. Ge, *J. Colloid Interface Sci.* **2023**, *642*, 470.
[460] K. Zhang, Z. Ai, M. Huang, D. Shi, Y. Shao, X. Hao, B. Zhang, Y. Wu, *J. Catal.* **2021**, *395*, 273.
[461] L. Zhang, Y. Meng, H. Shen, J. Li, C. Yang, B. Xie, S. Xia, *Inorg. Chem.* **2022**, *61*, 6045.
[462] J. Geng, S. Ji, *Nano Res.* **2024**, *17*, 4898.
[463] L. Chen, M. Liu, Y. Chen, S. Zhu, C. Sun, X. Tu, H. Zheng, *Catal. Sci. Technol.* **2023**, *13*, 2802.
[464] H. Lee, J.-H. Lee, Y. Lee, E.-B. Cho, Y. J. Jang, *Appl. Surf. Sci.* **2023**, *620*, 156812.
[465] J. Duan, Y. Qu, J. Chen, Q. Zhang, R. Liu, M. Bian, G. Chen, W. Wang, *J. Alloys Compd.* **2024**, *1003*, 175686.
[466] R. Bariki, S. K. Pradhan, S. Panda, S. K. Nayak, A. R. Pati, B. G. Mishra, *Langmuir* **2023**, *39*, 7707.
[467] R. Bariki, A. R. Pati, S. K. Pradhan, S. Panda, S. K. Nayak, B. G. Mishra, *Sustainable Energy Fuels* **2023**, *7*, 5633.
[468] N. Ojha, A. Bajpai, S. Kumar, *J. Colloid Interface Sci.* **2021**, *585*, 764.
[469] D. Prusty, S. Mansingh, K. M. Parida, *Catal. Sci. Technol.* **2023**, *13*, 1311.
[470] S. F. Almojil, A. I. Almohana, A. F. Alali, E.-A. Attia, K. Sharma, M. A. Shamseldin, A. G. Mohammed, Y. Cao, *New J. Chem.* **2022**, *46*, 21625.
[471] Y. Fang, Y. Cao, Q. Chen, *Chem. Eng. J.* **2023**, *462*, 142039.
[472] S. Zhang, Y. Zhao, R. Shi, C. Zhou, G. I. N. Waterhouse, L.-Z. Wu, C.-H. Tung, T. Zhang, *Adv. Energy Mater.* **2020**, *10*, 1901973.
[473] H. Wang, Q. Mao, T. Ren, T. Zhou, K. Deng, Z. Wang, X. Li, Y. Xu, L. Wang, *ACS Appl. Mater. Interfaces* **2021**, *13*, 44733.
[474] T. Hou, L. Chen, Y. Xin, W. Zhu, C. Zhang, W. Zhang, S. Liang, L. Wang, *ACS Energy Lett.* **2020**, *5*, 2444.
[475] J. V. Perales-Rondon, D. Rojas, W. Gao, M. Pumera, *ACS Sustainable Chem. Eng.* **2023**, *11*, 6923.
[476] H. Gao, J. Zhang, R. Wang, M. Wang, *Appl. Catal., B* **2015**, *172–173*, 1.
[477] W. Yu, J. Liu, M. Yi, J. Yang, W. Dong, C. Wang, H. Zhao, H. S. H. Mohamed, Z. Wang, L. Chen, Y. Li, B.-L. Su, *J. Colloid Interface Sci.* **2020**, *565*, 207.
[478] S.-J. Yang, Y.-K. Lin, Y.-C. Pu, Y.-J. Hsu, *J. Phys. Chem. Lett.* **2022**, *13*, 6298.
[479] Y. Zhang, B. Deng, T. Zhang, D. Gao, A.-W. Xu, *J. Phys. Chem. C* **2010**, *114*, 5073.
[480] A. George, D. Magimai Antoni Raj, X. Venci, A. Dhayal Raj, A. Albert Irudayaraj, R. L. Josephine, S. John Sundaram, A. M. Al-Mohaimeed, D. A. Al Farraj, T.-W. Chen, K. Kaviyarasu, *Environ. Res.* **2022**, *203*, 111880.
[481] Y.-H. Chang, H. Wang, T.-F. Siao, Y.-H. Lee, S.-Y. Bai, C.-W. Liao, J.-K. Zhuang, T.-W. Chiu, C.-H. Kuo, *J. Alloys Compd.* **2021**, *854*, 157235.
[482] N. Schmachtenberg, S. Silvestri, J. da Silveira Salla, G. L. Dotto, D. Hotza, S. L. Jahn, E. L. Foletto, *J. Environ. Chem. Eng.* **2019**, *7*, 102954.
[483] W. Xu, S. Zhu, Y. Liang, Z. Li, Z. Cui, X. Yang, A. Inoue, *Sci. Rep.* **2015**, *5*, 18125.
[484] M. Tanveer, C. Cao, I. Aslam, Z. Ali, F. Idrees, M. Tahir, W. S. Khan, F. K. Butt, A. Mahmood, *RSC Adv.* **2014**, *4*, 63447.
[485] D. Ayodhya, M. Venkatesham, A. Santoshi kumari, G. B. Reddy, D. Ramakrishna, G. Veerabhadram, *J. Exp. Nanosci.* **2016**, *11*, 418.
[486] R. K. Sithole, L. F. E. Machogo, M. J. Moloto, S. S. Gqoba, K. P. Mubiayi, J. Van Wyk, N. Moloto, *J. Photochem. Photobiol. A: Chem.* **2020**, *397*, 112577.
[487] Y. Liu, Y. Deng, Z. Sun, J. Wei, G. Zheng, A. M. Asiri, S. B. Khan, M. M. Rahman, D. Zhao, *Small* **2013**, *9*, 2702.
[488] S. Iqbal, A. Bahadur, S. Anwer, S. Ali, A. Saeed, R. Muhammad Irfan, H. Li, M. Javed, M. Raheel, M. Shoaib, *Appl. Surf. Sci.* **2020**, *526*, 146691.
[489] N. Tavker, U. K. Gaur, M. Sharma, *ACS Omega* **2019**, *4*, 11777.
[490] D. Lakhdari, N. Lakhdari, I. Laourari, A. Berchi, Y. Park, Y. Vasseghian, M. Berkani, *J. Ind. Eng. Chem.* **2023**, *124*, 422.
[491] C.-X. Liu, W.-H. Zhang, N. Wang, P. Guo, M. Muhler, Y. Wang, S. Lin, Z. Chen, G. Yang, *Chem. Eur. J.* **2018**, *24*, 16804.
[492] W. Zou, L. Zhang, L. Liu, X. Wang, J. Sun, S. Wu, Y. Deng, C. Tang, F. Gao, L. Dong, *Appl. Catal., B* **2016**, *181*, 495.
[493] Y.-C. Pu, H.-Y. Chou, W.-S. Kuo, K.-H. Wei, Y.-J. Hsu, *Appl. Catal., B* **2017**, *204*, 21.
[494] X. Yu, J. Zhang, Y. Chen, Q. Ji, Y. Wei, J. Niu, Z. Yu, B. Yao, *J. Environ. Chem. Eng.* **2021**, *9*, 106161.
[495] Y. Cheng, Y. Lin, J. Xu, J. He, T. Wang, G. Yu, D. Shao, W.-H. Wang, F. Lu, L. Li, X. Du, W. Wang, H. Liu, R. Zheng, *Appl. Surf. Sci.* **2016**, *366*, 120.
[496] B. Zhan, Y. Liu, S. Li, C. Kaya, T. Stegmaier, M. Aliabadi, Z. Han, L. Ren, *Appl. Surf. Sci.* **2019**, *496*, 143580.
[497] W. Zhang, B. Wang, C. Hao, Y. Liang, H. Shi, L. Ao, W. Wang, *J. Alloys Compd.* **2016**, *684*, 445.
[498] G. Yang, H. Li, D. Yekeh, B. Deng, Z. Chen, S. Duan, L. Yang, *Sep. Purif. Technol.* **2025**, *353*, 128559.
[499] Y. Xu, D. Liang, M. Liu, D. Liu, *Mater. Res. Bull.* **2008**, *43*, 3474.
[500] R. C. Ding, Y. Z. Fan, G. S. Wang, *ChemistrySelect* **2018**, *3*, 1682.
[501] N. Dasineh Khiavi, R. Katal, S. Kholghi Eshkalak, S. Masudy-Panah, S. Ramakrishna, H. Jiangyong, *Nanomaterials* **2019**, *9*, 1011.
[502] F. Bayat, S. Sheibani, *Mater. Res. Bull.* **2022**, *145*, 111561.
[503] W. Cui, W. An, L. Liu, J. Hu, Y. Liang, *J. Hazard. Mater.* **2014**, *280*, 417.
[504] S. Hu, F. Zhou, L. Wang, J. Zhang, *Catal. Commun.* **2011**, *12*, 794.
[505] G. R. Surikanti, P. Bajaj, M. V. Sunkara, *ACS Omega* **2019**, *4*, 17301.
[506] S. Min, F. Wang, Z. Jin, J. Xu, *Superlattices Microstruct.* **2014**, *74*, 294.
[507] A. Norouzi, A. Nezamzadeh-Ejhieh, *Phys. B* **2020**, *599*, 412422.
[508] J. Liu, J. Ke, D. Li, H. Sun, P. Liang, X. Duan, W. Tian, M. O. Tadé, S. Liu, S. Wang, *ACS Appl. Mater. Interfaces* **2017**, *9*, 11678.
[509] R. Rajendran, S. Vignesh, A. Sasireka, P. Priya, S. Suganthi, V. Raj, J. K. Sundar, M. Srinivasan, M. Shkir, S. AlFaify, *Colloid Interface Sci. Commun.* **2021**, *44*, 100480.
[510] S. Zuo, Y. Chen, W. Liu, C. Yao, X. Li, Z. Li, C. Ni, X. Liu, *Ceram. Int.* **2017**, *43*, 3324.
[511] M. Kuczynski, M. Luba, T. Mikolajczyk, B. Pieroiynski, A. Jasiecka-Mikolajczyk, L. Smoczynski, P. Solowiej, P. Wojtacha, *Molecules* **2021**, 26.
[512] I. Santana, M. Silva, N. Neves, F. Silva, M. Henrique, J. Cavalcanti, R. Garcia, J. Rodríguez-Diaz, M. Duarte, D. Napoleao, *Appl. Catal. O: Open* **2024**, *188*.
[513] A. Bahdaouia, S. Amara, L. Adnane, A. Mahieddine, *J. Appl. Electrochem.* **2024**, *54*, 1741.
[514] X. Li, S. Raza, C. Liu, *J. Environ. Chem. Eng.* **2021**, *9*, 106133.
[515] H. Tang, X. Liu, M. Xiao, Z. Huang, X. Tan, *J. Environ. Chem. Eng.* **2017**, *5*, 4447.
[516] S. Karthikeyan, S. Kumar, L. J. Durndell, M. A. Isaacs, C. M. A. Parlett, B. Coulson, R. E. Douthwaite, Z. Jiang, K. Wilson, A. F. Lee, *ChemCatChem* **2018**, *10*, 3554.
[517] Y. Tang, Y. Xu, C. Qi, X. Li, E. Xing, F. Wang, Z. Kan, C. Wang, J. Tang, G. Zheng, K. Zhang, X. Wang, C. Li, K. Yang, *J. Nanosci. Nanotechnol.* **2018**, *18*, 8282.
[518] R. Singaravelan, A. Salam, N. Krishnan, P. Vasanthi, *Inorg. Chem. Commun.* **2022**, 142.
[519] Z. Huang, L. Wang, H. Wu, H. Hu, H. Lin, L. Qin, Q. Li, *J. Alloys Compd.* **2022**, *896*, 163045.
[520] D. Jiang, J. Xue, L. Wu, W. Zhou, Y. Zhang, X. Li, *Appl. Catal., B* **2017**, *211*, 199.
[521] M. Li, Z. Wang, Q. Zhang, C. Qin, A. Inoue, W. Guo, *Appl. Surf. Sci.* **2020**, *506*, 144819.

© 2025 The Author(s). Advanced Functional Materials published by Wiley-VCH GmbH

16163028, 0, Downloaded from https://advanced.onlinelibrary.wiley.com/doi/10.1002/adfm.202502901 by EMBRAPA - Empresa Brasileira de Pesquisa Agropecuaria, Wiley Online Library on [06/06/2025]. See the Terms and Conditions (https://onlinelibrary.wiley.com/terms-and-conditions) on Wiley Online Library for rules of use; OA articles are governed by the applicable Creative Commons License

[522] L. Yang, J. Guo, T. Yang, C. Guo, S. Zhang, S. Luo, W. Dai, B. Li, X. Luo, Y. Li, *J. Hazard. Mater.* **2021**, *402*, 123741.
[523] C. Yang, J. Wang, L. Mei, X. Wang, *J. Mater. Sci. Technol.* **2014**, *30*, 1124.
[524] Y. Zhang, Z. Zhang, Y. Zhang, Y. Li, Y. Yuan, *J. Colloid Interface Sci.* **2023**, *651*, 117.
[525] Z. Zheng, B. Huang, Z. Wang, M. Guo, X. Qin, X. Zhang, P. Wang, Y. Dai, *J. Phys. Chem. C* **2009**, *113*, 14448.
[526] Y. Su, H. Li, H. Ma, J. Robertson, A. Nathan, *ACS Appl. Mater. Interfaces* **2017**, *9*, 8100.
[527] W.-C. Huang, L.-M. Lyu, Y.-C. Yang, M. H. Huang, *J. Am. Chem. Soc.* **2012**, *134*, 1261.
[528] Y. Shang, D. Sun, Y. Shao, D. Zhang, L. Guo, S. Yang, *Chemistry* **2012**, *18*, 14261.
[529] J. Li, M. He, J. Yan, J. Liu, J. Zhang, J. Ma, *Nanomaterials* **2022**, *12*.
[530] W. C. J. Ho, Q. Tay, H. Qi, Z. Huang, J. Li, Z. Chen, *Molecules* **2017**, *22*, 677.
[531] L. Deng, M. Li, X. Gao, X. Yi, Y. Zhao, Y. Yang, Z. Zhao, J. Chen, B. Dou, F. Bin, *J. Hazard. Mater.* **2025**, *484*, 136796.
[532] C. Dai, X. Tian, Y. Nie, H.-M. Lin, C. Yang, B. Han, Y. Wang, *Environ. Sci. Technol.* **2018**, *52*, 6518.
[533] T. Li, Z.-Z. Ding, F. Shi, Y.-T. Ju, T.-T. Du, C. Liu, X. Zhang, *J. Environ. Chem. Eng.* **2024**, *12*, 112039.
[534] Q. Zhao, K. Wang, J. Wang, Y. Guo, A. Yoshida, A. Abudula, G. Guan, *ACS Appl. Nano Mater.* **2019**, *2*, 2706.
[535] P. Wang, C. Qi, L. Hao, P. Wen, X. Xu, *J. Mater. Sci. Technol.* **2019**, *35*, 285.
[536] L. Zhang, Y. Zhao, L. Zhong, Y. Wang, S. Chai, T. Yang, X. Han, *Appl. Surf. Sci.* **2017**, *422*, 1093.
[537] M. Wan, Y. Zhang, W. Wei, S. Cui, H. Hou, W. Chen, L. Mi, *ChemistrySelect* **2019**, *4*, 7512.
[538] Y. zhang, X. Li, J. Chen, Y. Wang, Z. Cheng, X. Chen, X. Gao, M. Guo, *Appl. Surf. Sci.* **2023**, *611*, 155744.
[539] N. S. Bisht, S. P. S. Mehta, N. G. Sahoo, A. Dandapat, *Dalton Trans.* **2021**, *50*, 5001.
[540] Z. Tong, Y. Liu, X. Wu, Y. Cheng, J. Yu, X. Zhang, N. Liu, X. Liu, H. Li, *Nanomaterials* **2024**, *14*.
[541] K. S. Prasad, H.-B. Noh, S. S. Reddy, A. E. Reddy, Y.-B. Shim, *Appl. Catal., A* **2014**, *476*, 72.
[542] Y. Pei, X. Zheng, C. Lu, S. Hu, Z. Wang, Z. Shi, W. Zhong, Z. Xiao, X. Liu, *Appl. Surf. Sci.* **2025**, *679*, 161144.
[543] H. Sudrajat, D. Lisovytskiy, J. C. Colmenares, *Catal. Sci. Technol.* **2024**, *14*, 6893.
[544] B. Li, J. Hong, Y. Ai, Y. Hu, Z. Shen, S. Li, Y. Zou, S. Zhang, X. Wang, G. Zhao, X. Xu, *J. Catal.* **2021**, *399*, 142.
[545] W. Zhang, R. Liu, X. Lv, L. Jiang, S. Tang, G. Liu, G. Shen, X. Huang, C. Ma, B. Yang, *Molecules* **2023**, *28*, 6460.
[546] Y. Chen, M. Wang, Y. Ma, Y. Li, J. Cai, Z. Li, *Catal. Sci. Technol.* **2018**, *8*, 2218.
[547] X. Li, D. Wei, L. Ye, Z. Li, *Inorg. Chem. Commun.* **2019**, *104*, 171.
[548] T. Bezghiche-Imloul, H. Hammache-Makhloufi, N. Ait Ahmed, *Surf. Rev. Lett.* **2016**, *23*, 1650041.
[549] A. Yarmolenko, B. Malik, E. S. Avraham, G. D. Nessim, *Nanomaterials* **2023**, *13*, 1234.
[550] B. D. Queiroz, P.-L. S. Vital, K. O. Budke, N. Rey-Raap, A. Arenillas, G. M. O. Barra, D. S. Ferreira, G. A. Camara, H. Wender, C. A. Martins, *ACS Appl. Mater. Interfaces* **2024**, *16*, 35255.
[551] L. Chen, Z. Hua, J. Shi, M. He, *ACS Appl. Mater. Interfaces* **2018**, *10*, 39002.
[552] I. Petriev, P. Pushankina, Y. Glazkova, G. Andreev, M. Baryshev, *Coatings* **2023**, *13*.
[553] A. Badalyan, S. S. Stahl, *Nature* **2016**, *535*, 406.
[554] M. Hasanzadeh, G. Karim-Nezhad, M. G. Mahjani, M. Jafarian, N. Shadjou, B. Khalilzadeh, L. A. Saghatforoush, *Catal. Commun.* **2008**, *10*, 295.
[555] J. Zhang, H. Ding, H. Hui, Q. Yao, W. Feng, T. Chen, T. W. B. Lo, Y. Ren, L. Ye, B. Yue, H. He, *Small* **2024**, *20*, 2405150.
[556] X. Zhang, X. R. Zhang, P. Yang, H.-S. Chen, S. P. Jiang, *Chem. Eng. J.* **2022**, *450*, 138030.
[557] L. Sun, D. Wang, Y. Li, B. Wu, Q. Li, C. Wang, S. Wang, B. Jiang, *Chin. Chem. Lett.* **2023**, *34*, 107490.
[558] J. He, M. Zhang, A. Primo, H. García, Z. Li, *J. Mater. Chem. A* **2018**, *6*, 19782.
[559] M. T. Gonfa, S. Shen, L. Chen, S.-F. Yin, *Colloids Surf. A* **2025**, *706*, 135746.
[560] Y.-D. Shan, S.-H. Wu, Y.-L. Wang, C. Wang, S.-Q. Zhi, Y. Liu, X. Han, *Inorg. Chem.* **2023**, *62*, 4872.
[561] Y. Feng, C. Jia, H. Zhao, K. Wang, X. Wang, *New J. Chem.* **2022**, *46*, 4082.
[562] S. Qiao, B. Fan, Y. Yang, N. Liu, H. Huang, Y. Liu, *RSC Adv.* **2015**, *5*, 43058.
[563] A. Shahzeydi, M. Ghiaci, H. Farrokhpour, A. Shahvar, M. Sun, M. Saraji, *Chem. Eng. J.* **2019**, *370*, 1310.
[564] D. Peng, Y. Zhang, G. Xu, Y. Tian, D. Ma, Y. Zhang, P. Qiu, *ACS Sustainable Chem. Eng.* **2020**, *8*, 6622.
[565] T. Siboonruang, R. Alaufey, N. H. Attanayake, M. Tang, *J. Electrochem. Soc.* **2024**, *171*, 083502.
[566] Y. Ru, Y. Chen, X. Yu, Q. Zhang, Y. Yin, G. Tian, *Chem. Eng. J.* **2023**, *475*, 146158.
[567] L.-H. Gao, W.-Y. Xiao, M.-Y. Qi, J.-Y. Li, C.-L. Tan, Z.-R. Tang, *Mol. Catal.* **2024**, *554*, 113858.
[568] T. Hu, Z. Yue, Y. Wang, Y. Yu, Y. Chang, L. Pei, W. Chen, P. Han, W. Martens, E. R. Waclawik, H. Wu, H. Y. Zhu, J. Jia, *J. Colloid Interface Sci.* **2024**, *663*, 632.
[569] H.-L. Qi, D.-S. Chen, J.-S. Ye, J.-M. Huang, *J. Org. Chem.* **2013**, *78*, 7482.

© 2025 The Author(s). Advanced Functional Materials published by Wiley-VCH GmbH

16163028, 0, Downloaded from https://advanced.onlinelibrary.wiley.com/doi/10.1002/adfm.202502901 by EMBRAPA - Empresa Brasileira de Pesquisa Agropecuaria, Wiley Online Library on [06/06/2025]. See the Terms and Conditions (https://onlinelibrary.wiley.com/terms-and-conditions) on Wiley Online Library for rules of use; OA articles are governed by the applicable Creative Commons License

Yanjie Wang received her Ph.D. in physical chemistry from the National Center for Nanoscience and Technology (NCNST), China, in 2018, and subsequently joined NCNST as a research staff. From 2022 to 2024, she was a Postdoctoral Researcher at the University of Oxford. Her current research focuses on the rational design of nanomaterials for sustainable energy applications.

Tao He received his Ph.D. from the Institute of Chemistry, Chinese Academy of Sciences in 2002. He became a professor at National Center for Nanoscience and Technology, China in 2009 after postdoctoral training respectively in Weizmann Institute of Science, Israel and Rice University, USA. His research interest mainly focuses on green nanocatalysis for energy and environment. He has published more than 160 papers in peer-reviewed journals, including *Journal of the American Chemical Society*, *Advanced Materials*, *Advanced Functional Materials*, *Progress in Materials Science*, *Small*, and the like. He was selected by Hundred-Talent Program (Chinese Academy of Sciences) in 2009.

Alexei V. Emeline graduated from the Department of Physical Chemistry at Tomsk State University. He received his PhD in molecular physics and Doctor of Science in condensed matter physics at Saint-Petersburg University. Currently, he is professor of the Department of Photonics and deputy head in the laboratories "Photoactive nanocomposite materials" and "Photonics of Crystals" at Saint-Petersburg University. His major research interests are focused on photophysics and photochemistry of solids, heterogeneous photocatalysis, photoelectrochemical solar energy conversion, optical and luminescence behavior of halide perovskites, and metal–organic frameworks.

Osmando F Lopes received his Ph.D. degree in physical chemistry from the Federal University of São Carlos (Brazil) in 2016. He was a postdoctoral fellow at São Paulo University, Brazil (2016-2018). He was also a visiting researcher of the Forschungszentrum Jülich, Germany (2020-2021), sponsored by Alexander von Humboldt Foundation. Since 2018, he is an Adjunct Professor at the Federal University of Uberlândia, Brazil, where his research focuses on the development of novel electrocatalysts and photocatalysts for energy conversion, CO_2 reduction, and H_2 production.

© 2025 The Author(s). Advanced Functional Materials published by Wiley-VCH GmbH

16163028, 0, Downloaded from https://advanced.onlinelibrary.wiley.com/doi/10.1002/adfm.202502901 by EMBRAPA - Empresa Brasileira de Pesquisa Agropecuaria, Wiley Online Library on [06/06/2025]. See the Terms and Conditions (https://onlinelibrary.wiley.com/terms-and-conditions) on Wiley Online Library for rules of use; OA articles are governed by the applicable Creative Commons License

Antonio Otávio T. Patrocinio received his Ph.D. from Universidade de São Paulo, Brazil. He works as a Full Professor, head of the Laboratory of Photochemistry and Materials Science, and Coordinator of the Advanced Research Center in Energy Transition at the Federal University of Uberlandia, Brazil. He was honored by the German Federal Ministry of Education and Research (BMBF) with the Green Talents Award for his contributions in renewable energy research. He is a Alexander von Humboldt fellow, member of the Royal Society of Chemistry, and has published over 90 scientific papers (h-index: 32). His research focuses on inorganic materials for artificial photosynthesis.

Jia Hong Pan is a Professor at the School of Resources, Environment and Materials, Guangxi University, and academic leader of the State Key Laboratory of Featured Metal Materials and Life-Cycle Safety for Composite Structures. Together with Detlef W. Bahnemann, he co-founded the International Joint Center for Nature-Inspired Carbon Neutrality Solutions. He serves on the Editorial Boards of Catalysis Letters and Chemistry of Inorganic Materials. He has published over 130 scientific papers with citations over 7,000 times (h-index: 44). His research focuses on self-assembled inorganic materials, semiconductor photo(electro)catalysis, and electrochemical energy storage.

Caue Ribeiro is a Senior Researcher at Embrapa Instrumentation (Brazil), where he coordinates the National Laboratory for Nanotechnology Applied to Agribusiness, and is an Affiliated Professor in the Graduate Programs in Chemistry at the University of São Paulo and the Federal University of São Carlos. He is a former Visiting Researcher at the National Center for Nanoscience and Technology in Beijing (China) and at Forschungszentrum Jülich (Germany). From 2012 to 2024, he coordinated the Embrapa AgroNano Network and led its Nanotechnology Projects Portfolio from 2020 to 2024. His research focuses on nanomaterials for controlled release systems and photo/electrocatalytic applications, and has been cited over 13,000 times (h-index: 65).

Detlef W. Bahnemann is the Director of the Megagrant Laboratory "Photoactive Nanocomposite Materials" at St. Petersburg State University (Russia) and a Distinguished Professor at Shaanxi University of Science & Technology, Xi'an (Peoples Republic of China). He is a Highly Cited Author with his current h-Index being 118, whose papers have been cited more than 85,000 times altogether. Currently, he is a Visiting Scholar at Queens University Belfast (United Kingdom), Fellow of the European Academy of Sciences (EURASC), and Member of the Academia Europaea (AE).

© 2025 The Author(s). Advanced Functional Materials published by Wiley-VCH GmbH

16163028, 0, Downloaded from https://advanced.onlinelibrary.wiley.com/doi/10.1002/adfm.202502901 by EMBRAPA - Empresa Brasileira de Pesquisa Agropecuaria, Wiley Online Library on [06/06/2025]. See the Terms and Conditions (https://onlinelibrary.wiley.com/terms-and-conditions) on Wiley Online Library for rules of use; OA articles are governed by the applicable Creative Commons License